Growth and Characterization of ZnO and Related Nanostructures

A thesis for the degree of
DOCTOR OF PHILSOPHY

Presented to

DUBLIN CITY UNIVERSITY

By
JUSTINA GRABOWSKA, M.Sc.

Research Supervisor
DR. ENDA MCGLYNN
School of Physical Sciences
Dublin City University

13 June 2007

Declaration

I herby certify that this material, which I now submit for assessment on the programme of study leading to the award of Doctor of Philosophy is entirely my own work and has not been taken from the work of others save and to the extent that such work has been cited and acknowledged within the text of my work.

Signed: Justina Grabowska
Justina Grabowska

ID No.: 53144341

Date: 02/07/07

Acknowledgements

There are a lot of people I would like to thank for a huge variety of reasons.

Firstly, I would like to thank my supervisor, Dr. Enda McGlynn. I could not have imagined having a better advisor and mentor for my PhD. Thank you for supervising my thesis work and for supporting and encouraging me along the way, and for enthusiasm and inspiration which was always there when I needed it. Thank you for your patience in reading and correcting my thesis. Throughout my thesis-writing period, you provided encouragement, sound advice, good teaching, good company, and lots of good ideas…but the biggest thank you is for you to being my good friend, I really appreciate that very much.

Thank you to everyone in my group: James, Deirdre, Ger, Alan, Conor, Brendan for your help, advice and friendship. Ricky, thank you for being my best friend and for all the great fun and unforgettable memories I have with you from my PhD period. I really appreciate you correcting my written English, teaching me new words and giving me English lessons. Also, an especially big thank you to Dr. Karuna Kar Nanda and Dr. R.T. Rajendra Kumar for all your help with my first steps in the research world. Thank you for teaching me the skills I have needed to develop. I have really enjoyed working with you.

Many thanks to everyone in the physics department: Sheila, Lisa, Ray, Alan, Pat and Des for your help in various situations over last few years.

Many thanks to my parents and my family for their support and encouragement over the last few years. Finally and the most importantly thank you Sven not only for support and for taking such good care of me but for your love and a very big heart.

Thanks to SFI, the NCPST and the School of Physical Sciences for financing and facilitating this work.

Publications

The present work has so far resulted in the following publications:

1. **J. Grabowska**, R. T. Rajendra Kumar, E. McGlynn, K. K. Nanda, S. B. Newcomb, P. J. McNelly, L. O'Railly, J. -P. Mosnier, Martin O. Henry, , 'Growth and Characterization of Epitaxially Ordered Zinc Aluminate Domains on *c*-Sapphire', *Thin Solid Films* (article in press)
2. R. T. Rajendra Kumar, **J. Grabowska**, J. -P. Mosnier, M. O. Henry, E. McGlynn, 'Morphological control of ZnO nanostructures grown on silicon', Zinc Oxide Materials and Devices II, edited by Ferechteh Hosseini Teherani, Cole W. Litton, Proceedings of SPIE Vol. 6474 (SPIE, Bellingham, WA, 2007), article # 64741I.
3. **J.Grabowska**, K. K. Nanda, R. T. Rajendra-Kumar, J. -P. Mosnier, M. O. Henry, S. B. Newcomb, P. J. McNally, L. O'Reilly, Xu Lu, E. McGlynn, 'Self organized, horizontal, cubic phase ZnO nanowires', *Superlattices and Microstructures* (article in press)
4. R. T. Rajendra Kumar, **J. Grabowska**, J. -P. Mosnier, M. O. Henry, E. McGlynn, 'Morphological control of ZnO nanostructures grown on silicon', *Superlattices and Microstructures* (article in press)
5. **J. Grabowska**, A. Meaney, K. K. Nanda, E. McGlynn, J. -P. Mosnier, M. O. Henry, 'Laterally and vertically grown ZnO nanostructures on c-sapphire', *Proseedings of SPIE,* **5824** (2005) 269
6. R. Groarke, **J. Grabowska**, E. McGlynn, J. G. Vos, 'Spectroscopic study of the properties of chemically modified ZnO nanowires', *Proseedings of SPIE,* **5826** (2005) 194
7. **J. Grabowska**, A. Meaney, K. K. Nanda, J. -P. Mosnier, M. O. Henry, J. -R. Duclere, and E. McGlynn, 'Surface excitonic and quenching effects in ZnO nanowire/nanowall systems: Limiting effects on device potential', *Physical Review B* **71** (2005) 115439

8. **J. Grabowska,** G. Tobin, K. K. Nanda, E. McGlynn, J. -P. Mosnier, and M. O. Henry, ' Synthesis and Photoluminescence of ZnO nanowires/nanorods', *Journal of Materials Science: Materials in Electronics* **16** (2005) 397
9. **J. Grabowska**, K. K. Nanda, E. McGlynn, J. -P. Mosnier, and M. O. Henry, 'Studing the growth conditions, the alignment and structure of the ZnO nanorods.', *Surface and Coating technology* **200** (2005) 1093
10. R. Korbutowicz, E. Dumiszewska, **J. Grabowska**, 'Podloza alternatywne stosowane w epitaksji azotku galu', *Elektronika,* 11 (2003) 5

Conferences

The present work has so far presented in the following conferences:

1. **Plasma Proceses for Biomedical Applications,** 24 May 2007 Dublin (DCU), Ireland – (***Poster Presentation – J. Grabowska,*** 'Bio-Applications of ZnO Nanorods – Living cell immobilization on ZnO nanorods'*)*
2. **SPIE Photonics WEST,** 20-25 January 2007 San Jose, California, USA (*Oral presentation – Dr. E. McGlynn,* 'Morphological control of ZnO nanostructures grown on silicon')
3. **CVD Ireland**, 20 October 2006 (DCU), Ireland (***Oral Presentation – J. Grabowska,*** 'ZnO nanorods/nanowalls: Steps towards morphological control'*)*
4. **IPBPG**, 12 May 2006 Dublin (DCU), Ireland (***Oral Presentation – J. Grabowska,*** 'ZnO and related nanostructures for nanophotonic and electronic devices: Growth and analysis')
5. **ZnO WORKSHOP**, 5 May 2006 Dublin (DCU), Ireland – (***Oral Presentation – J. Grabowska,*** 'Growth of ZnO nanostructures using vapour phase growth and materials characterization'*)*

6. **EMRS_ Spring Meeting 2006**, 29 May – 2 June 2006 Nice, France – (2 *Oral presentations – Dr. E. McGlynn,* 'Self-organized ZnAl2O4 nanostructures grown on c-sapphire' & 'Morphological control of ZnO nanostructures on silicon substrates'*)*
7. **SPIE 2005**, Opto Ireland, 4-6 April 2005 Dublin, Ireland – (***Poster presentation – J. Grabowska,*** 'Laterally and vertically grown ZnO nanostructures on c-sapphire'*) & (Oral presentation – R. Groarke,* 'Spectroscopic Properties of Chemically Modified Zinc Oxide Nanorods'*)*
8. **MFMN 2004**, 5th Internatiomal Conference Materials for Microelectronics and Nanoengineering, 13-14 September 2004 Southampton, UK – (*Oral presentation – Dr. E. McGlynn,* 'Synthesis and Photoluminescence of ZnO nanowires/nanorods'*)*
9. **PSE 2004**, Ninth International Conference on Plasma Surface Engineering, September 13-17, 2004 Garmish-Partenkirchen, Germany – (***Poster presentation - J. Grabowska,*** 'Studying the growth conditions, the alignment and structure of the ZnO nanorods'*)*
10. **SOXESS**, European Network on ZnO First Workshop, 5-7 September 2003 Autrans, France

Seminars & Competitions

1. NCPST 2006, Postgraduate Seminar, 20 September 2006 ('ZnO and related nanostructures for nanophotonic and electronic devices: Growth and analysis'), Dublin City University, Dublin, Ireland
2. BOC 2006, Poster Competition, 14 September 2006 Dublin City University, Dublin, Ireland
3. NCPST competition for the best paper 2005, **J. Grabowska,** G. Tobin, K. K. Nanda, E. McGlynn, J. -P. Mosnier, and M. O. Henry, ' Synthesis and Photoluminescence of ZnO nanowires/nanorods', *Journal of Materials Science: Materials in Electronics* **16** (2005) 397, Dublin City University, Dublin, Ireland, – (***1st prize***)

4. BOC 2005, Poster Competitions, 26 May 2005 Dublin City University, Dublin, Ireland,– (***3rd prize)***
5. BOC 2004, Poster Competitions, 14 April 2004 Dublin City University, Dublin, Ireland
6. WEMiF, Poster Competitions, 2003 Wroclaw University of Technology (Faculty of Microsystem Electronics and Photonics), Wroclaw, Poland, – (***1st prize***)

Abstract

Growth and characterization of ZnO and related nanostructures.

Zinc oxide (ZnO) nanostructures exhibit unique optical properties which makes them potential candidates for optoelectronic device applications. It is very important for various applications to be able to control morphology of low dimensionality nanostructures. In the first part of this thesis, synthesis and characterization of well aligned ZnO nanorods and nanorods/nanowalls nanostructures and the understanding of growth morphology are described.

By using a simple vapour phase transport (VPT) and condensation process, we have grown low dimensionality ZnO nanostructures on *a*-plane sapphire with gold (Au) catalyst. The catalytic growth of various nanostructures is controlled by the conventional vapour liquid solid (VLS) mechanism. We demonstrate that morphology of ZnO nanostructure could be controlled by varying the parameters viz., substrates, growth duration, growth temperature, and Au catalyst thickness.

Temperature dependent photoluminescence analysis indicates the ZnO nanostructures are of excellent optical quality. In the case of samples showing both nanorod and nanowall morphologies, we observe an intense excitonic emission at 3.37 eV at low temperature and the intensity decays rapidly with increasing the temperature. We propose this peculiar behaviour is due to high surface to volume ratio associated with the nanorod/nanowall systems. The use of such nanostructures in room temperature optoelectronic devices appears to be dependent on the control or elimination of such surface effects.

Arising from our studies of ZnO growth on sapphire we have also grown epitaxially ordered zinc aluminate ($ZnAl_2O_4$) with sub-micron dimensions on bare *c*-sapphire substrates. The epitaxially oriented deposit displays the form of characteristically twinned grains. The structure of these grains and their epitaxial relation to the substrate is studied using TEM, in cross-section and plan-view, in addition to FESEM and other measurements.

The growth of these grains is strongly associated with the presence of extended defects in the sapphire substrate, and can be seeded by local mechanical damage to the substrate.

List of Acronyms

0D	*Zero Dimensional*
1D	*One Dimensional*
2D	*Two Dimensional*
AFM	*Atomic Force Microscopy*
BE	*Bound Exciton*
CD	*Compact Disc*
CL	*Cathodoluminescence*
Cps	*Cycle Per Second*
EP	*Eagle-Picher Corporation*
FE	*Free Exciton*
FESEM	*Field Emission Scanning Electron Microscopy*
FET	*Field Effect Transistor*
FIB	*Focused Ion Beam*
HRXRD	*High Resolution X-Ray Diffraction*
FWHM	*Full Width at Half Maximum*
THE	*High Temperature Electronic*
HVPE	*Hydride Vapour Phase Epitaxy*
JCPDS	*Joint Committee on Powder Diffraction Standards*
L	*Liquid*
LD	*Laser Diode*
LED	*Light Emitting Diode*
LTF	*Lenton Tube Furnace*
MFC	*Mass Flow Controller*
MOCVD	*Metalorganic Chemical Vapour Deposition*
MP	*Melting Point*

NSL	*Nanosphere Litography*
PL	*Photoluminescence Spectroscopy*
PLD	*Pulsed Laser Deposition*
PVD	*Physical Vapour Deposition*
RC	*Rocking Curve*
S	*Solid*
SAED	*Selected Area Electron Diffraction*
SEM	*Scanning Electron Microscopy*
SX	*Surface Exciton*
TCO	*Transparent Conducting Oxide*
TE	*Thermal Evaporation*
TEM	*Transmission Electron Microscopy*
TCO	*Transport Conducting Oxide*
UV	*Ultra Violet*
V	*Vapour*
VS	*Vapour Solid*
VLS	*Vapour Liquid Solid*
VPT	*Vapour Phase Transport*
XRD	*X-Ray Diffraction*

Table of Contents

1 Introduction, Material Properties, Potential Applications and Novel Devices

In this introduction chapter of the thesis, material properties of ZnO and $ZnAl_2O_4$ and potential applications of various types of nanostructures are presented. The purpose of this chapter is to answer broad questions, for example 'Why is this work about ZnO and $ZnAl_2O_4$, and why does it concentrate on nanostructures and not thin films?' It is very interesting to note that many materials used to form nanostructures either change their intrinsic properties at nanoscale sizes or change various extrinsic properties such as sensitivity to ambient environment depending on the size and shape and may thus show new behaviour due to the nanostructure morphology. It has been observed previously that the reduction of particle size affects important properties such as the electronic structure, conductivity, melting temperature and mechanical properties. So, one of the challenges in nanocrystal synthesis is to control not only the crystal size but also the shape and morphology as well. ZnO and $ZnAl_2O_4$ are two very interesting materials for nanostructure applications both in terms of their wide applicability for various technologies and for understanding fundamental physical concepts. These aspects will be outlined in the following sections. Particularly, the optical properties of nanostructured materials are very interesting due to potential applications in the fabrication of optoelectronic devices. In chapter four and in chapter five of my thesis the optical properties for well aligned ZnO nanorods and nanorods/nanowalls are presented.

1.1 Importance and Material Properties of ZnO and $ZnAl_2O_4$

Wide bandgap II-VI semiconductors offer new and exciting possibilities for applications in optoelectronics. The future development of technology naturally inspires research regarding functional devices based on new materials. For example, materials research for the next generation of compact disk (CD) read-heads remains highly competitive. The shorter the wavelength of the operating laser, the more information the devices can store due to the

reduced diffraction limit at shorter wavelengths. New semiconductor materials and structures are key aspects in advancing photonics and other technologies.

Oxides generally are the basis of many 'smart' and functional materials. Synthesis and device fabrication using functional oxides have attracted a lot of attention recently because the physical properties of these materials can be tuned. By varying the ratio of cations to anions or through doping with impurity atoms the electrical, optical, magnetic, and chemical properties can be tuned. The unique characteristic of functional oxides makes these materials a very diverse class of materials, with applications in areas such as semiconductor-photonics [1], superconductivity [2], ferroelectricity [3], and magnetism [4], sensors [5] etc. In the following pages we outline the most important materials properties of both ZnO and $ZnAl_2O_4$ materials, of relevance to this thesis and then outline some of the most important aspects of current ZnO nanostructure research.

Zinc Oxide (ZnO)

Zinc oxide is II-VI compound semiconductor. ZnO can crystallise in a variety of crystal structures including wurtzite, zincblende and rocksalt, but the stable structure at ambient temperatures and pressures is the hexagonal, wurtzite structure shown in Figure 1.1 below [6].

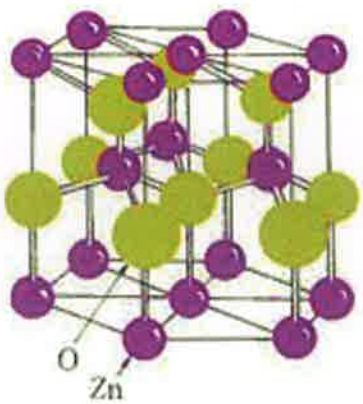

Figure 1.1 Stick and ball representation of the wurtzite ZnO crystal structures with Zn and O atoms labelled (taken from [7]).

Wurtzite zinc oxide has a hexagonal structure (space group *C6mc*) with two lattice parameters a = 0.3296 and c = 0.52065 nm.

From the point of view of potential technological applications zinc oxide has a number of notable properties:

1. It has a wide direct bandgap (~ 3.37 eV at 300 K) and thus is receiving renewed attention for device applications due to a number of advantages it presents in comparison with GaN (bandgap ~ 3.4 eV at 300 K), for example larger exciton binding energy, availability of large area substrates for homo-epitaxy, etc [8]. The high exciton binding energy of 60 meV (which is larger than the thermal energy at room temperature) leads to excitonic emission at room temperature and above [9]. In this regard ZnO is a promising photonic material for UV/blue devices such as short wavelength light emitting diodes and laser diodes in optoelectronics.
2. ZnO is a semiconducting, piezoelectric material. It shows a high degree of surface "activity" in terms of interacting via ad- and chemi-sorption with the surrounding ambient. This leads to potential applications in e.g. field emission displays, gas sensors, nanoresonators, and nanocantilevers etc. These devices may have important applications in nanosystems and biotechnology [10 - 13].
3. ZnO naturally forms a wide variety of nanostructures using a range of growth techniques, including nanorods, nanowires, nanobelts, nanorod/nanowall, nanotubes etc. These structures in many cases display a degree of crystal perfection which far exceeds that of thin films, even on lattice mismatched surfaces. In combination with properties 1 and 2 above, this wide range of high crystal quality nano-morphologies open even more potential applications [14 - 18].
4. P-type ZnO is predicted to display spin polarised carrier behaviour when doped with magnetic impurities and as such is a promising material for spintronics applications [16].
5. ZnO is bio-safe and biocompatible, and it can be directly used for biomedical applications without coating [19, 20].

With these unique characteristics, ZnO is one of the most important materials for future research and applications. Perhaps the three most important challenges in ZnO research generally are:

(a) The p-type doping problem: ZnO is a naturally unipolar semiconductor, like many other wide bandgap materials, e.g. GaN. However the solution to this problem in ZnO has proved far more difficult to date than for GaN [21].

(b) The high degree of surface activity: This can strongly affect electronic conduction mechanisms via creation of surface depletion and accumulation layers, altering the electronic characteristics. These effects vary over time and in different gas atmospheres and illumination levels. This means that reliable doping and measurements of doping are very difficult [22].

(c) Control of the nanostructure morphology: the wide variety of nanostructure morphologies in which ZnO can grow almost by definition means that the growth process is highly sensitive to growth conditions. Controlled growth of specific nanomorphologies and scaleable growth (i.e. growing uniformly on 1" – 2" substrates) and detailed understanding of the growth mechanisms still lag far behind the vast number of published data showing what can be grown (see section 1.2.1).

Zinc Aluminate, ($ZnAl_2O_4$)

Zinc aluminate ($ZnAl_2O_4$) material is also a well known direct, wide bandgap semiconductor with a cubic, spinel structure.

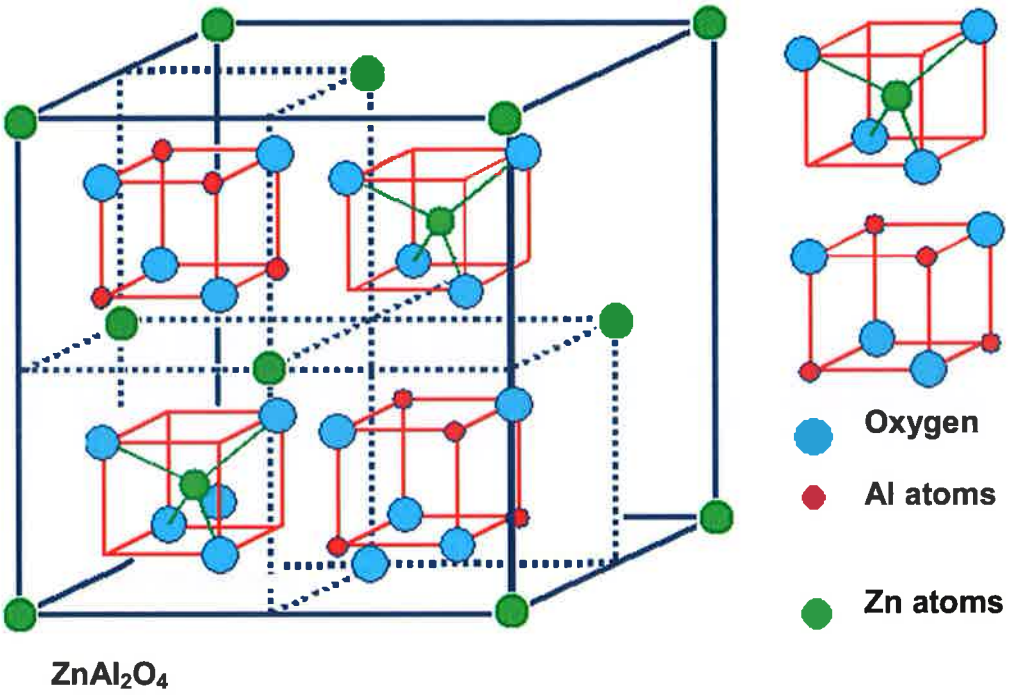

Figure 1.2 Crystal structure of zinc aluminate, adapted from [23].

Zinc aluminate ($ZnAl_2O_4$) is of interest technologically, and its wide potential functionalities are presented below:

1. It has a direct wide bandgap (~ 3.8 eV) [24]. This may lead to applications in transparent conducting oxide (TCO) films and high temperature electronics (HTE), and when doped with rare-earth elements, may function as an effective luminescent material for phosphor applications [25 - 28]. Zinc aluminate is also being considered for reflective optical coating applications in aerospace technology [29].
2. Zinc aluminate is used in many catalytic applications, including cracking, dehydration of saturated alcohols, synthesis of methanol and other alcohols etc. in addition to acting as a support for catalysis [30]. The catalytic functionality of materials, particularly for particles on the sub-micron scale, is known to be affected by the microstructure, and the activity of various facets show substantial differences in catalytic activity.

3. A recent report has used zinc aluminate as a platform material to demonstrate a novel technique for core-shell nanostructure synthesis using the nano-Kirkendall effect. The peculiar counter diffusion mechanisms of the Zn and Al atoms in the oxygen sublattice are rather unique to spinel materials and indicating the great potential this particular material has for nanoscale applications [31].

Controllable, ordered growth of microstructured catalytic material on a chemically and physically robust substrate is therefore an important technological focus and forms a general background for the work on zinc aluminate presented here.

1.2 Importance of Low Dimensional Nanostructures

Since the late 1980's and particularly after the discovery of carbon nanotubes in 1991, there have been significant research efforts worldwide to synthesize nanometre-scale various structures made from range of semiconductors and other materials. Major progress has already been made particularly in the field of zero- (0D) and two dimensional (2D) nanostructures (i.e. quantum dots and quantum wells, respectively). For example, using analogies with atomic systems and also basic quantum mechanical concepts of the "particle in a box" type interesting chemistry and physics has been learned, and many applications realised, by studying the evolution of nanostructure fundamental properties with size [32 - 34]. Using these quantum scale nanostructures as functional components, a variety of nanoscale devices have been fabricated as prototypes by many research groups around the world, with notable examples including quantum dot lasers [32], logic and memory units [33] and single electron transistors [34]. These would qualify as "revolutionary" nanotechnology. Of equal importance however is "evolutionary" nanotechnology where nanostructures have been used as building blocks for a range of devices where the small size has increased device performance or reliability (field effect transistors (FETs), p-n diodes, bipolar junction transistors) [35 - 39].

The main example of this evolutionary nanotechnology is the development of silicon-based microelectronics since the 1950's. The trend during this entire period has been towards smaller and smaller devices, leading to increased performance. Over this period device performance (e.g. in terms of processor speed, component density etc.) has doubled every 18 - 24 months, a trend known as "Moore's Law". This law, and the semiconductor roadmaps based upon it, implicitly assume that the current progress will continue and that device dimensions will be smaller and thus the devices will be faster and of higher density for memory applications. Challenges based on fundamental scientific limits are now beginning to affect the miniaturization paradigm which has been the dominant theme in electronics. These challenges are expected to limit the dramatic increase in computing speed. One of these challenges is to continue the miniaturization trend in electronics through improvements in established top-down, lithographically defined, fabrication techniques. One of the fundamental limits in this case is due to the finite device dimensions imposed by the diffraction limit of the radiation used in the lithography process.

Another important branch of nanotechnology which has developed strongly over the past decade is so-called "bottom-up" nanotechnology or self-organisation. This refers to situations where the intrinsic energetics of material growth leads to specific shapes on the nanoscale. Nature provides many examples of this type of nanotechnology, e.g. in the form and operation of DNA and proteins, and in many aspects of organic and polymer chemistry [40]. One of the key advantages of bottom-up nanotechnology is that lithographic pattern definition is not required, the energetic of the materials/molecules structure the system. This means that many of the limitations of lithography are not present, and also, in principle, such structures should be easily scaleable. However a key challenge is to ensure sufficient uniformity of self organisation over dimensions which would enable industrial applications.

1.2.1 ZnO Nanorods, Nanostructures & Applications

As mentioned previously ZnO naturally forms a wide variety of nanostructures with excellent crystal quality (superior to thin films and even bulk crystals in some cases) by a

self organisation process and thus recently significant research has been dedicated to exploring these aspects of ZnO material as part of the general trend towards the study of nanotechnology and self-organised processes generally among the scientific and materials communities. A great deal of attention has been focussed on synthesis and analysis of ZnO nanostructures due to their particular material properties, as discussed above. The combination of the material properties and self-organised nanostructure synthesis promise applications in optoelectronics, nanoelectronics, nanomechanics, nanoelectrochemical systems, and sensors (Table 1.1).

1.	OPTOELECTRONICS	* Optical devices, date storage [41] * Photodetectors [42] * Light emitting diodes (LEDs) [43] * Laser diodes (LDs) [44]
2.	NANOELECTRONICS	* Field-effect transistors [45] *Field emission sources [11]
3.	NANOMECHANICS	* Nanocantilevers [13]
4.	NANOELECTROCHEMICAL SYSTEM	* Biochemical and chemical sensors [46 - 48]

Table 1.1 Important application areas of ZnO nanostructures

1D and quasi 1D ZnO nanoscale structures, such as nanorods [14], nanowires [15], nanobelts [16], nanorod/nanowall [17], nanotubes [18] are ideal systems for investigating the dependence of optical properties, electrical transport and mechanical properties on size and dimensionality. They are expected to play an important role as both interconnects and functional components in the fabrication of nanoscale electronic and optoelectronic devices. Optical and electronic properties of nanomaterials are controlled by their size and shape [49, 50]. Therefore different nanostructures can have various applications. The key challenge for future nanotechnological applications is to control the size, structure and morphology of nanomaterials in order to control and tailor their properties.

We have synthesised single-crystalline ZnO nanorods using high temperature vapour phase transport using the vapour liquid solid growth mechanism in a self-organised process (Chapters 2, 3 & 4). From our SEM data the well aligned ZnO nanorods have a diameter typically in the range of 10 – 150 nm (average diameter 100 nm, std. dev). An example of the morphology of the ZnO nanorods grown in this way is shown in Figure 1.3 below.

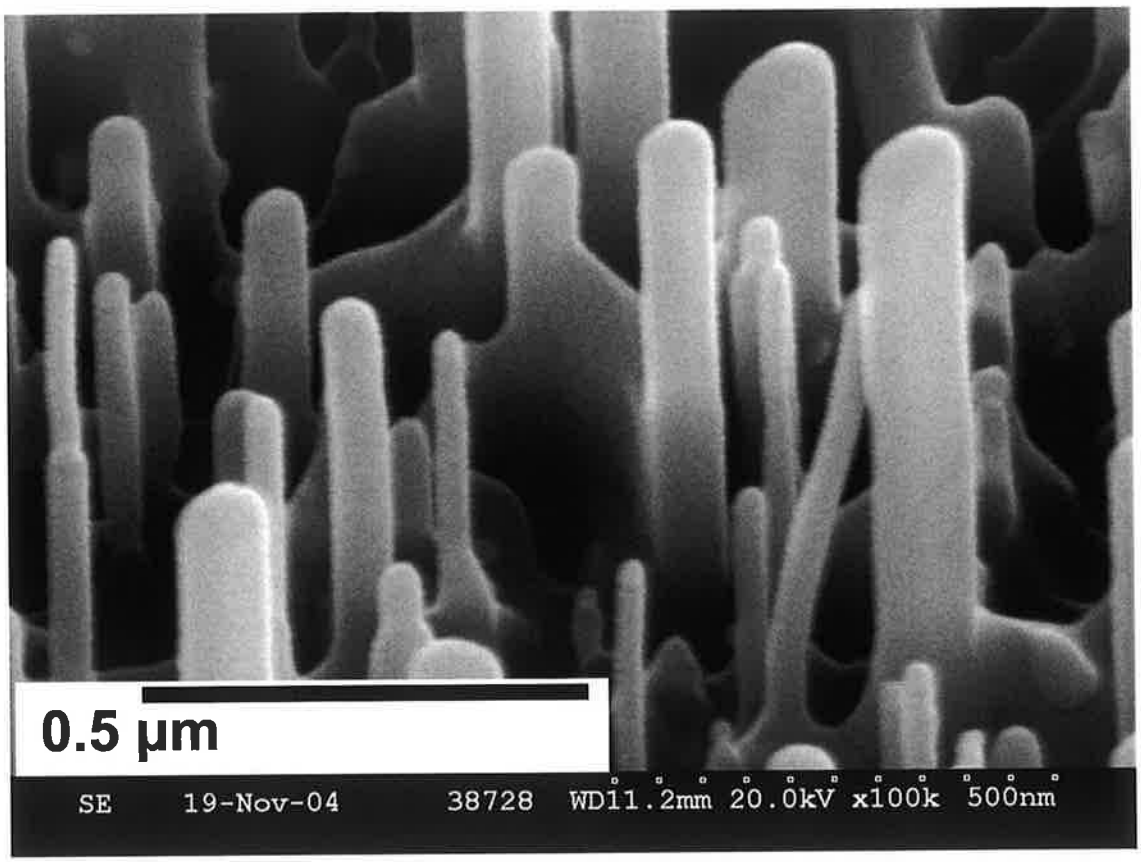

Figure 1.3 FESEM images of well aligned ZnO nanorods

From the narrower perspective of ZnO nanostructure research, perhaps the most important aims and challenges in current research are:

(1) Controlled growth is required to define nanostructure size, size distribution and shape. A thorough understanding of the growth mechanism(s) is the key to this control. In many cases, a suitable way to control the size and morphology of the

ZnO nanostructures is to properly control the temperature, catalyst conditions and growth time, etc.

(2) Techniques are required to grow the nanorods into aligned arrays, onto patterned substrates. Achieving this goal will enable superior performance of a variety of device architectures, including LEDs, LDs and field emission electronic sources where such alignment e.g. automatically generates multiple parallel lasing cavities in LDs and high field enhancement factors for field emission. Aligned arrays of nanostructures are easier to contact and also tend to present a more monodisperse surface area to volume ratio, which is important in sensor applications.

(3) For sensor applications, the nanorods may have the required sensitivity due to their morphology, but the selectivity needs to be improved. This may require the synthesis of composite nanobelts, such as heterostructures. Surface functionalization of the nanobelts is also an important direction [51].

(4) Ultimately the growth techniques should be scaleable for industrial level applications.

My thesis centres on point (1) and (2) above in relation to ZnO. I will explain the challenges involved in controlling size, distribution and shape of ZnO nanostructures using a very simple vapour transport technique. I will also try to draw some useful conclusions about a key point of this study which is to better understand the growth mechanism of ZnO nanostructures.

1.3 Outline of the Thesis

This thesis describes the growth and characterisation of various types of nanostructures of the wide bandgap semiconductors, zinc oxide (ZnO) and zinc aluminate ($ZnAl_2O_4$), using a technique known as Vapour Phase Transport (VPT). The various growth morphologies are summarized and their growth processes are proposed.

The thesis can be broadly grouped into two categories; relevant theory of the materials involved and experimental study of the behaviour of these materials in the VPT environment. It is outlined accordingly with chapters one to three dealing with material properties, applications and preparation as well as covering some theory of VPT growth, while chapters four to seven discuss the experimental results of zinc oxide and zinc aluminate nanostructures. The individual chapter contents can be summarised as follows:

Chapter 1: Introduction, Material Properties, Potential Applications and Novel Devices

This chapter provides a brief discussion on the properties and importance of zinc oxide and zinc aluminate materials and nanostructures and potential for future technology.

Chapter 2: Theory of Growth

This chapter describes the growth mechanism of zinc oxide nanorods and zinc aluminate domains. This growth appears to proceed by variety of mechanisms including the vapour liquid solid (VLS) mechanism with Au catalyst and vapour solid (VS) mechanism without Au catalyst.

Chapter 3: Equipment and Characterisation Techniques

In this chapter the core apparatus for zinc oxide nanostructure and zinc aluminate domain growth and characterisation are discussed in detail. The chapter is divided into three main sections; basic nanostructure growth equipment (the commissioning of which formed a substantial part of the initial thesis work), material preparation procedures for ZnO and $ZnAl_2O_4$ growth, and finally description of the equipment used to characterize zinc oxide and zinc aluminate.

Chapter 4: Well Aligned Zinc Oxide (ZnO) Nanorods and Nanowalls

In this chapter a study of growth of ZnO nanorods is presented and the issues affecting growth control are discussed. The detailed morphology is very sensitive to growth conditions. To control the size and morphology of the zinc oxide nanostructures we have to properly focus on various parameters like: growth temperature, duration, growth steps, and catalyst conditions. Our results show that a variety of ZnO nanostructure morphologies (rods, wires, mixed rods/walls) can be fabricated by controlling the growth parameters.

Chapter 5: PL Study of the Zinc Oxide Nanorods/Nanowalls System

In this chapter a detailed study of the ZnO nanorods/nanowalls morphology mentioned in chapter 4 is presented, concentrating on the optical properties. One key outcome of this study was the realization that the nanostructures in this case have extremely bright optical emission at low temperatures (~ 7 K) which is strongly quenched at room temperatures which in turn has implications for device applications of this nanostructure morphology.

Chapter 6: Self-Organized Zinc Aluminate ($ZnAl_2O_4$) on *c*-Sapphire

This chapter presents a detailed study of the growth of zinc aluminate domains with well defined epitaxial relationships on *c*-sapphire substrates. These microstructures show a number of interesting features, including well-defined epitaxial relationships to the substrate and two types of twin boundary, with the nature of these relationships dependent on the growth duration at high growth temperatures.

Chapter 7: Conclusions and Future Work

Finally, the last chapter concludes with some general conclusions and gives some perspectives on future research work which remains to be carried out as a continuation of the work presented in this thesis.

1.4 References

[1] M. Law, D. J. Sirbuly, J. C. Johnson, J. Goldberger, R. J. Saykally, P. Yang, *Science* **305** (2004) 1269

[2] R. W. Hill, C. Proust, L. Taillefer, P. Fournier, R. L. Greene, *Nature* **414** (2001) 711

[3] J. F. Scott, *Science* **315** (2007) 954

[4] G. S. D. Beach, A. E. Berkovitz, *IEEE Transactions on Magnetics* **41** (2005) 2043

[5] Y. Choongho, H. Qing, S. Sanjoy, S. Li, K. Xiangyang, Z. L. Wang, *Applied Physics Letters* **86** (2005) 063101

[6] U. Ozgur, Ya. I. Alivov, C. Liu, A. Teke, M. A. Reshchikov, S. Dogan, V. Avrutin, S.-J. Cho, H. Morkoc, *Journal of Applied Physics* **98** (2005) 041301

[7] http://staff.ustc.edu.cn/~bxlin/index_e.htm

[8] W. I. Park, D. H. Kim, S.-W. Jung, G.-C. Yi, *Applied Physics Letters* **80** (2002) 4232

[9] M. H. Huang, S. Mao, H. Feick, H. Yan, Y. Wu, H. Kind, E. Weber, R. Russo, P. Yang, *Science* **292** (2001) 1897

[10] M. Zhao, Z. L. Wang, S. X. Mao, *Nano Letters* **4** (2004) 587

[11] C. J. Lee, T. J. Lee, S. C. Lyu, Y. Zhang, H. Ruth, H. J. Lee, *Applied Physics Letters* **81** (2002) 3648

[12] E. Comini, G. Faglia, G. Sberveglieri, Z. W. Pan, Z. L. Wang, *Applied Physics Letters* **81** (2002) 1869

[13] W. Hughes, Z. L. Wang, *Applied Physics Letters* **82** (2003) 2886

[14] J. Grabowska, K. K. Nanda, E. McGlynn, J.-P. Mosnier, M. O. Henry, A. Beaucamp, A. Meaney, *Journal of Material Science: Materials in Electronics* **16** (2005) 397

[15] J. Grabowska, K. K. Nanda, E. McGlynn, J.-P. Mosnier, M. O. Henry, *Surface & Coatings Technology* **200** (2005) 1093

[16] C. Ronning, P. X. Gao, Y. Ding, Z. L. Wang, *Applied Physics Letters* **84** (2004) 783

[17] J. Grabowska, A. Meaney, K. K. Nanda, J.-P. Mosnier, M. O. Henry, J.-R. Duclere, E. McGlynn, *Physical Review B* **71** (2005) 115439

[18] Y. J. Xing, Z. H. Xi, Z. Q. Xue, X. D. Zhang, J. H. Song, *Applied Physics Letters* **83** (2003) 1689

[19] Z. L. Wang, J. Song, *Science* **312** (2006) 242

[20] X. Wang, J. Song, J. Liu, Z. L. Wang, *Science* **316** (2007) 102

[21] For a review, see S. Nakamura and G. Fasol, The Blue Laser Diode (Spring-Verlag, Berlin, 1997)

[22] S. B. Zhang, S.-H. Wei, A. Zunger, *Journal of Applied Physics* **83** (1998) 3192

[23] www.tf.uni-kiel.de/matwis/amat/def_en/kap_2/basics/b2_1_6.html

[24] S. K. Sampath and J. F. Cordaro, *Journal of the American Ceramic Society* **81** (1998) 649

[25] H. Kim, C. M. Gilmore, J. S. Horwitz, A. Pique, H. Murata, G. P. Kushto, R. Schlaf, Z. H. Kafafi, D. B. Chrisey, *Applied Physics Letter* **76** (2000) 259

[26] R. Padney, J. D. Gale, S. K. Sampath, J. M. Recio, *Journal of American Society* **82** (1999) 3337

[27] S. Mathur, M. Veith, M. Hass, H. Shen, N. Lecerf, V. Huch, S. Hufner, R. Heberkoru, H. P. Beck, M. Jilabi, *Journal of American Ceramic Society* **84** (2001) 1921

[28] B. Cheng, S. Qu, H. Zhou, Z. Wang, *Nanotechnology* **17** (2006) 2982

[29] T. El-Nabarawy, A. A. Attita, N. Alaya, *Materials Letters* **24** (1995) 319

[30] J. Wrzyszcz, M. Zawadzki, J. Trawczynski, H. Grabowska, W. Mista, *Applied Catalysis A* **210** (2001) 263

[31] H. J. Fan, M. Knez, R. Scholz, K. Nielsch, E. Pippel, D. Hesse, M. Zacharias, U. Gosele, *Nature Materials* **5** (2006) 627

[32] V. I. Kilmov, A. A. Mikhailovsky, S. Xu, A. Malko, J. A. Hollingsworth, C. A. Leatherdale, H. J. Eisler, M. G. Bawendi, *Science* **290** (2000) 314

[33] T. Rueckes, K. Kim, E. Joselevich, G. Y. Tseng, C. L. Cheung, C. M. Lieber, *Science* **289** (2000) 94

[34] D. L. Klein, R. Rroth, A. K. L. Lim, A. P. Alivisatos, P. L. McEuen, *Nature* **389** (1997) 699

[35] Y. Cui, C. M. Lieber, *Science* **291** (2001) 851

[36] Y. Huang, X. F. Duan, Y. Cui, L. J. Lauhon, K. H. Kim, C. M. Lieber, *Science* **294** (2001) 1313

[37] J. Y. Yu, S. W. Chung, J. R. Heath, Silicon Nanowires: Preparation, *Journal of Physical Chemistry B* **104** (2000) 11864

[38] Y. Cui, X. F. Duan, J. T. Hu, C. M. Lieber, *Journal of Physical Chemistry B* **104** (2002) 5213

[39] S. W. Chung, J. Y. Yu, J. R. Health, *Applied Physics Letters* **76** (2002) 2068

[40] H. Yan, S. H. Park, G. Finkelstein, J. H. Reif, T. H. LaBean, *Science* **301** (2003) 1882

[41] H. T. Ng, J. Li, M. K. Smith, P. Nguyen, A. Cassel, J. Han, M. Meyyappan, *Science* **300** (2003) 1249

[42] Z. R.Tian, J. A. Voigt, J. Liu, B. McKenzie, M. J. McDermott, M. A. Rodriguez, H. Konishi, H. Xu, *Nature Materials* **2** (2003) 821

[43] A. Tsukazaki, A. Ohtomo, T. Onuma, M. Ohtani, T. Makino, M. Sumiya, K. Ohtani, S. F. Chichibu, S. Fuke, Y. Segawa, H. Ohno, H. Koinuma, M. Kawasaki, *Nature Materials* **4** (2005) 42

[44] W. Yang, R. D. Vispute, S. Chooun, R. P. Sharma, T. Venkatesan, H. Shen, *Applied Physics Letters* **78** (2001) 2787

[45] M. S. Arnold, Ph. Avouris, Z. W. Pan, Z. L. Wang *Journal of Physical Chemistry B* **107** (2003) 659

[46] E. Comini, G. Faglia, G. Sberveglieri, Z. W. Pan, Z. L. Wang *Applied Physics Letters* **81** (2002) 1869

[47] H. T. Wang, B. S. Kang, F. Ren, L. C. Tien, P. W. Sadik, D. P. Nortan, S. P. Pearton, J. Lin, *Applied Physics Letters* **86** (2005) 243503

[48] M. Law, H. Kind, F. Kim, B. Messer, P. Yang, *Angewandte Chemie International Edition* **41** (2002) 2405

[49] J. Jortner, C. N. R. Rao, *Pure and Applied Chemistry* **74** (2002) 1489

[50] G. Schmidt, *Nanoparticles: From Theory to Applications,* New York: Wiley, 2004

[51] X. D. Bai, P. X. Gao, Z. L. Wang, *Applied Physics Letters* **82** (2003) 4806

2 Theory of Growth

Growth of zinc oxide nanostructures has been reported both catalysed by Au nanoclusters and uncatalysed on bare substrates, and appears to proceed by variety of mechanisms including the vapour liquid solid (VLS) mechanism with Au catalyst and vapour solid (VS) mechanism without Au catalyst. In this chapter I will present these two mechanisms which are very well known and widely reported. However, neither mechanism is as yet fully understood for zinc oxide and zinc aluminate growth. In the particular experiments reported in this thesis sample growth used the Vapour Phase Transport technique. In the work in this thesis for growth on Au coated a-plane sapphire ZnO nanorods are synthesised with their c-axis perpendicular to the substrate via the VLS mechanism. For growth on bare (i.e. without Au catalyst coating) c-plane sapphire, zinc aluminate domains tend to grow on the substrate via the VS mechanism.

2.1 Vapour Liquid Solid (VLS) Mechanism

A well accepted mechanism of nanorod growth via gas phase reaction of relevance to this thesis is called the Vapour Liquid Solid (VLS) process. In 1965 Wagner and Ellis proposed the VLS mechanism during studies of large single crystalline Si whisker growth. In the series of experiments they showed that epitaxial deposition of silicon whiskers on a Au coated silicon substrate occurred when silicon condensed from the vapour (V) at the Au liquid alloy surface and then dissolved in the liquid (L) to form an eutectic alloy solution. Upon supersaturation of this alloy, silicon was precipitated out and grew at the interface between the liquid droplet and the silicon substrate as a solid (S) whisker whose diameter was controlled to some extent by the dimensions of the Au droplets [1].

In our study, we have grown well aligned ZnO nanostructures using predominantly the same type of VLS mechanism. The growth mechanism of conventional whiskers involves the participation of vapour, liquid, and solid phase (VLS) in the growth process (illustrated below in Figure 2.1). Because ZnO is a compound semiconductor the growth process is slightly more complicated then for elemental semiconductor such as Si.

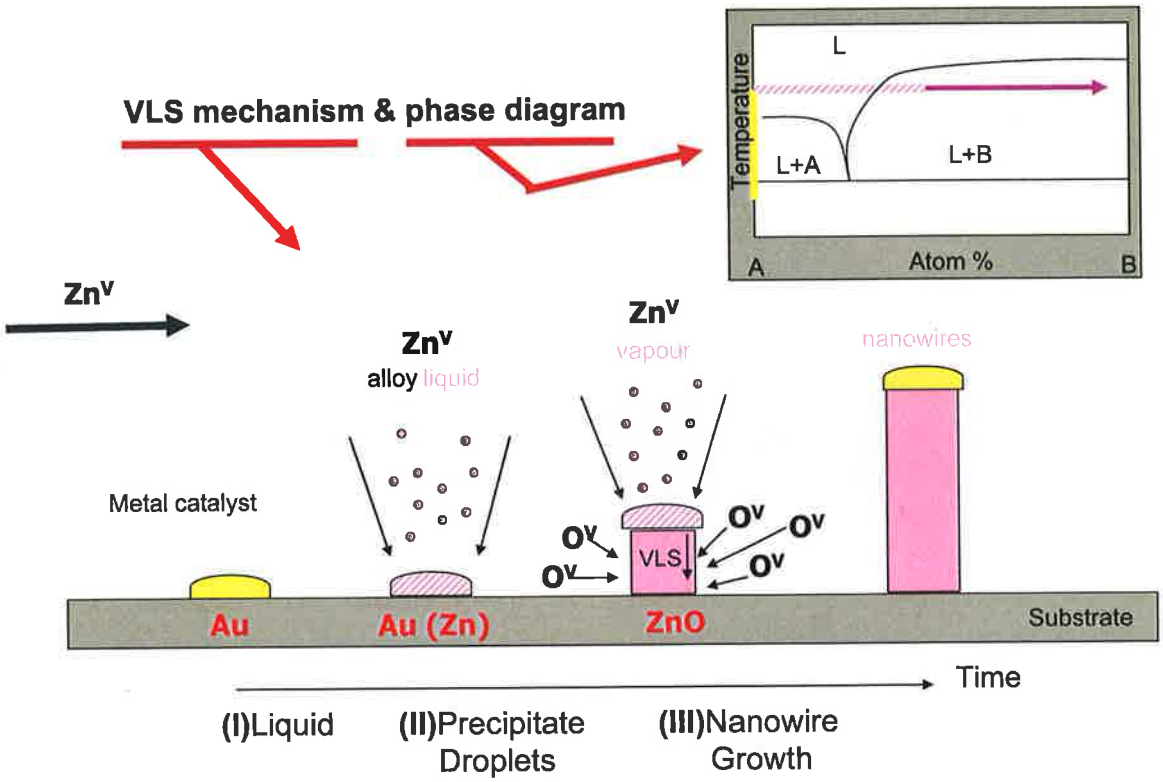

Figure 2.1 VLS mechanism with the general phase diagram.

The formation of ZnO nanorods using the VLS technique involved at least five different stages:

1. Metal (Au) thin film (~ 2 nm) deposition on substrate at or close to room temperature
2. When the coated substrate is placed at high temperature region (> 900 °C) in a furnace where a source of Zn vapour is generated (see section on carbothermal reduction below) two key events occur:
    a. Catalytic Au nanoclusters formation due to capillarity induced beading of Au thin film at high growth temperatures
    b. Nucleation/condensation/dissolution of Zn vapour at catalytic Au nanoclusters locations
3. When the Au-Zn alloy reaches a certain solubility of Zn, Zn metal will begin to precipitate out at the interface between the droplet and surface
4. The precipitating Zn metal will oxidize due to the residual oxygen in the chamber. Oxygen is also sometimes intentionally introduced in the gas flow.

5. This ultimately leads to epitaxial growth of ZnO nanorods (with a Au "cap") on the substrate whose diameters are related to the diameters of the catalytic Au nanoclusters

We now discuss some of these stages in more detail. The growth generally takes place in a horizontal tube furnace with a carrier gas flow (Ar in our case) which will be described in more detail in chapter 3.

The Zn vapour is generated by a process known as carbothermal reduction of ZnO by carbon (graphite powder in our case). Zn vapour can be generated by the reduction of ZnO powder by graphite and CO(g) at high temperatures. The temperatures required can be determined by using so-called Ellingham diagrams [2]. For ZnO these diagrams predict that the following reactions take place at ~ 950 °C:

(1) $ZnO(s) + C(s) \rightarrow Zn(g) + CO(g)$

(2) $ZnO(s) + CO(g) \rightarrow CO_2(g) + Zn(g)$

The Zn vapour is transported to a lower temperature region (downstream of carrier gas flow) where it is absorbed by catalytic nanoclusters on the sample (as described above). The substrate used for ZnO nanorod growth was generally *a*-plane sapphire. This is coated with a thin film (20 Å) of Au (by a bell jar evaporator). This beads up into liquid nanoclusters at high temperatures close to the Au melting point, though size dependent and eutectic alloying effects can lower the melting temperature below the bulk value, as discussed in chapter 4. These metal clusters acts as the energetically favored site for absorption of gas-phase reactants. Zn vapour condenses into liquid Au nanoclusters and increasing amounts of Zn dissolution leads to formation of an Au-Zn liquid alloy. Above a certain supersaturation the Zn metal will precipitate out and oxidize by reaction with residual oxygen in the chamber to form ZnO nanostructures by the following reaction.

(3) $Zn(l) + \frac{1}{2}O_2(g) \rightarrow ZnO(s)$

In support of the mechanism proposed above (which is quite standard in the literature) we note the following observations. Firstly, we flush the (initially air-filled) quartz furnace tube with Ar gas for 10 minutes prior to turning on the furnace and when the furnace is switched on it reaches the growth temperature in 20 minutes. The Ar flow rate during the entire process is 90 sccm. The quartz tube inner diameter is ~ 4 cm and the length is 120 cm, yielding a volume of ~ 1500 cm^3. An Ar flow of 90 sccm will replace this volume of air in 1500/90 = 16 minutes. However the actual time to fully replace the air is likely to be somewhat longer than this because the gas flow in quite slow and significant diffusion and mixing is likely to occur in addition to some boundary layer effects close to walls in the system where the effects of the Ar gas flow are limited. However, other experiments using this system, made by a colleague, Dr. R.T. Rajendra Kumar, where the tube was flushed for ~ 45 minutes before switching on the furnace yield no ZnO growth. This is consisten with the hypothesis that the residual air in the chamber is the source of the oxygen and that this is displaced fully on a timescale of 45 minutes in a 90 sccm Ar flow. Furthermore we observe that both a white deposited layer (in the higher temperature region close to the centre, temperature region ~ (250 – 700 °C)) and a black deposited layer (close to the ends at lower temperatures, temperature region ~ (150 – 250 °C)) are deposited on the inner walls of the quartz tube after growths (at both ends, with the nominal furnace temperature ~ 950 °C, shown in chapter 3). The fact that this deposition is seen at both end of the tube (upstream and downstream) indicates that diffusion effects are very important in the growth regime we work in, i.e. the gas flow does not drive all deposition to the downstream end. We have checked these depositions with XPS measurements which show the white layers are ZnO and the black layers are unoxidised metallic C. This is consistent with the Zn vapour flowing in the tube, and depositing on the sidewalls (in addition to the growth substrate) where it is oxidized rapidly in the high temperature furnace centre, and only carbon is carried feather down. However it is worthwhile noting that some aspects of this explanation, which, although common in the literature, seem at odds with known material aspects in some regards.

Firstly, the alloying process between Au and Zn is shown in the Au-Zn phase diagram in Figure 2.2 below and an isothermal line at ~ 1000 °C is shown. The alloy formation at this

temperature seems to allow a continuous solubility (i.e. complete miscibility) of Zn in Au, either in liquid or solid phase alloy, or both. There is no evidence of a critical point at which pure Zn metal precipitates out. One possible explanation is that the precipitation (and hence ZnO growth) occurs only at the end of the growth period as the furnace cools but this is at odds with data to be presented subsequently where there is evidence that growth time affects the morphology in various ways, and the discussion above concerning the loss rate of residual oxygen from the furnace due to the Ar flow which should discriminate against growth at longer times. The second objection to this hypothesis is that it appears that a 3 - 4 % solid solution of Zn in Au is stable at room temperature in addition to various other phases. X-ray diffraction data on our samples show no evidence of such alloys or phases under any circumstances, and all the sample-related reflections can be indexed to either ZnO or (occasionally) Au. There is also evidence from the literature, e.g. XRD, EDX & TEM studies that the Au particulates found on top of ZnO nanorods grown by VLS are (within detection limits) pure Au rather than alloys [3 - 5].

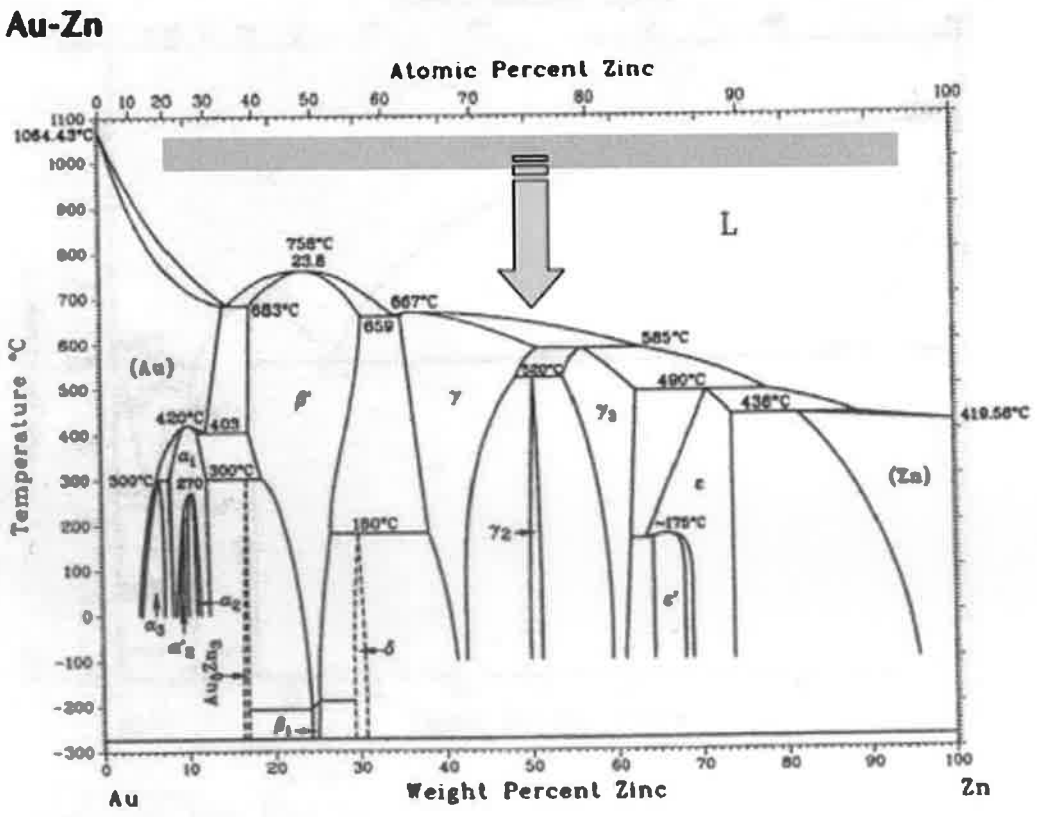

Figure 2.2 Au-Zn Binary Phase Diagram. The potential range of Zn concentration in the gold droplet is shown by the gray bar.

A second possible explanation is that the presence of a reactive oxygen atmosphere substantially changes the thermodynamics which rule the phase diagram (i.e. change the phase diagram), and that at high growth temperatures, above certain Zn concentrations in the Au-Zn alloy droplet it is energetically favorable for Zn to precipitate out to react with oxygen rather than stay in solution (particularly in nanoscale structures with a large surface to volume ratio). This stripping of Zn from the alloy droplet may continue as the system cools to leave pure Au droplets on top of ZnO nanorods. This suggestion closely parallels effects seen in GaAs and InAs nanorods grown by VLS [6] where the As atmosphere leads to a stripping of group II compound from the catalyst droplet.

It is also worth noting that the detailed growth mechanism when ZnO nanorods grow in an Au coated portion of a substrate seem to vary substantially from substrate to substrate, e.g. from Si to sapphire, and also from one surface termination to another (*c*-sapphire to *a*-sapphire). These are often lumped under the heading "VLS" in the literature but there is increasingly strong evidence [7] that the classic VLS mechanism as described above is not appropriate to e.g. ZnO nanorod growth on Au coated Si substrates. However, for growth on Au coated *a*-sapphire substrates the description above appears to correctly describe the growth mechanism (taking into account the provisos in the two previous paragraphs). Because most of our ZnO nanorod growth is on Au coated *a*-sapphire substrates we have presented the description of VLS growth most appropriate to this case and not elaborated on the wider variations.

The advantage of the growth of nanorods via the VLS method is that the diameter and length of the nanorods can be controlled easily by controlling the growth time and the diameter of catalytic Au clusters (either using colloidal Au particles or various thickness deposited Au thin films). Additionally, nanorods only grow in regions where Au has been deposited so that the location of the structures can be easily controlled by shadow masking or other lithographic definition of the Au thin film.

Initial experimental results (Figure 2.3) which were actually taken for ZnO nanorods grown on *c*-plane sapphire clearly show the VLS mechanism at work. Figure 2.2 shows a FESEM image with an Au tip on the top of zinc oxide nanorods.

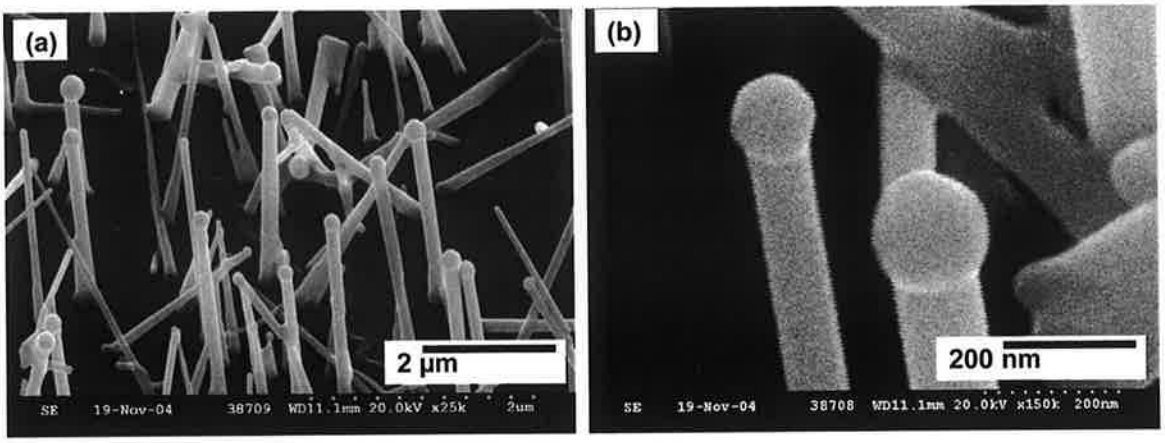

Figure 2.3 FESEM images of zinc oxide nanorods with Au tip on the top of zinc oxide rod, low magnification (a), high magnification (b)

2.2 Vapour Solid (VS) Mechanism

The second important mechanism for nanostructure growth of relevance to this thesis is the classical vapour solid (VS) method [1]. In this process, Zn vapour is first generated either by evaporation or carbothermal reduction (in our work) as described previously. The vapour is subsequently transported and condensed directly onto substrate without the intermediate stage of a liquid catalytic droplet. Oxidation then occurs to form ZnO nanostructures as previously. In our study we have grown zinc aluminate domains on bare (i.e. not coated with Au) *c*-sapphire substrates via this mechanism and the data is presented in the chapter 6 (an example is shown in Figure 2.4 below). The zinc aluminate formed when the VS deposited ZnO layer reacted with sapphire to form the aluminate compound.

The VS method for the growth of ZnO and related nanostructures is significantly different to the VLS method. The prime consideration for VS growth of ZnO nanostructures growth is the supersaturation of Zn vapour. Whereas the VLS method offers energetically attractive nucleation sites at which Zn vapour may condense from the gas flow, the absence of these

in VS growth means that the driving force for nucleation is less. This means either that (i) any coverage will be quite thin or (ii) that nucleation will occur preferentially at substrate regions where there are imperfections (e.g. dislocations threading to the surface) which offer energetically attractive nucleation sites [8]. This is fully consistent with our data on zinc aluminate in chapter 6 where the appearance of large aluminate domains are closely correlated with the presence of substrate imperfections, and where aluminate coverage is very low on more perfect substrates.

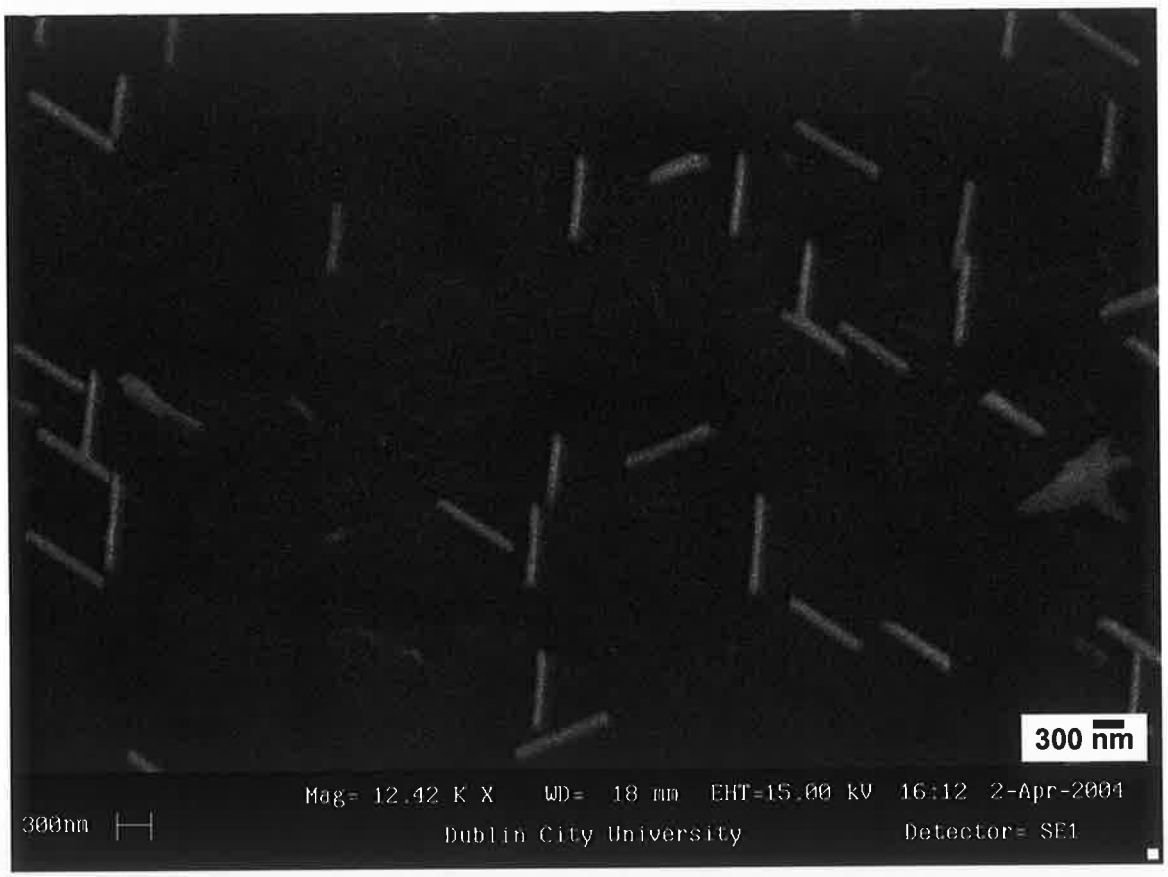

Figure 2.4 SEM image of zinc aluminate domains on c-plane sapphire

2.3 References

[1] Whisker Technology, Levitt A. P. Eds. Wiley-interscience, New York, 1970

[2] P. W. Atkins, book, *Physical Chemistry*, 5th edition, Oxford University Press (1994). Ellingham diagrams, Chapter 10, R. T. Dehoff, Thermodynamics in Material Science, McGraw-Hill, New York (1993)

[3] M. H. Huang, Y. Y. Wu, H. Feick, N. Tran, E. Weber, P. D. Yang, *Advanced Materials* **13** (2001) 113

[4] B. Nikoobakht, A. Davydov, S. J. Stranick, *Materials Research Society Symposium Proceedings* **818** (2004) M8.25

[5] D. Zhao, C. Andreazza, P. Andreazza, J. Ma, Y. Liu, D. Shen, *Chemical Physics Letters* **399** (2004) 522

[6] A. I. Persson, M. W. Larsson, S. Stenstrom. B. J. Ohlesson, L. Samuelson, L. R. Wallenberg, *Nature Materials* **3** (2004) 677

[7] Y. Li, M. Feneberg, M. Schirra, R. Enchelmaier, A, Ladenburger, A. Langlois, R. Sauer, K. Thonke, J. Cai, H. Rauscher, *Journal of Applied Physics* **99** (2006) 054307

[8] W. K. Burton, N. Cabrera, F. C. Frank, *Philosophical Transactions of the Royal Society* **A243** (1951) 299

3 Equipment and Characterization Techniques

In this chapter the core apparatus for zinc oxide nanostructure and zinc aluminate domain growth and characterisation are discussed in detail. The chapter is divided into three main sections; basic nanostructure growth equipment specifications, material preparation procedures for ZnO and $ZnAl_2O_4$ growth, and finally the specifications of the equipment for zinc oxide and zinc aluminate characterization.

3.1 Vapour Phase Transport Deposition System

In the last few years, several methods including metalorganic chemical vapour deposition (MOCVD) [1], physical vapour deposition (PVD) [2], pulsed laser deposition (PLD) [3] etc. have been employed to synthesize 1D oxide nanostructures. Vapour phase transport (VPT) is a form of thermal evaporation and is one of the simplest and most effective approaches to obtain ZnO nanostructures [4], and it has been employed to fabricate many of the ZnO nanostructures reported at the earliest stages of the recent upsurge in ZnO research. The simplicity of the technique is attractive, in that only a single zone horizontal tube furnace is required in addition to a Zn vapour source and substrate. The fact that largely similar tube furnace designs are used on large area wafers in various commercial semiconductor fabrication facilities for oxide growth, epitaxial growth, dopant diffusion etc. indicates that the technique may be more inherently scaleable than techniques such as PLD. However our data, reported later, indicate that growth of ZnO nanostructures is highly sensitive to variations in a wide range of growth parameters, which casts doubt on the scaleability of the VPT process.

The basic idea of this method is to evaporate source materials at high temperature in a tube furnace. The vapour is then transported in a carrier gas and subsequently deposited in a different part of the furnace (where the temperature is determined by the furnace profile) to form the desired nanostructures.

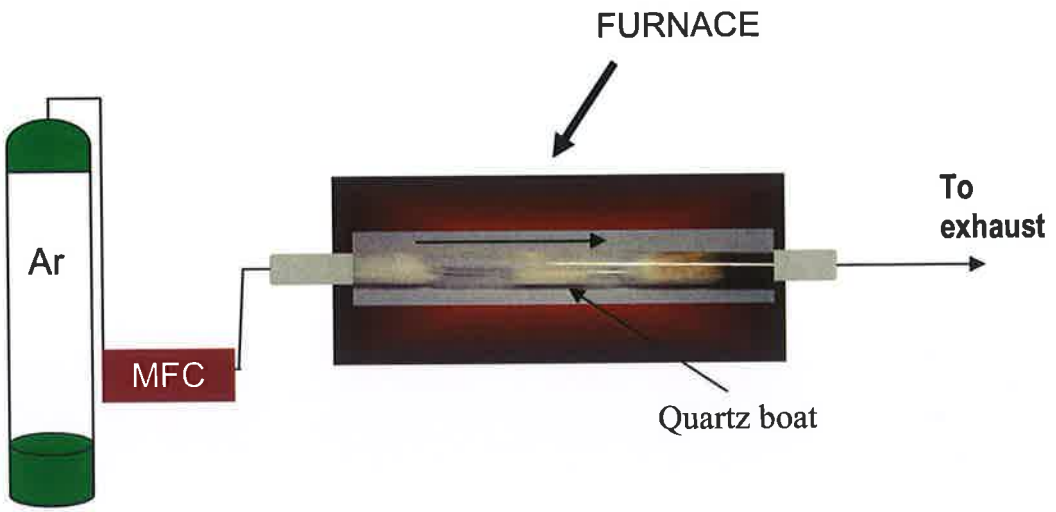

Figure 3.1 Thermal evaporate deposition system for synthesis of 1D nanostructures

The first part of my Ph.D. research involved setting up the growth system shown in Figure 3.1 in collaboration with a colleague, Dr. Karuna Kar Nanda. Figure 3.1 shows a schematic diagram of the experimental apparatus used in the studies presented here. A Lenton horizontal tube furnace (56 cm long, LTF model, serial number 3210) was used. This has a maximum temperature rating of 1600 °C and uses a Eurotherm controller model 818P/TC/RLGC/. A ceramic alumina line tube (4.6 cm inner diameter, 90 cm long) is placed in the furnace and a quartz tube (3.7 cm in diameter, 120 cm long) is placed co-axially inside the liner. Ar (99.999 %) is used as a carrier gas and the flow rate is controlled by a mass flow controller (MFC).

Our synthesis is based on generating source Zn vapour by the carbothermal reduction of ZnO and graphite powders, discussed in chapter 2. The synthesis is performed in the quartz tube. High purity (99.9995 %) ZnO and graphite powders are mixed well together by mechanical mixing in a mortar and pestle for 2 minutes. The typical masses of ZnO and C are 0.06 g to give a total powder mass of 0.12 g. The powder mixture is placed in an alumina boat and positioned in the middle of the furnace, which is at the highest temperature. The substrates for collecting the vapour produced are normally placed down stream of the source powder, generally still in the boat, as shown in Figure 3.2. This figure also shows typical temperature ranges for the source and substrate. The substrate can be a

silicon wafer, single crystal alumina (sapphire) or zinc oxide. Both ends of the tube are covered by stainless steel caps and sealed with rubber O-rings. All gas fittings are Swagelok DN25-0.75 inch stainless steel fittings. There is a facility to evacuate the quartz tube to ~ 1 x 10^{-2} mbar, but we have not used this for the results presented in this thesis.

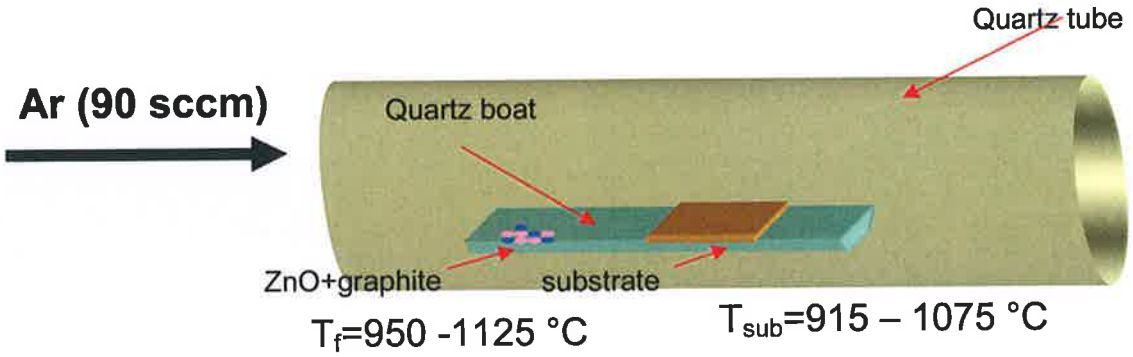

Figure 3.2 Quartz tube with the quartz boat inside ready for deposition

The difference in temperature between the source and substrate is controlled by careful positioning of the substrate with respect to the source, based on knowledge of the furnace temperature profile shown in Figure 3.3. This profile was regularly re-checked (3 monthly intervals).

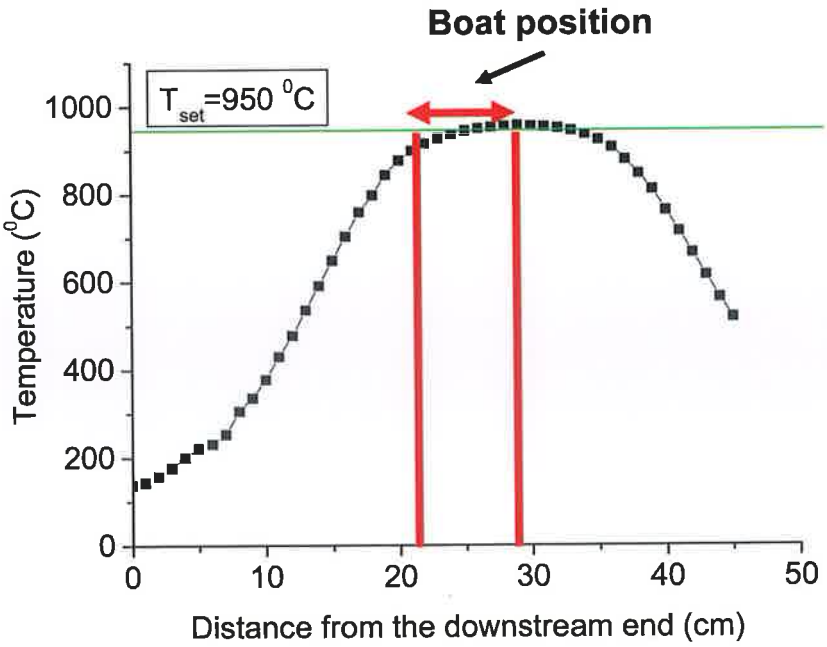

Figure 3.3 Temperature profile of the furnace

The typical growth procedure is to flush the tube with Ar at 90 sccm flow rate for 10 minutes prior to turning the furnace on. The furnace reaches set values of 950 °C in a time of ~ 20 minutes. Growth then proceeds for the required time and growth is terminated when the furnace is turned off. The system is then cooled down to room temperature by flowing inert gas such as Ar.

There are several processing parameters, such as source and substrate temperature, carrier gas (including gas purity class and its flow rate), substrate material type and orientation, and evaporation time period, that can be controlled and need to be selected properly before and/or during the thermal evaporation. Some basic considerations and knowledge of the literature enable us to establish appropriate ranges for many of these parameters. The choice of source temperature mainly depends on the requirement to drive the carbothermal reduction process in the source material. From the Ellingham diagram this reaction proceeds spontaneously at and above ~ 950 °C, though low partial pressures of Zn vapour can be produced at lower source temperatures (down to 850 °C). The substrate temperature usually drops as a function of the distance from the position of source material: the greater the distance, the lower the substrate temperature. The substrate temperature is a key parameter and one that I have examined in some detail during my Ph.D. Selecting a proper evaporation time is also important because it influences not only the amount but also the size and the morphology of the product. Some preliminary investigations were undertaken to quantify the source evaporation rate in terms of mass loss and the effects of aging on the source powder.

3.1.1 Rate of Evaporation as a Function of Temperature

In order to choose a suitable experimental condition for the growth of ZnO nanorods, we initially studied the evaporation rate as a function of furnace temperature and the results are plotted in Figure 3.4. The evaporation rate was gauged by measuring the mass difference in the boat + source powder before and after a 30 minutes growth run (in addition to the ramp-up and cool-down times).

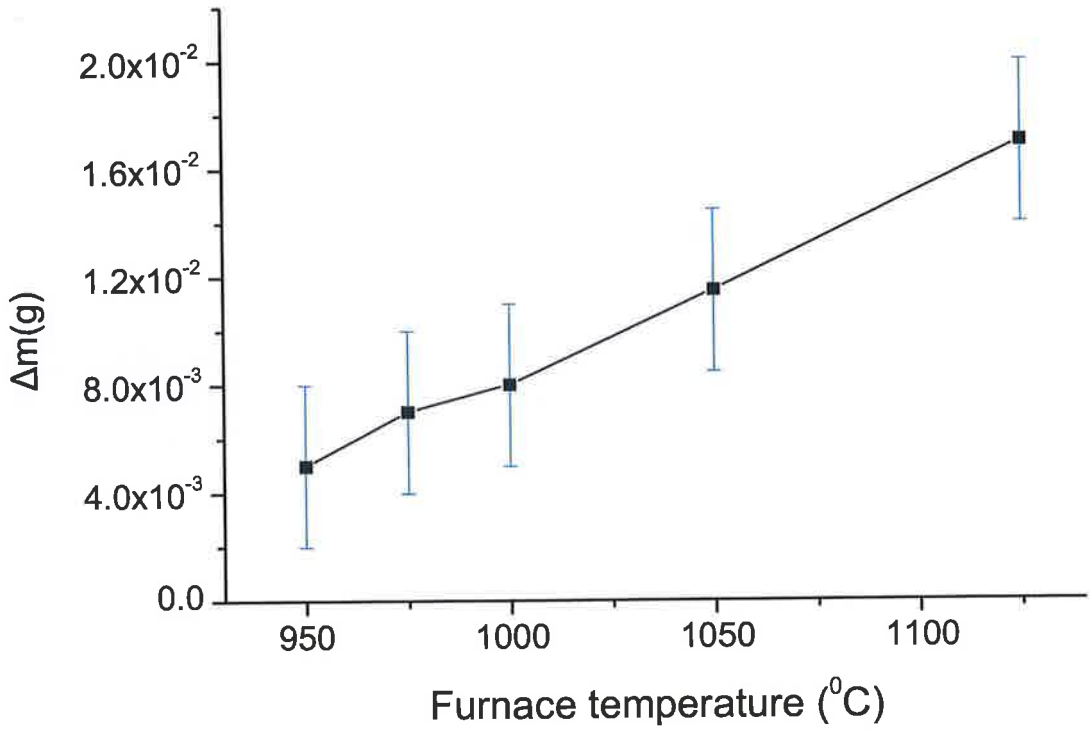

Figure 3.4 Rate of evaporation as a function of (a) time and (b) furnace temperature

The evaporation rate increases with increasing furnace temperature showing an almost linear behaviour in the temperature range 950 – 1130 °C. The majority of our experimental work was conducted in this same temperature range.

3.1.2 Effects of Aging on Source Powder

Another initial study undertaken was to ascertain the effects (if any) on the source powder from aging. Specifically we wished to know how important it is to use fresh ZnO + C powder supply for each deposition run. We did three experiments, one after the other (all under identical conditions of ramp-up, growth at 950 °C for various time and cool-down with Ar gas flow) to check the weight of ZnO deposition without changing the ZnO + C powder, measuring the mass loss between the start and end of each experiment. For the first experiment, we used fresh ZnO + C powder. We used the same ZnO + C mixture for the subsequent depositions.

I. Fresh powder (1st run; Cumulative time - 6 Hrs)

Mass before deposition: - a weight of the boat + (ZnO + C) powder = 12.040 g

Mass after deposition: - a weight of the boat + (ZnO + C) powder = 12.030 g

Deposited mass: 0.010 g

dm/dt = 0.00167 [g/hr]

II. Old powder (2nd run; Cumulative time - 6 Hrs + 24 Hrs)

Mass before deposition: - a weight of the boat + (ZnO + C) powder = 12.030 g

Mass after deposition: - a weight of the boat + (ZnO + C) powder = 12.019 g

Deposited mass: 0.011 g

dm/dt = 0.000458 [g/hr]

III. Old powder (3rd run; Cumulative time - 6 Hrs + 24 Hrs + 12 Hrs)

Mass before deposition: - a weight of the boat + (ZnO + C) powder = 12.019 g

Mass after deposition: - a weight of the boat + (ZnO + C) powder = 12.016 g

Deposited mass: 0.003 g

dm/dt = 0.00025 [g/hr]

We note that after all depositions, we notice white, wool-like ZnO products deposited on the walls of the alumina boat, indicating that we are not measuring the total mass loss of the powder. Nevertheless the mass loss we measure is an indication of the source reactivity.

These results of these experiments, shown in Figure 3.5 shows us very clearly that for each and every experiment we need to use fresh powder.

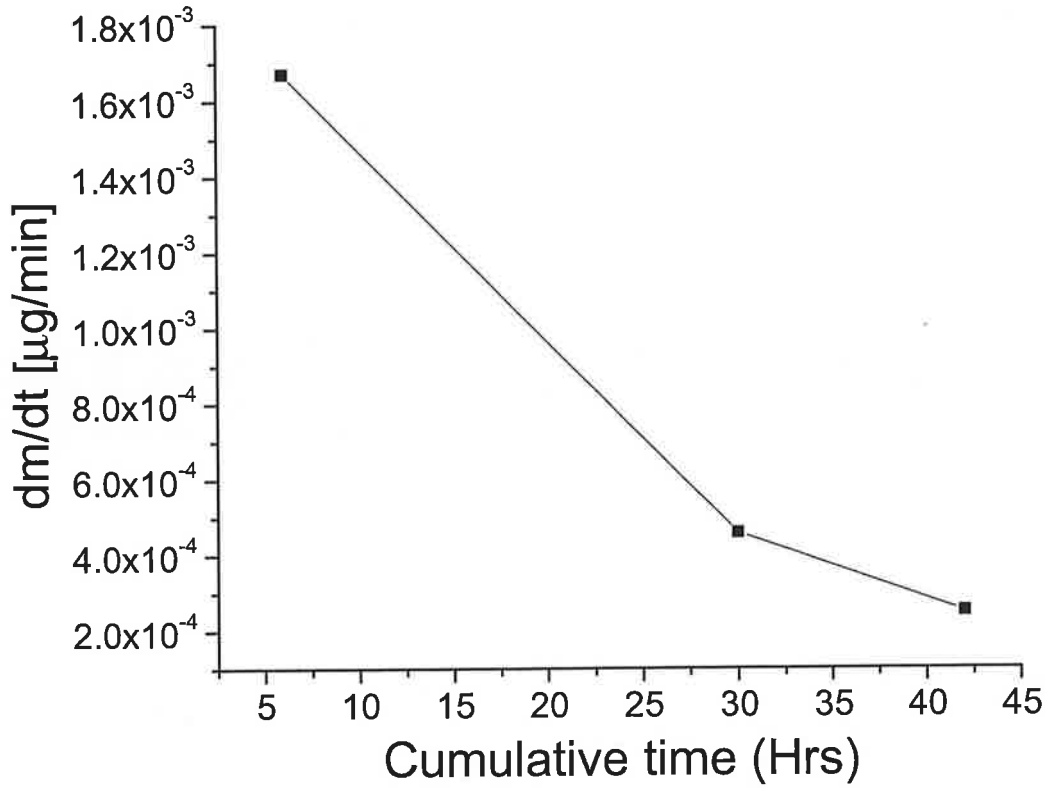

Figure 3.5 Rate of evaporation as a function of cumulative time

3.2 Substrate Preparation

Substrate choice and preparation is a major consideration when working in any nanotechnology research area. This is particularly true when epitaxial growth, leading to well aligned ZnO nanorods is desired. Substrates have to be cleaned before any deposition and, when using the VLS technique, further preparation is required in terms of depositing Au thin films to control the position and density of ZnO nanorods. ZnO nanorods in our experiments are grown on various Au patterned (using an Au thin film or Au nanoparticles as a catalyst) substrates (Si, SiO_2, Al_2O_3, and ZnO) and zinc aluminate domains are grown on unpatterned *c*-sapphire.

3.2.1 Cleaning

Cleaning of substrates and other experimental equipment is very important in our experiments. Small amounts of impurities can effect the growth very dramatically. Before starting any deposition run the substrates have to be properly cleaned using isopropanol or acetone in an ultrasonic bath. The quartz tube in which the deposition takes place is cleaned at less frequent, though regular, intervals (3 months) and one tube is used for each experiment (i.e. one for ZnO nanorods on sapphire, another for zinc aluminate etc.) and each worker in the lab has his/her own set of tubes which are not "swapped".

- Substrate cleaning and preparation before ZnO and $ZnAl_2O_4$ growth

Firstly the substrates on which the nanostructures will be deposited have to be prepared. Since the ZnO structures are of nanometer dimensions, any impurities on a dirty substrate can possibly cause a significant effect on the properties of the grown zinc oxide nanostructures. Because we do not work in clean-room conditions there is likely to be a substantial amount of particles on the substrate. While these are almost impossible to completely eliminate, good cleaning procedures can reduce the particles count substantially.

Substrates in the form of larger wafers are cut with a diamond tipped scribe into 5 x 5 mm squares. Then, the substrate is placed into a glass beaker which holds a series of cleaning agents. Firstly, the substrate is placed in a clean glass beaker filled with acetone and placed in an ultrasonic bath for 15 minutes, and then is placed in a different clean glass beaker filled with isopropanol alcohol and again placed in an ultrasonic bath for 15 minutes. When each substrate is removed from the isopropanol with tweezers, it is immediately blown dry with N_2 gas.

- Au deposition

Thin Au films are mainly deposited in a standard bell jar thermal evaporator. In order to achieve a good vacuum in the jar deposition chamber, it is very important to thoroughly clean all surfaces that come into contact with the vacuum, which includes the bell jar surfaces, boats for evaporation etc.

After the cleaning procedures an Au thin film was deposited on a substrate for samples on which VLS growth was intended. Upon annealing, these Au thin films will self aggregate into high density Au nanoclusters (Figure 3.6). The diameters and the density of these clusters are determined by the thickness of the thin film and the growth temperature. Thus it is possible to control the nanorods area density by modifying the thin film thickness. The Au thin film layer was controlled by the quartz thickness monitor.

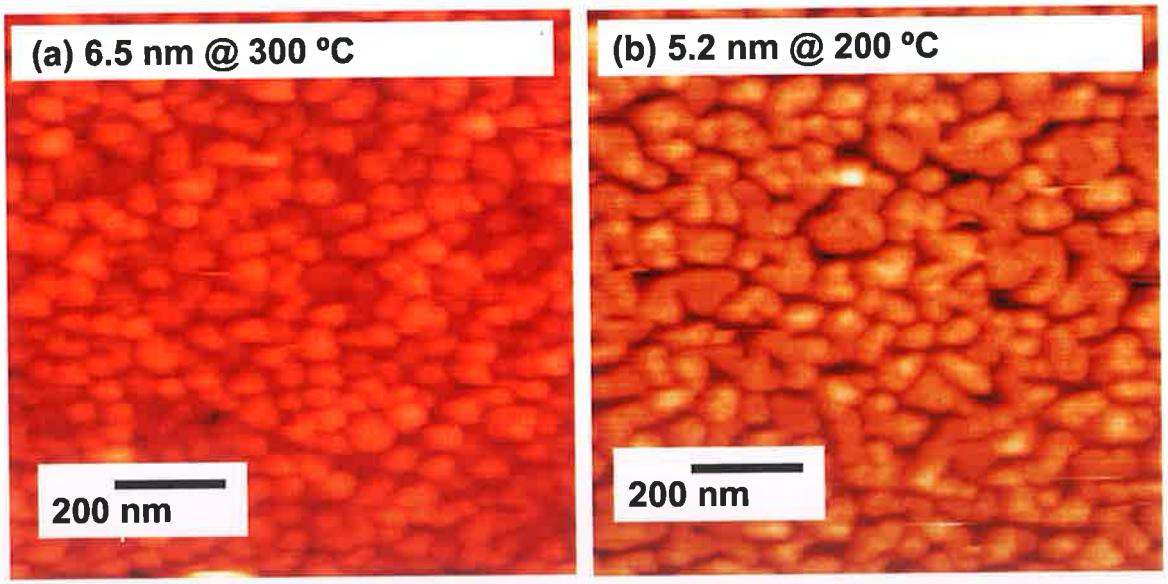

Figure 3.6 AFM images of 6.5 nm of Au film deposited on the silicon substrates and annealing at 300 °C (a), and 5.2 nm of Au film deposited on the silicon substrates and annealing at 200 °C (b).

We have also examined other, more controllable ways of depositing Au nano-particles (such as nano-sphere lithography and colloidal Au particles, applied by both spin coating and immersion).

3.3 Equipment for ZnO and $ZnAl_2O_4$ Characterization

During my PhD work, samples were characterized by a wide variety of techniques and instruments. In the table below (Table.3.1) the main characterisation equipment used are listed. Due to the wide variety of experimental characterisation equipment used, I will not describe each one on detail in terms of principles of operation, but rather give the experimental details as appropriate to the data in this thesis. A limited number of Laue pattern, TEM and Raman measurements were made by colleagues and are reported in the section on $ZnAl_2O_4$ growth. The experimental details will be given in a footnote in the appropriate sections.

Nr	Name of equipment	Description
1	**PL** – **P**hotoluminescence [5]	Optical properties
2	**CL** – **C**athodoluminescence [5 - 6]	Optical properties
3	**SEM** – **S**canning **E**lectron **M**icroscope [7]	Morphology characterization in nanoscale
4	**FESEM** – **F**ield **E**mission **S**canning **E**lectron **M**icroscope [7]	Morphology characterization in nanoscale
5	**TEM** – **T**ransmission **E**lectron **M**icroscop [8]	Morphology & Phase characterization in nanoscale
6	**AFM** – **A**tomic **F**orce **M**icroscop [9]	Topography analysis
7	**XRD** - **X**-**R**ay **D**iffraction [10]	Crystal properties & Phase characterization
8	**EDX** – **E**nergy **D**ispersive **X**-Ray Analysis [11]	Compositional analysis of materials

Table 3.1 Table of techniques and instruments I have been used during my Ph.D. project. References to textbooks, monographs or review articles describing the technique are given in brackets.

***-PL** – (Location - Dublin City University, Dublin, Ireland)*

Photoluminescence spectroscopy is a contactless, non-destructive method of studying the bandedge optical properties and thus the electronic properties of semiconductor materials. Laser light with a photon energy greater than the bandgap is directed onto a sample, where it is absorbed to create excited electron-hole pairs, which in ZnO form very stable Coulombically bound excitons (binding energy ~ 60 meV). These excitons may remain untrapped (free excitons) or become trapped at impurities in the material (bound excitons). The recombination of the electron hole pair generates photons with energies less than but close to the bandgap energy (~ 3.375 eV in ZnO at low temperatures, ~ 367 nm) which constitutes the photoluminescence signal from the sample.

PL is the one of the most important standard characterization tools for ZnO nanostructures measured both at room and cryogenic temperatures. The PL spectra from samples with a wide variety of growth conditions, substrates etc, show strong bandedge and varying degrees of green band intensity, which enable important information to be gleaned about the material. Figure 3.7 shows PL data for ZnO nanostructures grown on Si (100) substrate at room temperature. At room temperature we observed bandedge luminescence (at ~ 379 nm) and the classic ''structured'' green band emission (at ~ 500 nm), which is attributed by various authors to various causes, most commonly native defects such as oxygen vacancies or Cu-related defects [12, 13]. Room temperature PL reveals little about the optical quality / exciton structure of the material. The low temperature PL (< 50 K) reveals much more detail on the excitonic structure of the material, important for potential device applications using the exciton recombination in zinc oxide. There are fewer reports of low temperature exciton PL (compared to room temperature PL) , but nearly all indicate that very good optical quality is seen. Our data for certain growth conditions on sapphire (chapter 5: PL Study of the Zinc Oxide Nanorods/Nanowalls System) indicate that exceptionally high quality material may be obtained with low temperature PL spectra as good as that from as the best bulk material.

The PL data were taken using the 325 nm line of a continuous wave HeCd laser (output ~ 22 mW unfocussed on the sample) as the excitation source. The emission from the sample

was analyzed using a one meter grating spectrometer (SPEX 1704) and detected with a photomultiplier tube (Hamamatsu model R3310-02) in photon counting mode. Controllable temperatures down to 5 K were achieved using a closed cycle cryostat (Janis SHI-950-5). The typical resolution of the PL data taken in the near bandedge region was slightly less than 100 μeV and the absolute energy positions referenced to a calibration source were accurate to ~ 200 μeV. All these data were corrected for the effects of the refractive index of air as appropriate (1.0003).

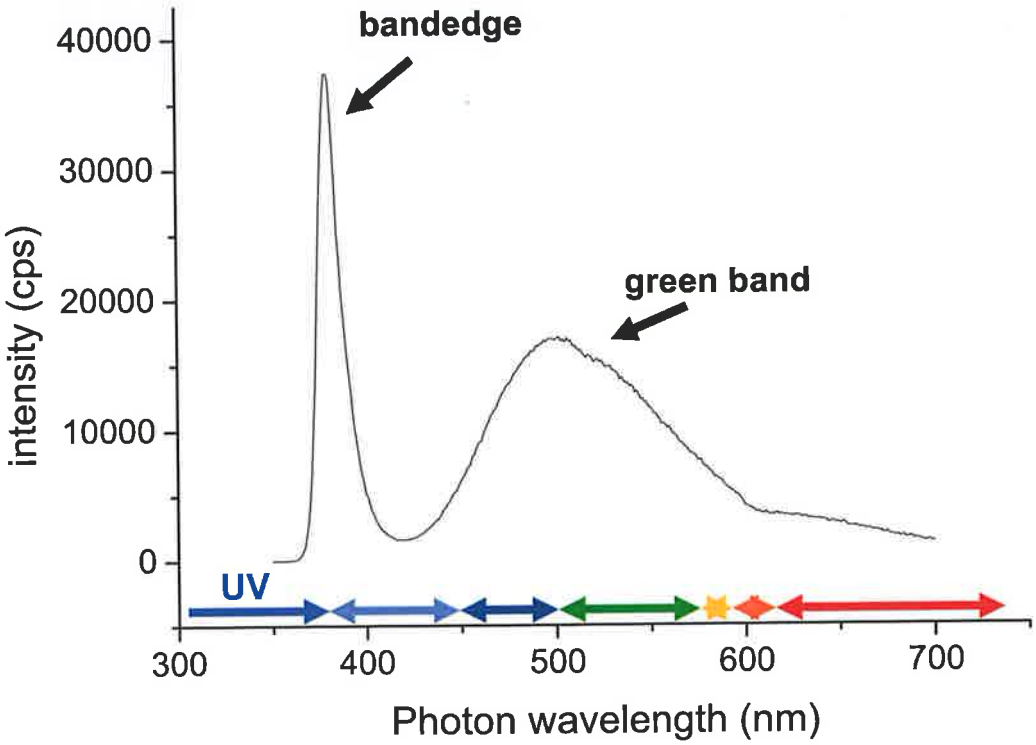

Figure 3.7 Room temperature photoluminescence spectrum of ZnO nanostructures grown on Si (100) substrate. Each colour on arrows above the x-axis of the spectrum corresponds to specific wavelength and energy range to make up visible light.

*-**CL**-SEM – (Location - Dublin City University, Dublin, Ireland)*

Cathodoluminescence is the emission of light from a sample when bombarded with an electron beam in a specially equipped SEM. In many ways the process is identical to PL except that an electron beam is used as the excitation source rather than a laser beam, and the interband excitation occurs by impact ionisation. However the small electron beam

width enables a very fine degree of spatial resolution in the CL-SEM system, i.e. only a much localised region (< 100 nm diameter) is excited, compared to a ~ 2 mm diameter laser for PL. In addition the depth of the electron beam penetration depends on the electron beam energy and on the materials, typically of 1 μm in semiconductor for a 10 keV electron beam. This non-destructive method is a very important characterization tool for ZnO nanostructures samples due to the spatial and depth resolution capabilities it provides which are important for nanostructured materials. Figure 3.8 shows CL spectrum for ZnO nanostructures grown on *a*-plane sapphire at room temperature. CL-SEM measurements were carried out on a Gatan Instruments CL coupled to the LEO Steroscan SEM described below.

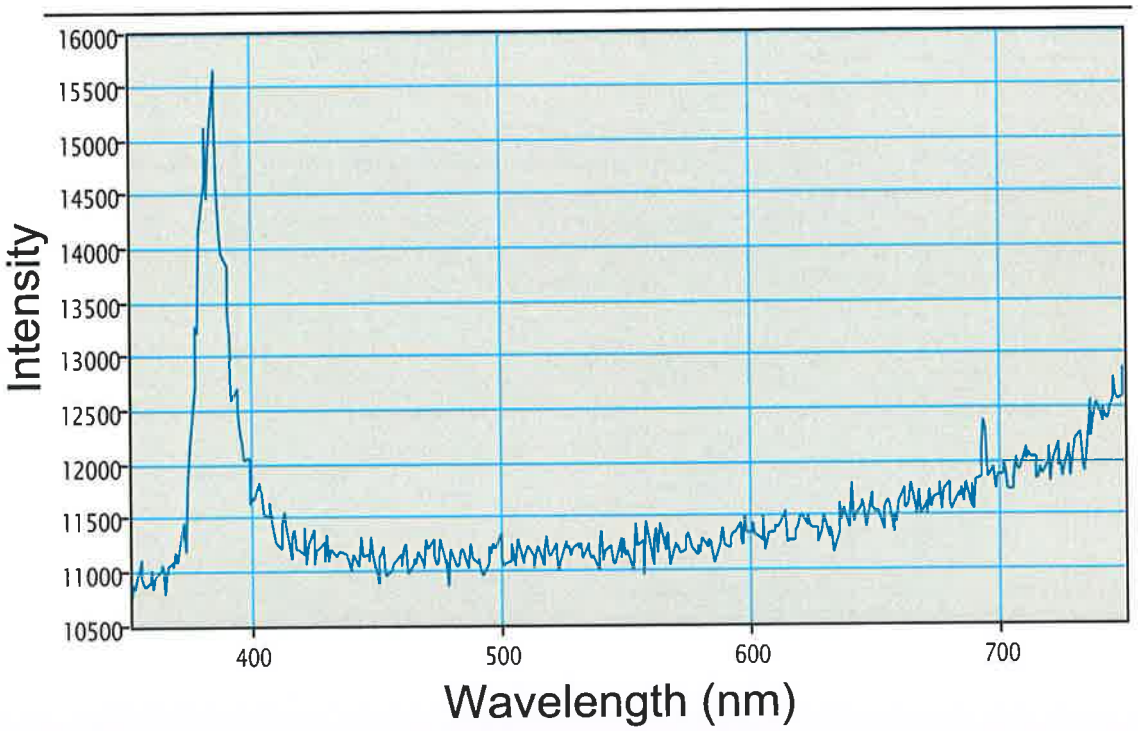

Figure 3.8 CL spectrum for ZnO nanostructures grown on a-plane sapphire at room temperature

-SEM & FESEM & EDX *– (Locations - Dublin City University, Dublin, Ireland & Trinity College Dublin, respectively)*

SEM instruments use a narrow (~ 10 nm) beam of high energy electrons (accelerated though potential differences of 1000's of volts) which is scanned in a raster fashion over

the sample. Various detectors, the most common being a Secondary Electron detector, produce a voltage corresponding to the response of the sample to the beam at each point in the scan. This produces an image of the sample which is deceptively like an optical photograph, though there can be very great differences. SEM images constitute the workhorse measurement for nanostructure morphology studies in order to study nanostructure growth, both for ZnO and $ZnAl_2O_4$ samples. The systems used were a LEO Stereoscan 440 system in DCU and a Hitachi S-4300 Field Emission system in TCD. The field emission system produces better images as the electron beam is produced by a cold cathode field emission process rather than thermionic emission, leading to higher simultaneously higher brightness and better resolution images. For FESEM work the samples were sputter coated with a 10 nm Au thin film post nanostructure growth, in order to eliminate charging effects which occur on insulating substrates such as sapphire.

EDX is effectively one mode of operation of a SEM, where the X-Ray spectrum of the sample (which results from electron bombardment by the primary SEM beam) is measured. A detector collects the X-rays and produces current pulses proportional to the X-ray photon energy; a pulse processor acts as a matched filter to convert the signal to analog voltage pulses. The information is used to create an X-ray spectrum, a plot of counts detected versus X-ray energy. The spectrum can be acquired in probe mode (stationary beam) or in scanning mode (moving beam). The X-ray spectrum for different elements is unique and thus this measurement was used to perform compositional analysis of samples at high spatial resolution, yielding percentage compositional information on both ZnO nanostructures samples and $ZnAl_2O_4$ samples. The instrument used is a Princeton Gamma-Tech (PGT) EDX spectrometer coupled to the LEO Stereoscan SEM.

-TEM – (Location – Glebe Laboratories, Co. Tipperary, Dr. Simon Newcomb)

TEM instruments use a very narrow beam (~ 1 nm) of very high energy electrons (accelerated though potential differences of 100,000's of volts) which is again scanned in a raster fashion over the sample. In this case the electron beam transmission through the sample is measured (rather than various sample responses to bombardment as in a SEM). This requires that the sample be thinned to electron transparency (few 100 nm). This

specialist task was undertaken by Dr. Simon Newcomb of Glebe Laboratories using mechanical thinning and ion beam techniques. Depending on the focus conditions used the TEM can yield both direct microscopic images of the material structures at very high magnification, and also can operate in Fourier transform mode, where it effectively forms a diffraction pattern of the lattice structure in the small region under illumination thus allowing the reciprocal space lattice to be measured and the material phase to be determined. TEM measurements have been made by Dr. Newcomb on a range of samples to identify the $ZnAl_2O_4$ phase and elucidate the details of the associated domain structures. The TEM used was a JEOL2000FX operating at 200 kV. Sections for microstructural evaluation were made using standard focused ion beam (FIB) thinning [14].

***-AFM** – (Location - Dublin City University, Dublin, Ireland)*

An atomic force microscope works by measuring how the force between the sample and a tiny "tip" on a cantilever changes as the microscope is moved over the surface of the sample. In most cases the image formed is an accurate reflection of the surface topography. However it is important to note that AFM contrast is also influenced by other factors including the surface chemistry. The small size of the AFM tip (tip radius of curvature ~ 50 nm) means that a relatively small portion of the tip interacts with the surface (via van der Waals or capillarity effects). This means that if the AFM mounting is vibration free the AFM can record images with extremely high spatial resolutions, sometimes approaching or achieving atomic resolution. Measurements of surface topography were made for a range of the $ZnAl_2O_4$ domains on various samples. The resolution in these cases was in the region of 10 nm. The instrument used was a Nanoscope IIIa, Digital Instruments operated in contact mode as the ceramic aluminate surface is mechanically robust. The AFM was mounted on a vibration-isolated table.

***-XRD** – (Location - Dublin City University, Dublin, Ireland)*

XRD is an efficient analytical technique used to identify and characterize the phase of crystalline materials. It relies on the reflection of incident x-rays at various angles according to Bragg's Law, which enables identification of the lattice spacing corresponding to reflections at a particular angle, once the x-ray wavelength is known. This is turn

generally enables unambiguous identification of the phase of the material under study as the lattice plane spacing is unique to particular materials. The XRD was used as a workhorse instrument in studying both the composition and morphology of both ZnO nanorods and $ZnAl_2O_4$ domains. The instrument used was a Bruker AXS D8 advance texture diffractometer using Cu K_α radiation ($\lambda = 0.15418$ nm), which enabled the material phase and epitaxial relationships between deposited materials and the substrate to be studied.

3.4 References

[1] J. J. Wu, S. C. Liu, *Advanced Mater*ials **14** (2002) 215

[2] Y. C. Kong, D. P. Yu, B. Zhang, W. Fang, S. Q. Feng, *Applied Physics Letters* **78** (2001) 407

[3] R. O'Haire, A. Meaney, E. McGlynn, M. O. Henry, J.-R. Duclere, J.-P. Mosnier, *Superlattices and Microstructures* **39** (2006) 153

[4] Z. W. Pan, S. M. Mahurin, S. Dai, and D. H. Lowndes, *Nano Letters* **5** (2005) 723

[5] L. Ozawa, 'Cathodoluminescence and Photoluminescence: Theories and Practical Applications (Phosphor Science and Engineering)', 2007

[6] L. Ozawa, 'Cathodoluminescence: Theory and Applications', 1991

[7] J. Goldstain, D. E. Newbury, D. C. Joy, Ch. E. Lyman, P. Echlin, E. Lifshin, L. C. Sawyer, J. R. Michael, 'Scanning Electron Microscopy and X-ray Microanalysis', 2003

[8] S. L. Flegier, J. W. Heckman, K. L. Klomparens, 'Scanning and Transmission Electron Microscopy: An Introduction', 1995

[9] M. T. Bray, S. H. Cohen, M. L. Lightbody, 'Atomic Force Microscopy / Scanning Tunneling Microscopy', 1995

[10] A. Guinier, 'X-Ray Diffraction: In Crystals, Imperfect Crystals, and Amorphous Bodies', 1994

[11] J. C. Russ, 'Fundamentals of Energy Dispersive X-Ray Analysis (Monographs in Materials', 1984

[12] R. Dingle, *Physical Review Letters* **23** (1969) 579

[13] K. Vanheusden, W. L. Warren, C. H. Seager, D. R. Tallant, J. A. Voight, B. E. Gnade, *Journal of Applied Physics* **79** (1996) 7983

[14] S. B. Newcomb, in: S. McVitie, D. McComb (Eds.), Inst. Phys. Conf. Ser., No. 179, Inst. Phys., Bristol, UK, 2004, p.357

4 Well Aligned Zinc Oxide (ZnO) Nanorods and Nanowalls

In this chapter a study of growth of ZnO nanorods is presented and the issues affecting growth control are discussed. For future applications of one-dimensional ZnO nanostructures it is very important to understand and to be able control their alignment, shape, size (diameter and length), and their distribution. Controlling the morphology is a key issue for ZnO-based nano-devices. ZnO nanostructures with different morphologies finds different applications: rods (UV photonic devices), needle (field emission plasma displays), wire (sensors, interconnects for nano circuits), belts (piezoelectric nano-mechanical devices), films (solar cells). The detailed morphology is very sensitive to growth conditions. To control the size and morphology of the zinc oxide nanostructures via VPT method we have to properly focus on various parameters like: growth temperature, duration, growth steps, and catalyst conditions. Our results show that a variety of ZnO nanostructure morphologies (rods, wires, mixed rods/walls) can be fabricated by controlling the growth parameters. The degree of sensitivity appears to depend on the type and orientation of substrate used, e.g. many reports of well aligned zinc oxide nanorods are on a-plane sapphire.

In the following chapter I will describe the results we have obtained concerning growth of materials by the previously described methods. We used FESEM and XRD to give structural results and PL to give optical characterization of the material. Many potential applications of nanorods are as photonic devices, and thus the optical properties of these systems are extremely important. In the first stages of the project work, shortly after the commissioning of the growth system detailed in the previous chapter, we grew a wide range of samples on a variety of structures with various process parameters simply to develop our own expertise and to compare with the published literature to validate the growth apparatus. Subsequently we have concentrated on specific aspects of nanostructure growth and control of growth of well separated ZnO nanorods and ZnO nanorods/nanowalls.

In the literature we can find various names to describe 1D stretched out structures, such as nanowires, nanorods, nanoribbon, and nanobelt and the choice of these names is not always consistent from one report to another [1-4]. In order to be consistent with the majority of the literature in this thesis we have named the nanostructures we have concentrated on as either 'well separated nanorods' or 'rods/walls ZnO nanostructures'. Other morphologies which we have observed we will label appropriately in the text with an explanation. The nanorod description is used to indicate structures of ~ 100 nm diameter and lengths of ~ 1 μm, and well aligned means with their long axes growing perpendicularly to the substrate surface. The 'rods/walls ZnO nanostructures' are so called because of the interconnecting walls at the bottom of well aligned zinc oxide nanorods in this mixed morphology.

4.1 Initial Experiments: Type and Orientation of Substrate and Overview of Effects on Morphology

It is readily seen in the literature that the morphology and degree of alignment of well separated ZnO nanorods depends, among other factors, on the type of substrate [1]. Nanowire growth on *a*-plane sapphire is generally well aligned along the vertical direction (due to the uniaxial locked epitaxy condition reported by Fons [5]. In contrast VPT growth on a Si/SiO_2 substrate is generally not well aligned. One of our first series of experiments with the VPT growth apparatus was to investigate the effect of different substrates and to reproduce the general type of results found in the published literature.

We show some examples below of the nanostructures grown on substrates other than *a*-sapphire. When the growth was completed to compare with published data, in most cases our structures matched the data in the literature well [6]. What is immediately evident is that ZnO readily forms a variety of nanostructures on different substrates, and that the physical and chemical processes influencing the growth and morphology are quite complicated. The FESEM images (Figures 4.1 - 4.5) with various ZnO nanostructures grown on various substrates (Si, ZnO, SiO_2, *c*-, *a*-sapphire) are presented below (Table 4.1).

We have used source and substrate temperatures in the range 950 - 1000 °C following the general ranges reported in the early literature as a guide.

Substrate	Furnace Temp.	Substrate Temp.	Au thickness	Comments/Description	Figure
Si / SiO_2	950 ° C	890 ° C	52 Å, pre-annealed @ 200 ° C for 3.5 mins.	unaligned nanowires	4.1
O-term. ZnO	1000 ° C	975 ° C	NO	micro/nanostructures	4.2
SiO_2 (Si /in O_2	1000 ° C	975 ° C	NO	micro/nanostructures	4.3
c-Al_2O_3	1125 ° C	1075 ° C	20 Å, pre-annealed @ 800 ° C for 3 mins.	nanorods	4.4
a-Al_2O_3	950 ° C	925 ° C	20 Å	we see well aligned nanorods	4.5

Table 4.1 shows experimental conditions and comments for samples grown on various substrates

Si substrate (950 °C furnace temperature, 52 Å Au thin film pre-annealed @ 200 °C for 3.5 minutes)

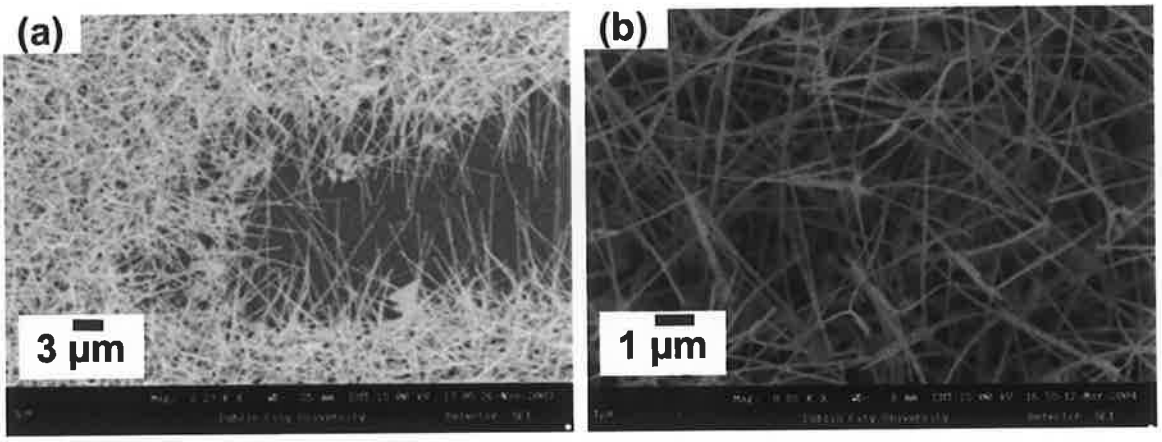

Figure 4.1 SEM images of ZnO nanowires on the silicon substrate, low magnification (a), high magnification (b)

ZnO substrate (O-terminated ZnO, 1000 °C furnace temperature, no Au thin film)

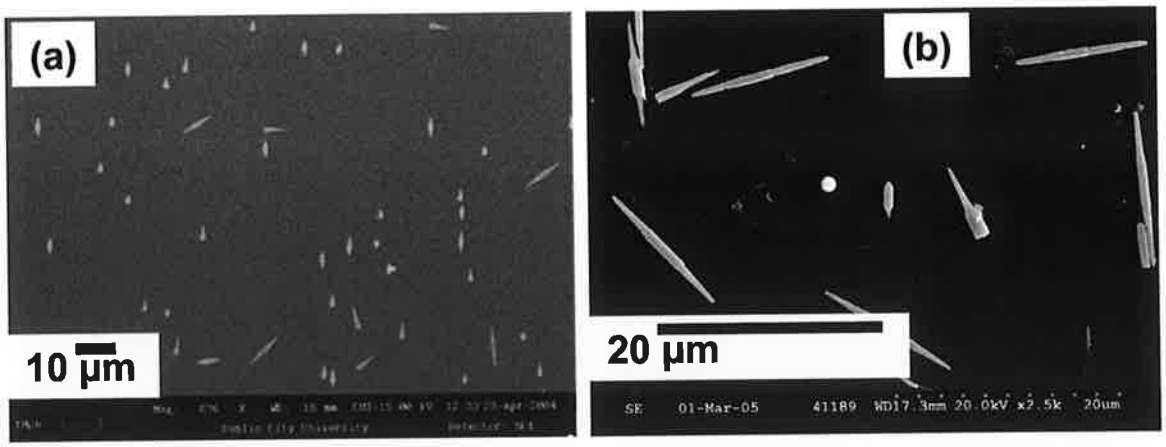

Figure 4.2 SEM & FESEM image of ZnO micro/nanostructures, low magnification (a), high magnification (b)

SiO_2 substrate (Si wafer annealed in O_2 gas at 1100 °C before growth, 1000 °C furnace temperature, no Au catalyst)

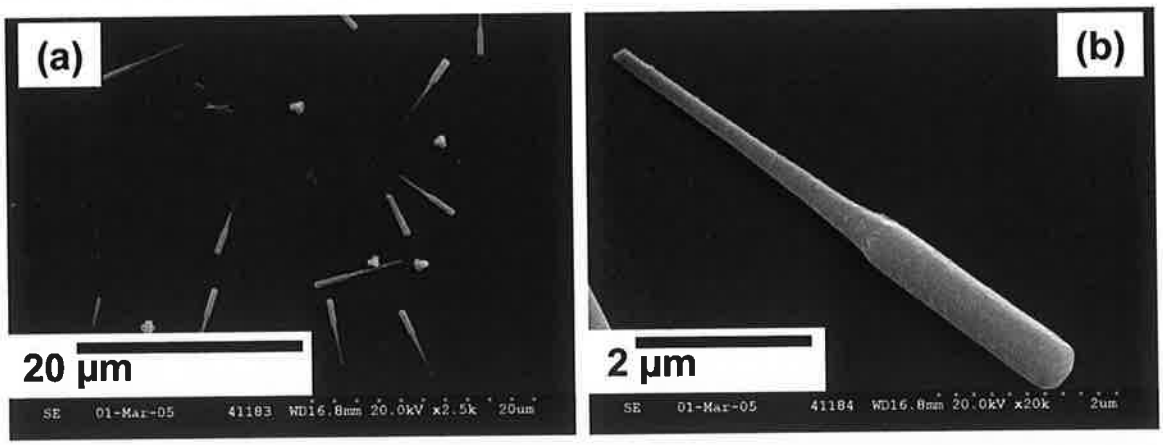

Figure 4.3 FESEM images of ZnO micro/nanostructures, low magnification (a), high magnification (b); Growth on Au-coated SiO_2 does not appear to lead to nanorod structures in the temperature range we have examined, though evidence is seen of catalyst-free nanorod growth in the Au-free regions as shown above.

c-plane sapphire substrate (1075 °C and 1125 °C furnace temperatures, 20 Å Au thin film pre-annealed @ 800 °C for 3 minutes)

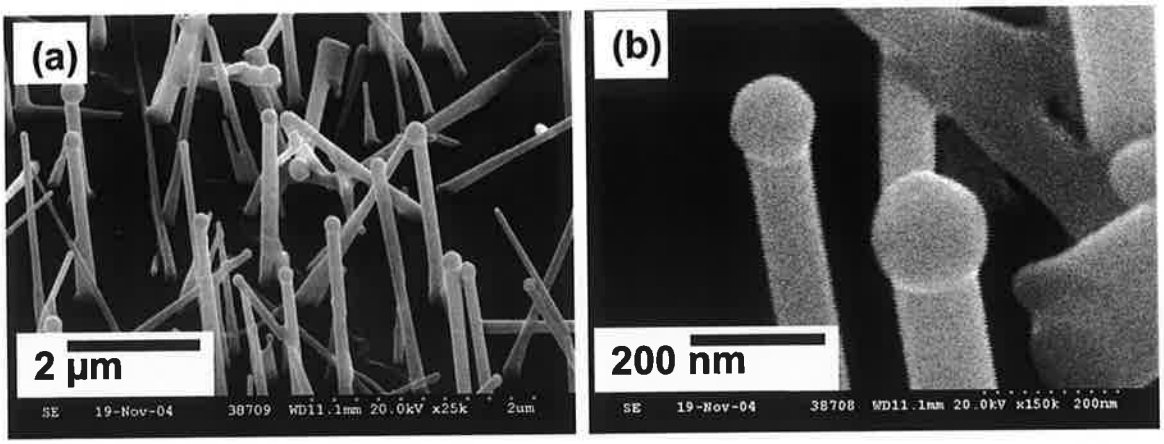

Figure 4.4 FESEM images of ZnO nanorods, low magnification (a), high magnification (b)

a-plane sapphire substrate (925 °C substrate temperature and 950 °C furnace temperatures, 20 Å Au thin film)

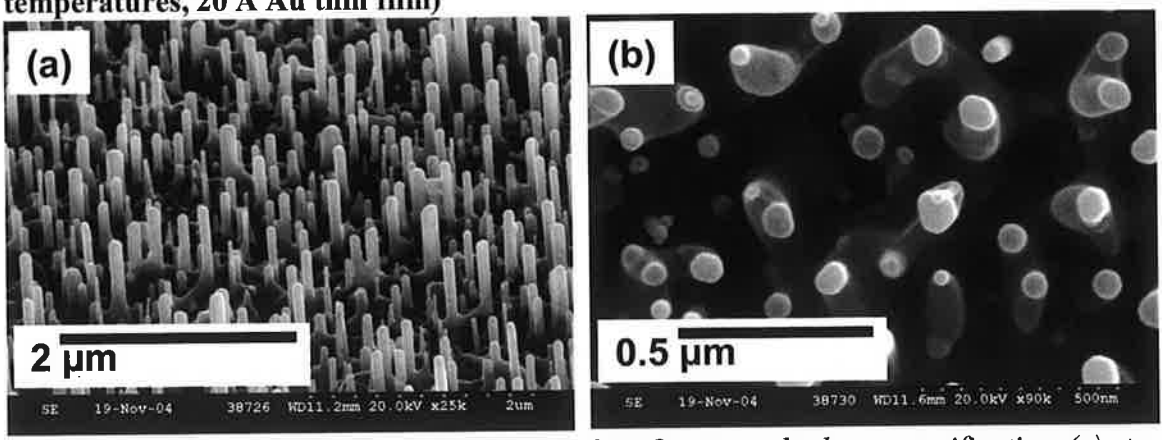

Figure 4.5 FESEM images of well separated ZnO nanorods, low magnification (a), top view, high magnification (b)

In addition to the wide variety of morphologies seen in Figures 4.1 - 4.3 above, it is also clear that the growth mechanisms are in many cases very different to the ideal VLS mechanism described in chapter 2. For example on a thick SiO_2 layer no growth is seen on the Au-covered region, whereas some growth is seen on the uncovered region. For growth on Si with a native oxide, ZnO nanowires (generally distinguished from nanorods by their much higher aspect ratio, i.e. length to diameter ratio) are seen to grow only in the region

where there is Au deposition, but no evidence of genuine VLS growth is seen (i.e. with Au droplets at the nanowire tips), and the growth appears to be mediated by the Au catalyst rather than actual VLS. This is in agreement with more recent work in the literature [7] and indicates that in the case of Si substrates (with native oxides) the Au droplets may serve solely as suitable nucleation points for Zn vapour.

Growth on *c*-sapphire (Figure 4.4) shows that in this case growth is via a genuine VLS mechanism and Au 'cap' can be seen on top of nanorods, which are generally well aligned. In fact our data and data from the literature more generally indicate that ZnO nanorod growth on the common sapphire terminations (*c*-, *a*-, *r*- & *m*-) occurs via genuine VLS in the temperature region around 950 °C. Thus we have concentrated our attention after the initial experiments on growth on *a*-sapphire (Figure 4.5).

4.1.1 Initial Experiments: VLS Growth on a-plane Sapphire

The consensus in the literature seems to point to *a*-sapphire as the most suitable substrate to achieve high quality well aligned ZnO nanostructures via VLS. The good alignment was explained by Fons *et al* [5] as due to the domain epitaxial match between the ZnO *c*-plane and the sapphire *a*-plane. For this reason our next set of experiments focused on VLS growth on *a*-sapphire in order to obtain well aligned ZnO nanorods. In our experiments well aligned ZnO nanorods were grown on *a*-plane sapphire using a ~ 20 Å catalytic Au thin film using the process described in chapter 2. The source and substrate temperatures were 950 °C and 925 °C, respectively. Figure 4.6 shows the FESEM image of the ZnO nanorods that were obtained which showed a high degree of alignment perpendicular to the ZnO substrate. Au clusters can be seen as hemispherical caps on the tips of the nanorods, confirming the VLS mechanism behind the growth.

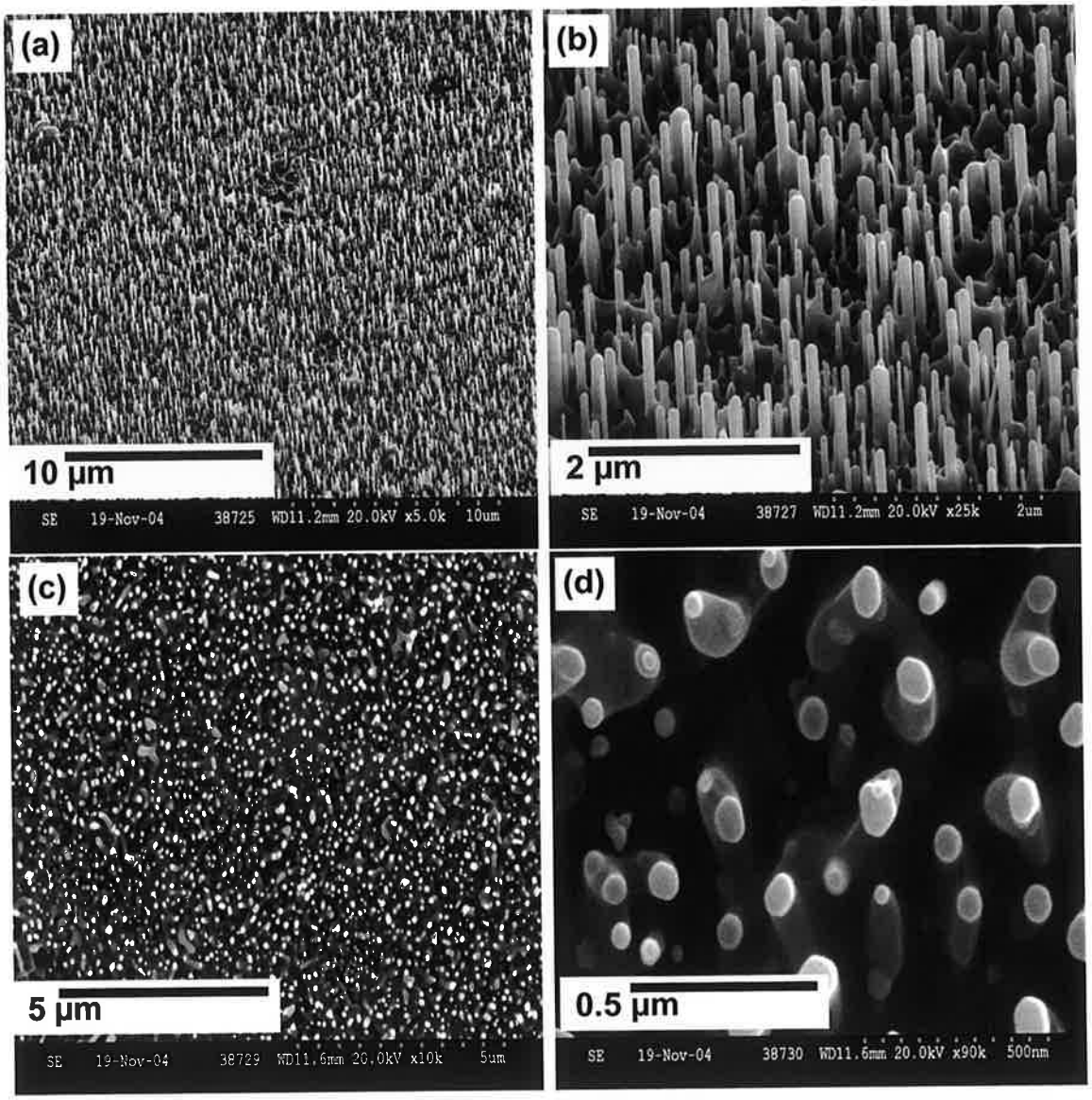

Figure 4.6 FESEM images of well aligned ZnO nanorods, tilted view (a, b), top view (c, d)

The high degree of alignment of the ZnO nanorod *c*-axes perpendicular to the substrate (texture) is shown by XRD data in Figure 4.7(a) below. θ-2θ data show only the ZnO (0002) and (0004) reflections at 34.47 ° and 72.68 °, respectively, in addition to the sapphire (11-20) reflection at 37.78°. These data for ZnO imply that a slight strain exists in the nanorods. The tabulated value for the (0002) reflection is 34.42^0 ([8] (a = 0.324982 nm, c = 0.520661 nm, c/a = 1.602)). Our data indicate that a slight tensile in-plane strain exists in the nanorods (leading to a reduction in the out-of-plane *c*-lattice parameter and an increase in

the 2θ reflection value, from Bragg's Law). This is consistent with the fact that although an almost perfect domain epitaxial match is achieved between (4 times) the ZnO *a*-lattice parameter and the sapphire c-lattice parameter for one in-plane direction, as discussed by Fons [5] the match between the two lattices along the orthogonal in-plane direction (the [10-10] direction) is not as good (4.12 Å for sapphire and 2.81 Å for ZnO, leading to a tensile in-plane strain at the nanorod-substrate interface). This is discussed further in chapter 5.

The degree of alignment can be quantified by the x-ray rocking curve (ω-scan) shown in Figure 4.7(b). The width of this curve is related to the mosaic spread of the nanorod long axes about the normal to the surface and is ~ 0.23 ° in the sample shown in Figure 4.7(b). This width is typical for the majority of samples grown on *a*-plane sapphire in our optimized conditions. The instrumental broadening contribution to this width is ~ 0.1 ° (based on data from supplier) indicating the mosaic spread of the nanostructures is ~ $\sqrt{(0.23)^2-(0.1)^2}=0.2^0$.

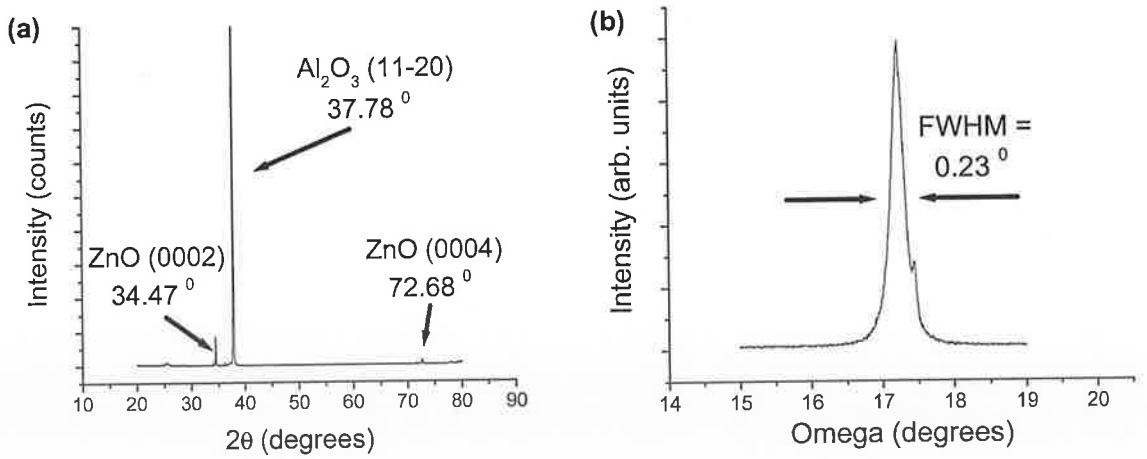

Figure 4.7 shows θ-2θ x-ray diffraction (XRD) data for well aligned ZnO nanorods grown on a-plane sapphire, with the ZnO (0002) and (0004) peaks clearly seen at 34.47 and 72.68 deg, respectively (a); Rocking curve of well aligned ZnO nanorods sample

Well aligned ZnO nanorods on *a*-plane sapphire also show extremely high optical quality at room temperature. Photoluminescence spectrum (Figure 4.8) taken at room temperatures shows very sharp peak at a wavelength $\lambda = 369$ nm. This peak corresponds to the bandedge free exciton and LO phonon replica signals at room temperature [9]. There is no emission in the visible region of the spectrum associated with optically active defects and specifically no sign of the green band, a well known emission from ZnO with a peak at ~ 520 nm, often attributed to oxygen vacancies [10].

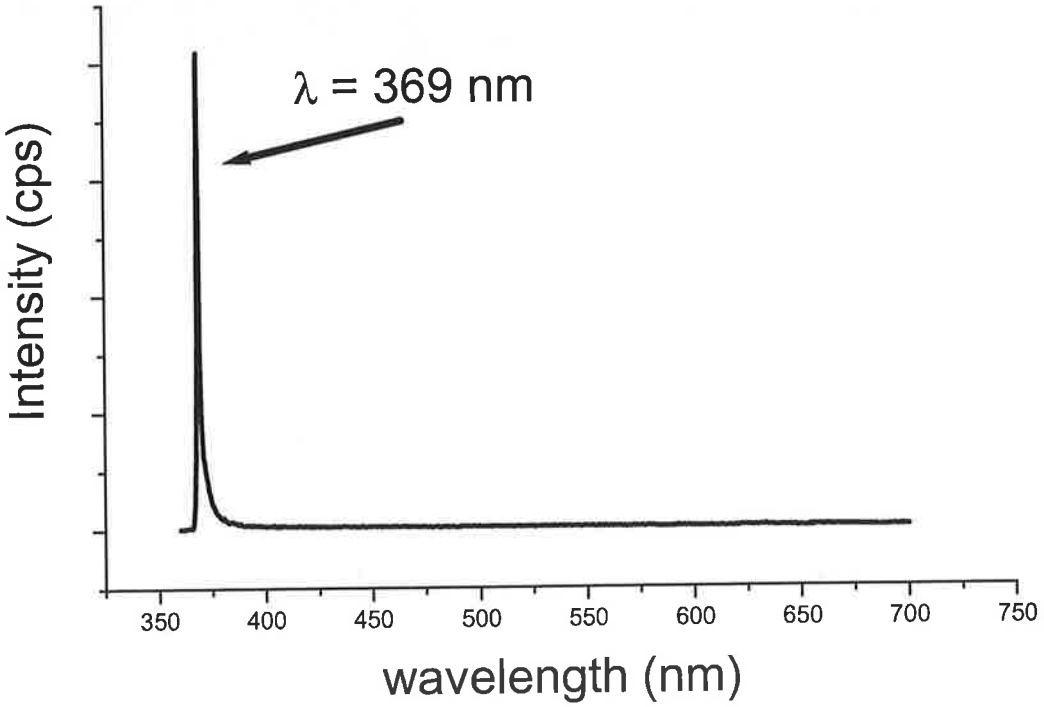

Figure 4.8 Photoluminescence spectrum of well aligned ZnO nanorods taken at room temperatures shows very sharp peak at a wavelength $\lambda = 369$ nm.

These data indicated that we were able to reproduce the ZnO well aligned nanorod morphologies on *a*-sapphire reported in the literature, and that the crystal quality, as judged from XRD and room temperature PL were quite comparable with the data reported by other workers.

4.2 VLS Growth on *a*-plane Sapphire: Morphology Control

Following initial experiments to duplicate literature results for growth on *a*-plane sapphire, and the confirmation of the VLS mechanism for this process we then extended our study of growth on this substrate to investigate the effects of varying different parameters such as the thickness of the catalytic Au film, source temperature, substrate temperature, and time of deposition. The data below show that these parameters have a significant influence on the ZnO morphology. Consequently by varying those parameters we can control the morphology of the ZnO nanostructures.

4.2.1 Au Catalyst

Based on our data and reports in the literature the Au film thickness and its consequent morphology are very important factors in determining the ZnO nanorod growth morphology, though few systematic studies have appeared in the literature.

From the graph below (Figure 4.9) we can see that the melting point of Au particles depends upon their size, for example the melting point (MP) for 50 Å diameter spheres is ~ 830 °C and for bulk Au the MP is 1064 °C. The change in melting point with size is due to surface energy (surface tension) effects which alter the Gibb's free energy of the system in a significant manner for nano-sized objects [11]. Generally lower temperatures are required to melt smaller particles due to these effects. The following equations are reported to describe the variation of melting temperature with size for films (D = thickness) and spherical particles (D = diameter), and the variations are shown in Figure 4.10 [12].

$$T_m^F = T_\infty - \frac{\alpha}{3D} \Rightarrow \Delta T = \frac{\alpha}{3D} \qquad (4.1)$$

Where α is a parameter proportional to the difference in surface tension between the liquid and solid phases, T_m^F is the melting temperature for thin films and T_∞ the melting temperature for bulk Au (1064 °C). A similar analysis for spherical particles shows that the variation in melting temperature is given by

$$T_m^S = T_\infty - \frac{\alpha}{D} \Rightarrow \Delta T = \frac{\alpha}{D} \qquad (4.2)$$

where α has the same numerical value as in Equation (4.1), determined only by the difference in surface tension between the liquid and solid phases for Au and T_m^S is the melting temperature for spherical particles. The difference in morphology between films and spherical particles is accounted for by the factor of 3 in equation (4.1).

We can use the published values for the variation in melting temperature of spherical Au particles [11] to determine α using Equation (4.2) and then use this value of α in equation (4.1) to ascertain the variation in melting temperature of thin Au thin films. The values for melting temperature for spherical particles were taken from the graph in Figure 4.9 and the melting temperature for thin films was calculated from Equation (4.1). All data are summarized in the Tables 4.2 and 4.3 below.

Spherical Particles (Å)	T_m^S **(°C), from Figure 4.9**	**α (K.Å), from Equation (4.2)**
20	327	14740
25	427	15925
50	827	11850
75	927	10275
100	947	11700
		Average $\alpha = 13000 \pm 2500$

Table 4.2 shows data taken to determine the value of α

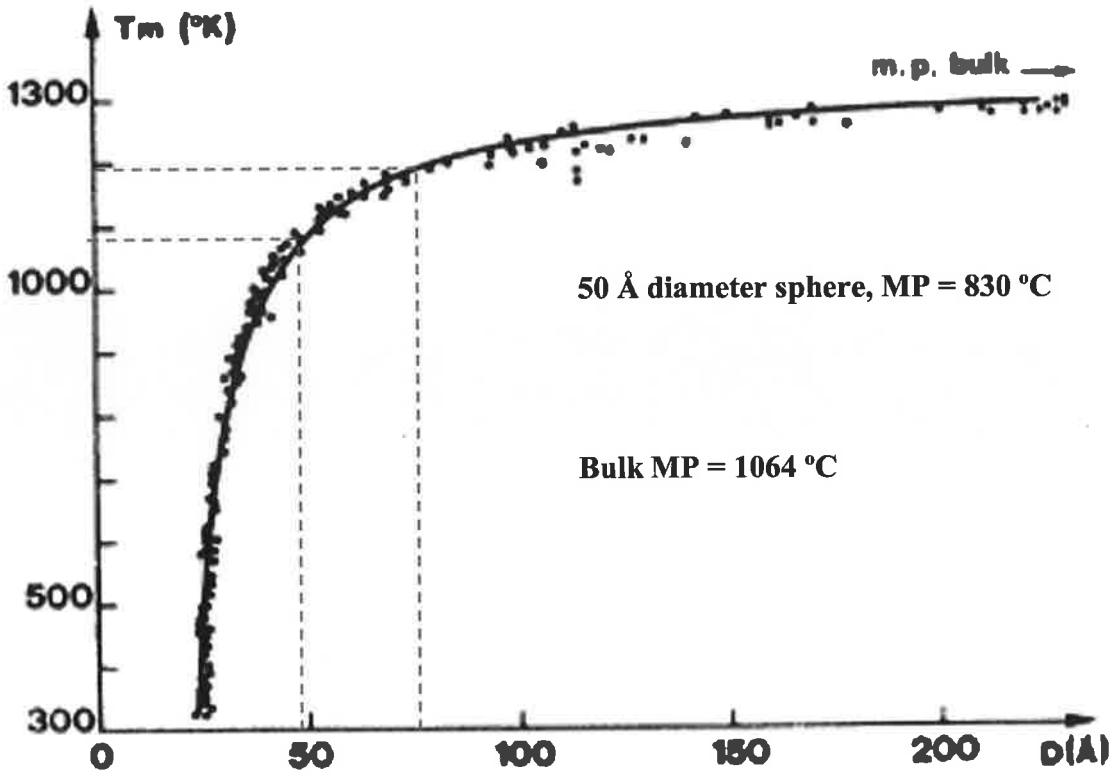

Figure 4.9 Experimental values of the melting-point temperature of Au particles (taken from [11]).

Film Thickness (Å)	T_m^F (°C) from Equation (4.1) with α = 13000 (~25% error)
20	847 ± 50
25	890 ± 50
50	977 ± 25
75	1006 ± 20
100	1020 ± 15

Table 4.3 shows thin film melting temperature data calculated using the value of a determined from Table 4.2 and used to plot the graph in Figure 4.10

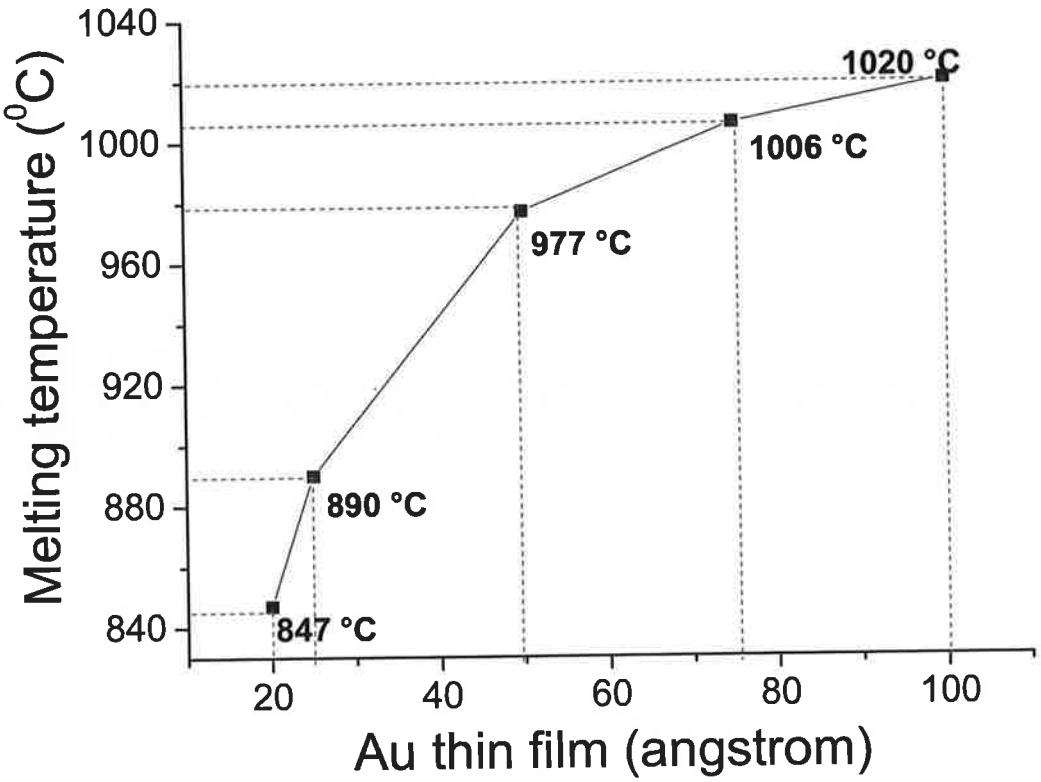

Figure 4.10 Calculate values of the melting-point temperature of Au thin films (using equation (1) above

In our study we grew ZnO nanorods using various methods to prepare catalytic Au clusters (see chapter 3 and Appendix I). However the main method of preparing Au clusters for VLS growth was to use evaporated Au thin films. As discussed previously these bead up due to capillary forces at high temperatures during growth in the furnace to form Au nanoclusters. The nanoclusters then act as the nucleation sites for ZnO nanorods and the diameter and density of the nanorods is determined, to a certain extent at least, by the nanocluster size and density. The thickness of the initially deposited Au film is expected to have an important role in determining the nanocluster morphology. We deposited different thicknesses of Au films on the *a*-plane sapphire and annealed them at 900 °C (in a pure Ar flow of 90 sccm, with no Zn vapour) to observe the development of Au nanoclusters with an emphasis on their size, distribution and density.

This results of this study using a variety of Au film thicknesses (from 5 Å to 100 Å) annealed at 900 °C for 30 minutes is shown in Figure 4.11 (no ZnO growth took place; the Au-coated *a*-sapphire substrates are simply annealed in a 90 sccm Ar flow). It is clear that one can control both the size and density of Au clusters by tuning the Au thickness film. The data indicate that the average nanocluster diameter formed from Au thin film thicknesses ≤ 20 Å are roughly constant at ~ 30 - 40 nm, while the density increases with increasing film thickness in this range as shown in Figure 4.12. For Au thin film thicknesses ≥ 50 Å the density of particles reduces while the particle size increases with increasing film thickness. The maximum density of nanoclusters is seen for a film thickness of 50 Å. These data are summarized in Table 4.4. For the largest diameter particles derived from 75 Å & 100 Å Au films there is clear evidence of faceting in many of the particles. Based on these data it is clear that the thickness of the deposited Au film has a substantial effect on the density and size of the Au nanoclusters formed, however no clear monotonic relationship has emerged. The 50 Å Au film seems to be a critical thickness below which the nanocluster size is roughly constant and the density increases with increasing film thickness, while above this Au film thickness the particle size increases while the density reduces with increasing film thickness.

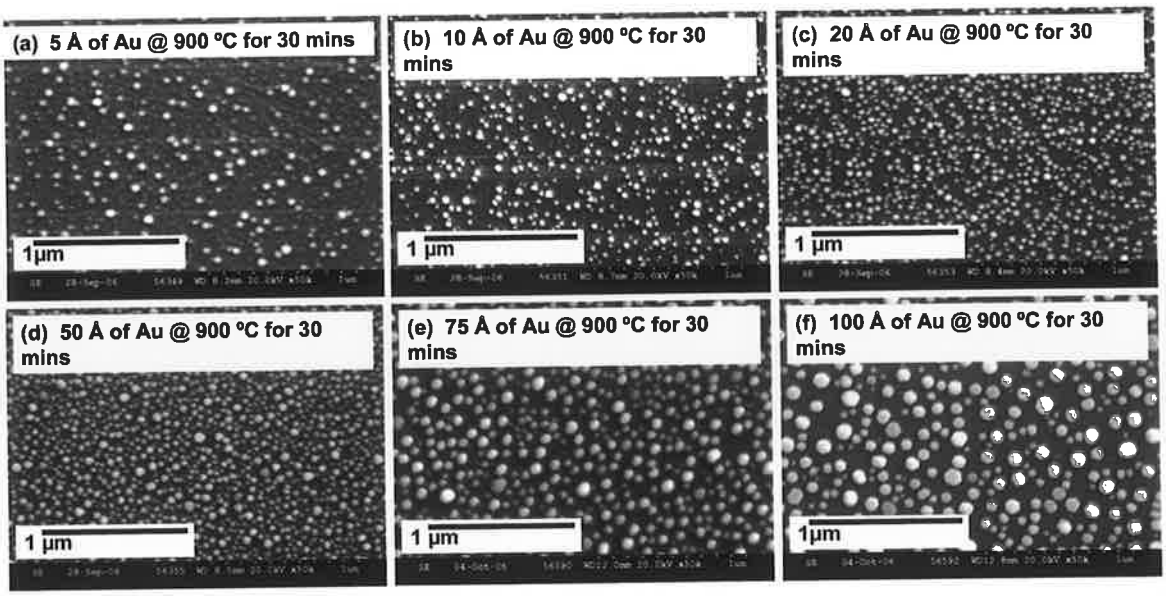

Figure 4.11 FESEM images of variety of Au thin film thickness (5 Å, 10 Å, 20 Å, 50 Å, 75 Å, 100 Å annealed at 900 °C

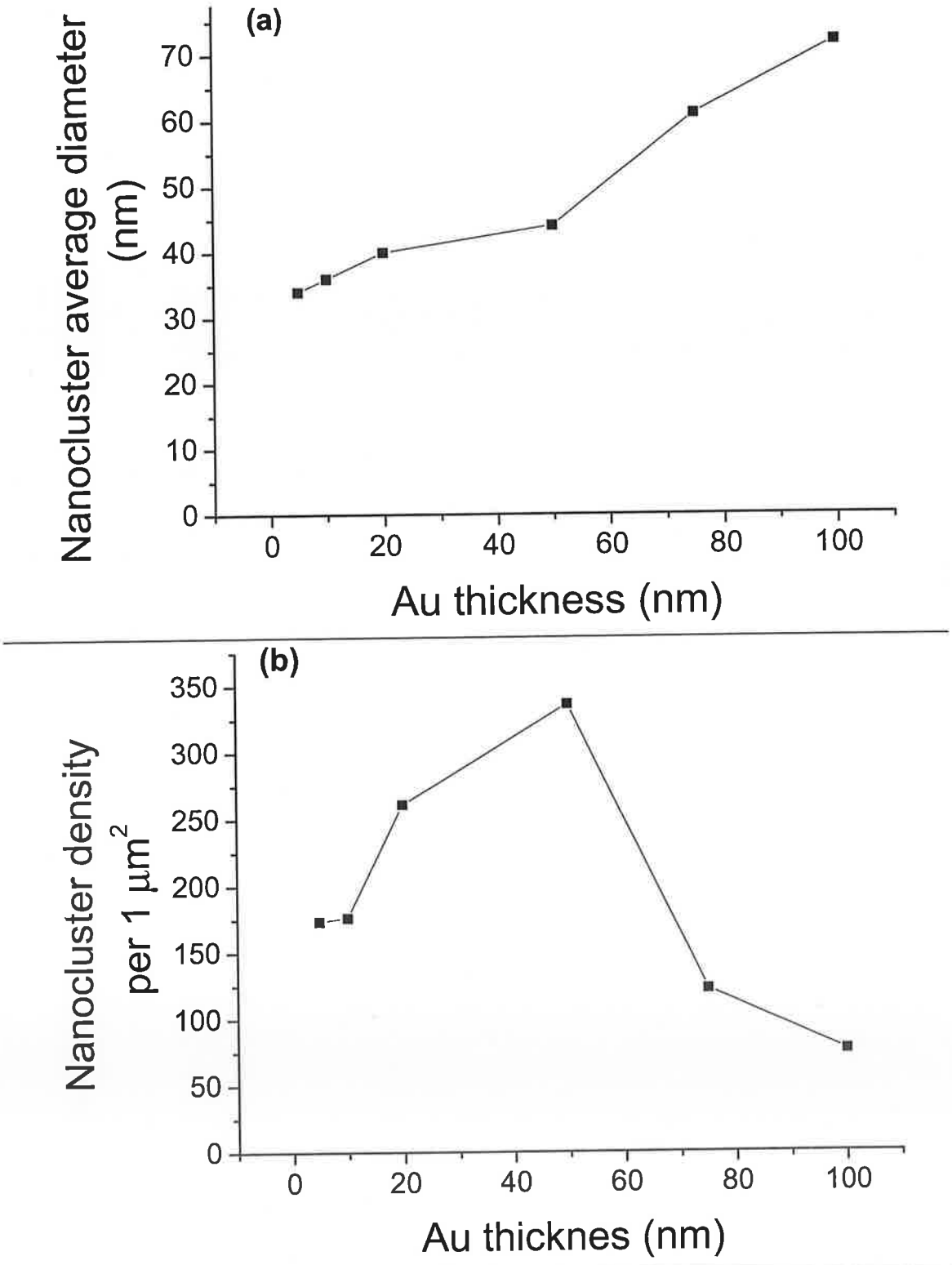

Figure 4.12 Graph of various diameter of nanocluster vs Au film thickness (a); Graph of various density of nanocluster vs Au film thickness (b)

Au Thickness	Figure	Annealed @ 900 °C		
		Number of counted nanoclusters	Nanocluster average diameter (nm)	Nanocluster density per 1 μm^2
5 Å	4.11(a)	~ 787	~ 34 ± 26	~ 173
10 Å	4.11(b)	~ 798	~ 36 ± 16	~ 176
20 Å	4.11(c)	~ 1184	~ 40 ± 14	~ 260
50 Å	4.11(d)	~ 1529	~ 44 ± 20	~ 336
75 Å	4.11(e)	~ 553	~ 61 ± 24	~ 122
100 Å	4.11(f)	~ 346	~ 72 ± 32	~ 76

Table 4.4 Summary of nanocluster average size and density per 1 μm^2, annealed at 900 °C for various Au thickness films

The reasons for this behavior are not fully clear, however we can speculate as to some of the possible mechanisms. Very thin Au films (≤ 20 Å) will melt at 900 °C, based on the data in Figure 4.10, while thicker Au films (≥50 Å) will probably not melt. The estimation of melting temperature for the 50 Å film as 977 °C from the data of Wautelet [12] is based on a very simple model using a single crystal thin film. The experimental data from Borel indicate a melting temperature for 50 Å spheres of ~ 830 °C. In fact, the deposited Au film is likely to be polycrystalline with a variety of grain sizes and shapes and therefore a melting temperature around 900 °C, between the two extremes of a perfect thin film and a collection of perfect nanospheres is quite reasonable. Thus the cluster formation and coarsening mechanisms are likely to be quite different for the thinnest and thickest films, with surface diffusion dominating for thicker Au films. This difference in nanocluster formation mechanism may also be responsible for the facetted morphology of the nanoclusters formed from thicker films during annealing. These ideas will require further investigation to substantiate or refute them. There is no evidence from FESEM data of any interaction between the Au and sapphire substrate (of the type seen for growth on Si where a Si-Au alloy is formed [7]).

It also must be borne in mind that while the data above provide reasonable guidelines for choice of Au film thickness for VLS growth, the presence of Zn vapour during actual

growth and the formation of an Au-Zn liquid alloy as discussed in chapter 2 will undoubtedly alter the cluster formation and coarsening processes during growth.

Diameter control of ZnO nanorods is important because many physical properties are diameter dependent, such as the Young's modulus [13], the surface to volume ratio etc. According to the VLS mechanism, the diameter of nanorods is determined by the size of the alloy droplet, which is in turn determined by the original cluster size. By using different sizes of metal nanoclusters, nanorods with a range of diameters can be synthesized. Figure 4.13 shows FESEM pictures of ZnO nanorods grown at a source temperature of 950 °C and a substrate temperature of 925 °C using a range of Au film thicknesses. The data shown previously in Figure 4.11 suggest that by tuning the thickness of the Au thin film we can control the diameter and density of the ZnO nanorods. We can clearly see that ZnO nanorods which are grown with a 5 Å Au film are much thinner (average diameter ~ 50 nm) than nanorods grown with thicker Au films (Figure 4.13). They appear to be very well separated with low density (~ 3 nanorods / μm^2). This is entirely consistent with what we would expect from Figure 4.11(a) where small and well separated nanoclusters of Au are formed using a 5 Å Au film. There are also a number of 2D sheet-like structures evident in the SEM data, but the origin of these is still unclear.

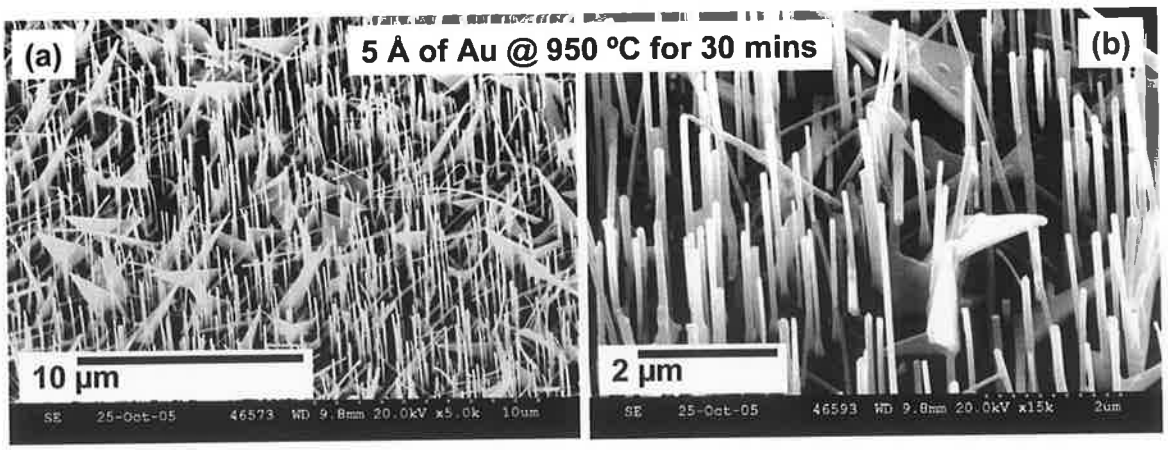

Figure 4.13 Shows FESEM pictures of ZnO nanorods grown at 950 °C for 30 minutes on 5 Å Au thicknesses film, (a) low magnification image, (b) high magnification image

However when we examine the data for ZnO nanorods grown using 20 Å and 50 Å Au films we see that there is no significant difference between them, in terms of diameter and density (with both having average diameters of ~ 76 nm and ~ 95 nm with average densities of ~ 15 nanorods / μm^2 and ~ 22 nanorods / μm^2 respectively) unlike Figures 4.14 and 4.15 although there does appear to be some difference in the size of the Au 'cap' on the top of the grown nanorods. Thus, the thickness of the initially deposited Au film does appear to have an effect on the ZnO nanorod diameter and spacing, particularly for thinner Au films, in agreement with the standard VLS mechanism, but for thicker Au films this relationship appears to break down.

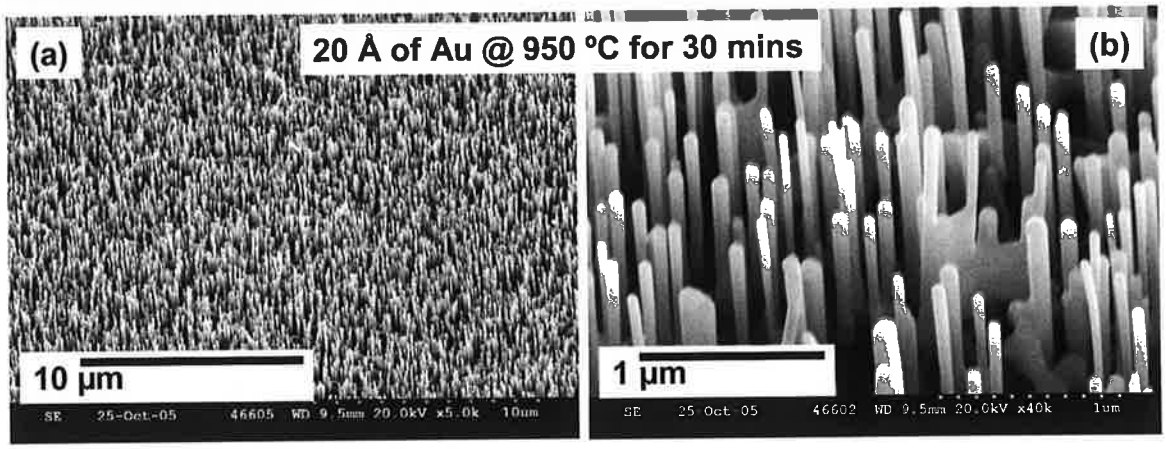

Figure 4.14 Shows FESEM pictures of ZnO nanorods grown at 950 °C for 30 minutes on 20 Å Au thicknesses film, (a) low magnification image, (b) high magnification image

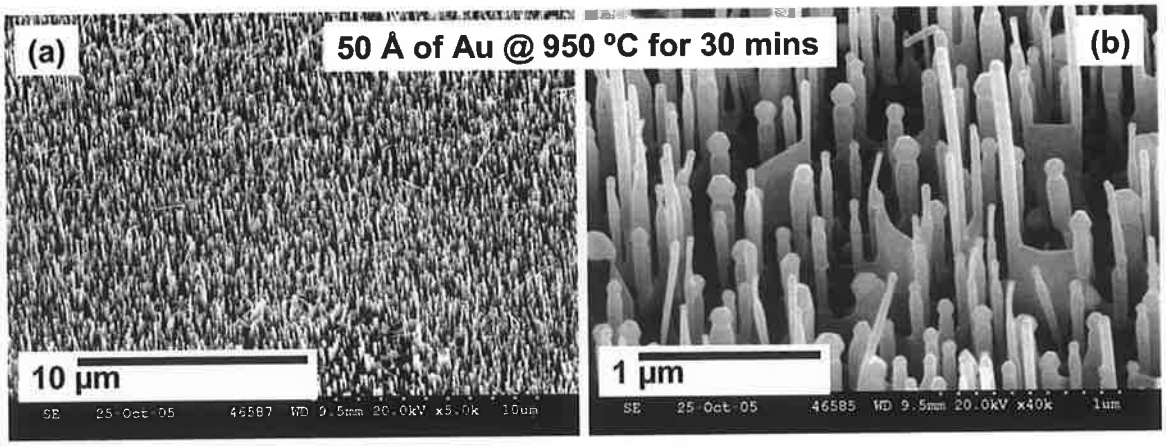

Figure 4.15 Shows FESEM pictures of ZnO nanorods grown at 950 °C for 30 minutes on 50 Å Au thicknesses film, (a) low magnification image, (b) high magnification image

There is also a thickness limit on the Au film in order to grow ZnO nanorods. We have observed that no ZnO nanorod growth is observed using a 100 Å Au film deposited on the *a*-plane sapphire (Figure 4.16). This is consistent with our previous observation concerning the manner in which the thicker Au film beads up to form nanoclusters. 100 Å Au films appear not to melt in this temperature region, and it may be the case that the Au-Zn alloy necessary for VLS growth will not form with a solid Au nanocluster.

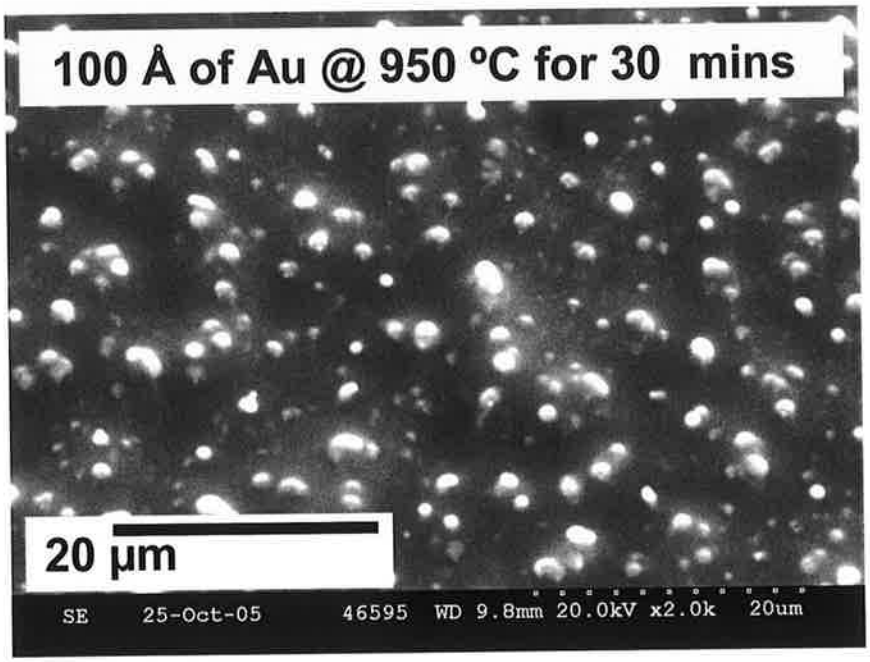

Figure 4.16 Shows FESEM pictures of ZnO nanorods grown at 950 °C for 30 minutes on 100 Å Au thicknesses film

In the Table 4.5 nanorods average diameter and density is summarized for nanorods grown on 5 Å, 20 Å and 50 Å Au thin films.

Au Thickness	Figure	Number of counted nanoclusters	Nanocluster average diameter (nm)	Nanocluster density per 1 µm^2
5	4.13(b)	131	50 ± 12	2
20	4.14(b)	103	76 ± 5	15
50	4.15(b)	156	95 ± 5	22

Table 4.5 Summary of nanorods average diameter and density per per 1 µm^2 grown on 5 Å, 20 Å and 50 Å Au thin films.

Based on the data above, we in the majority of the data we report subsequently we have used either a 20 Å Au film thickness or a 50 Å Au film thickness when growing ZnO nanostructures on *a*-sapphire.

One clear advantage of VLS growth of ZnO nanorods is that the nanorods grow only in regions where Au films have been deposited and thus the nanorod growth locations can be controlled by appropriate lithographic definition of the catalytic Au films. Various techniques for controlling the Au film locations can be utilized in this respect, including e.g. thin film deposition using a shadow mask, commercial Au colloids [7] and nanosphere-lithography [14] (Appendix I) can be used to create patterns of Au thin film for the successive semiconductor nanowire growth. An example of this is shown in Figure 4.17 with an FESEM image of ZnO nanorods/nanowalls grown on patterned Au islands on a sapphire substrate. It is clear that nanorods/nanowalls grow only from the substrate region that is coated with Au. This result shows that the growth of ZnO nanostructures on the silicon/sapphire substrates can be positioned and controlled by Au patterning substrates, which can be easily integrated with current semiconductor technology.

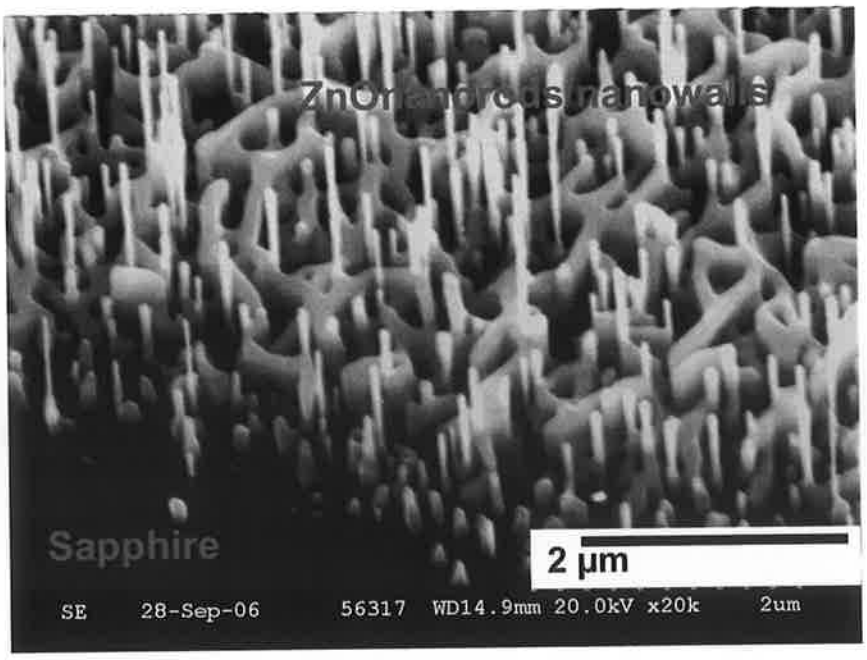

Figure 4.17 Selective growth of ZnO nanorods/nanowalls on sapphire substrates. The location of growth of the ZnO nanorods/nanowalls is defined by the location of the initial Au thin film.

4.2.2 Growth Temperature Effects

In the VPT growth system we have used, the source powder and substrate generally are placed close to each other (~ 3 cm separation) in the alumina boat at the furnace centre. Differences in the source and substrate temperatures are caused by the temperature profile of the furnace, as shown in chapter 3, and are typically not more than 25 °C, with the substrate at a slightly lower temperature. Because the majority of our experiments occur at or above 900 °C, while the boiling point of Zn is 904 °C, classical ideas of vapour phase crystal growth by condensation from a supersaturated vapour are of less relevance in our system. For the most part the substrate is close to or above the Zn boiling point and supersaturation is a less meaningful concept, certainly as applied to homogeneous nucleation. However heterogeneous nucleation of vapour at suitable locations on the substrate or elsewhere can still provide a driving force for nanostructure growth. For example the nucleation of Zn at Au nanoclusters is due to the chemical affinity for Zn to alloy with the molten Au nanoclusters, and then subsequently reacting with O_2 to form ZnO nanorods.

In addition to influencing the melting of the catalyst layer, the main effect of temperature changes in our growth system is to change the Zn vapour pressure by increasing the rate of the carbothermal reduction of the ZnO powder. As discussed in chapter 2 the carbothermal reduction process can be described by an Ellingham diagram [15] and it predicts that the reaction proceeds for a ZnO-C mixture above ~ 950 °C. Below this temperature the Zn vapour pressure will be very low and above it the vapour pressure will increase dramatically.

Figure 4.18 shows the ZnO nanostructures growth with various Au film thicknesses (5 Å, 20 Å and 50 Å) on *a*-sapphire at source temperatures of 900 °C, 950 °C and 1125 °C for 30 minutes (sample temperatures of 875 °C, 925 °C and 1100 °C). From these figures, we can conclude that for 900 °C growth temperature, well aligned ZnO nanorods are just beginning to nucleate and grow (Figure 4.18 (a), (d), (g)). This is consistent with the low Zn pressure in the growth chamber. Growth at 950 °C for 30 minutes shows well aligned ZnO nanorods

for all Au film thicknesses (Figure 4.18 (b), (e), (h). At higher temperatures (1125 °C) it appears that well aligned nanorods do not grow on *a*-sapphire. For Au film thicknesses of 5 Å and 20 Å it appears that we get 2-D ZnO structures, while no growth is seen at Au film thicknesses of 50 Å at 1125 °C. While the high Zn pressure in the chamber might explain the 2-D growth seen in Figures 4.18(c) and 4.18(f), as heterogeneous nucleation of Zn on the sidewalls of growing ZnO nanorods may begin to occur at high Zn pressure, the reasons for the absence of growth on 50 Å Au films is still under investigation. At all these temperatures growth is seen only on regions of the sapphire where Au films have been deposited and it appears that the initial growth proceeds via the VLS mechanism, even if heterogeneous nucleation on growing ZnO structures occurs subsequently at high temperatures.

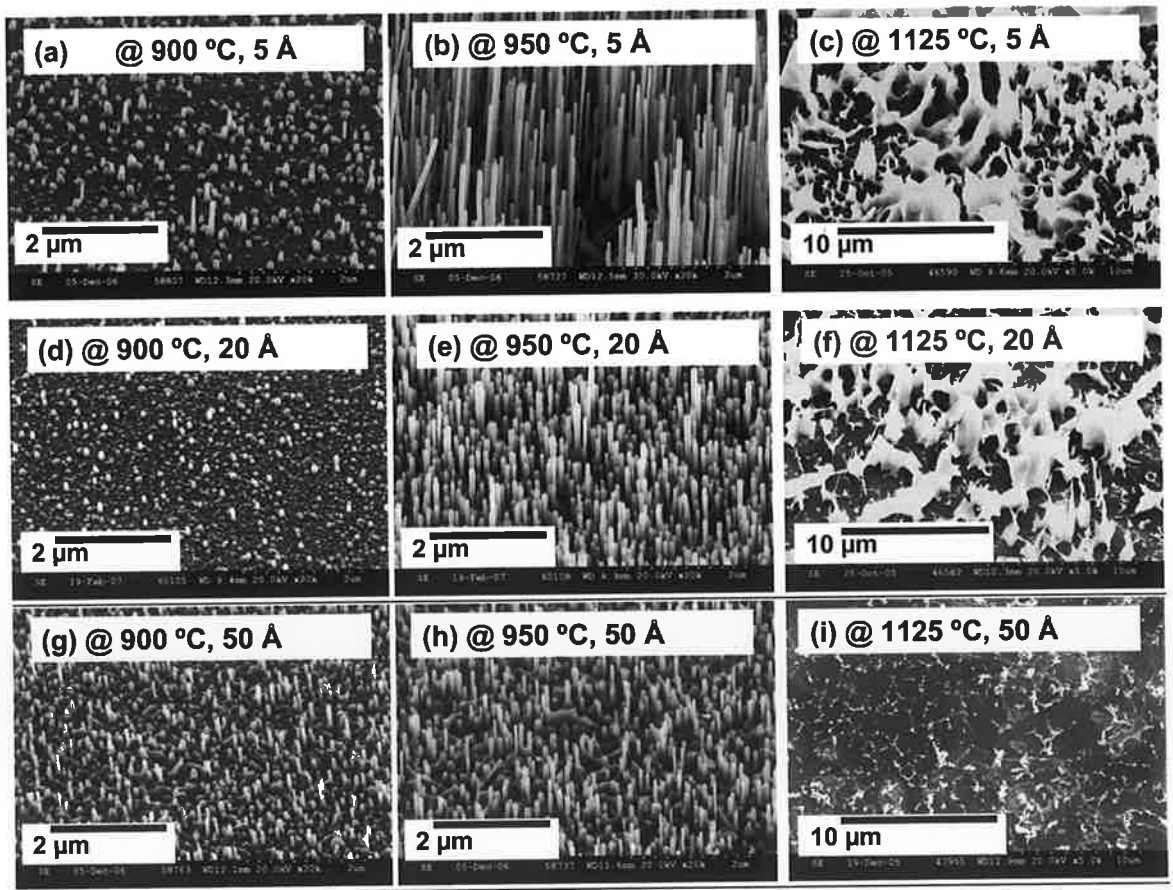

Figure 4.18 FESEM images of 1 step growth at 900 °C, 950 °C and 1125 °C for 30 minutes on various gold thickness layers : 900 °C & 5 Å (a), 950 °C & 5 Å (b), 1125 °C & 5 Å (c), 900 °C & 20 Å (d), 950 °C & 20 Å(e), 1125 °C & 20 Å (f), 900 °C & 50 Å (g), 950 °C & 50 Å (h), 1125 °C & 50 Å (i).

Based on these data the majority of our ZnO nanostructures were grown at source powder temperatures in the range 900 – 950 °C.

4.2.3 Growth Duration

We have also studied the effects of varying growth duration on the growth of ZnO nanostructures. For growth at 900 °C the longer durations will lead to longer ZnO nanorods. This is shown in Figure 4.19 below. However it can also be seen that a foam-like layer of interconnecting "nanowalls" becomes apparent for growths at longer times on samples with 20 Å and 50 Å Au film thicknesses. Growth at 950 °C for 30 minute and 60 minute durations show well aligned ZnO nanorods whose length increases with duration. Interconnecting nanowall structures are not so apparent for growth at 950 °C and are not seen for growth using a 5 Å Au film thickness at either 900 °C or 950 °C.

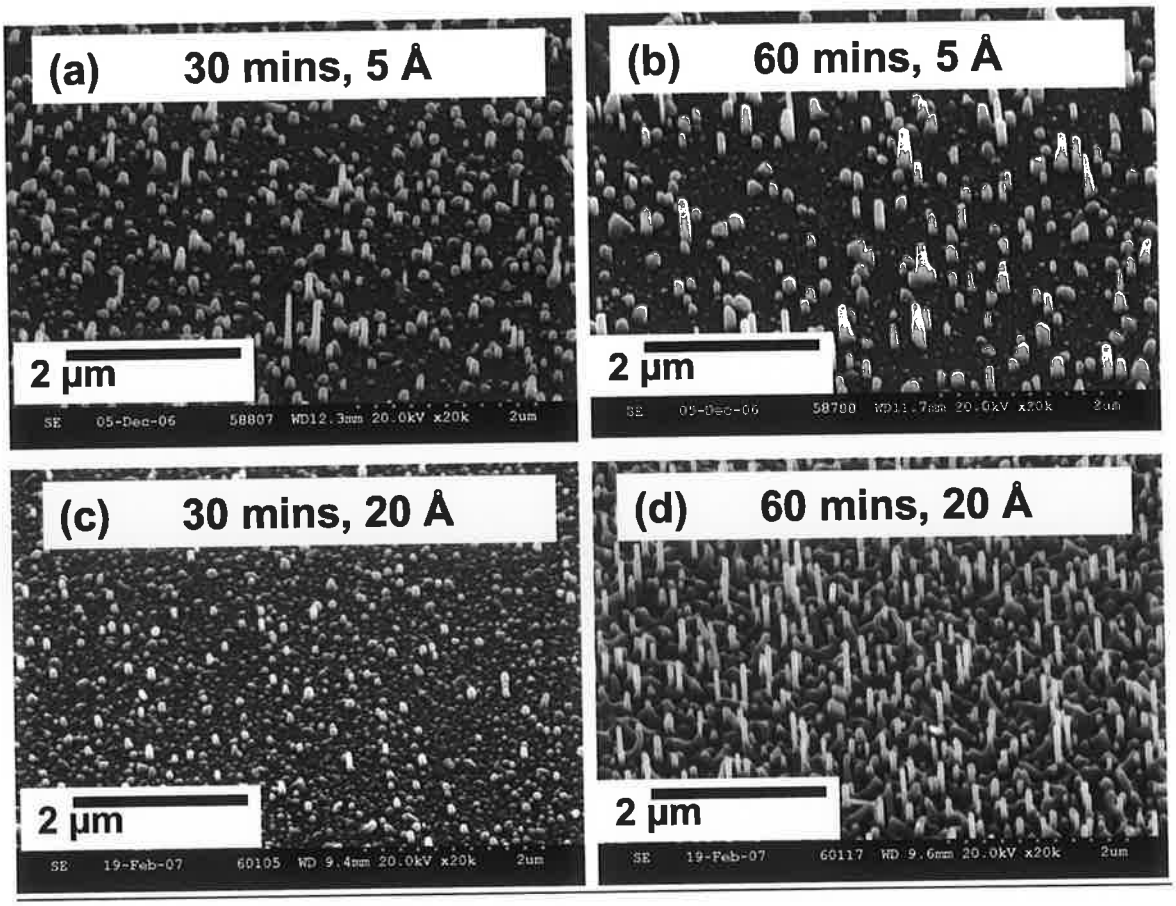

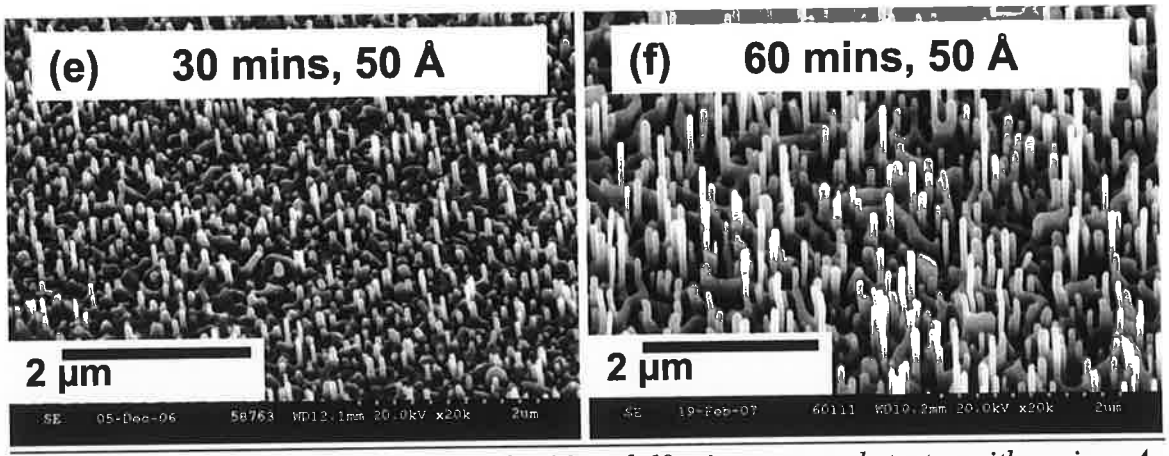

Figure 4.19 Samples grown at 900 °C for 30 and 60 minutes on substrates with various Au thickness (5 Å, 20 Å, 50 Å). (a) growth for 30 minutes on 5 Å, (b) growth for 60 minutes on 5 Å, (c) growth for 30 minutes on 20 Å, (d) growth for 60 minutes on 20 Å, (e) growth for 30 minutes on 50 Å, (f) growth for 60 minutes on 50 Å,

Based on these data the majority of our growth experiments used durations in the range 30 – 60 minutes. Beyond a growth duration of 60 minutes no further growth is expected due to the flushing of residual oxygen from the furnace tube by the Ar carrier gas flow, discussed in chapter 2.

4.2.4 Nanorod/Nanowall Morphology

The nanorod/nanowall morphology (seen in Figure 4.19(f)) is a potentially interesting one, which forms the basis of part of the next chapter. It is of potential technological use because the nanowall network might provide an electrical connection to the nanorods on the insulating sapphire substrate which could be useful e.g. for field emission device applications. We have made very basic lateral electrical continuity tests across a region of a nanorod/nanowall sample and also across a sample which shows only nanorods and in the former case a finite electrical resistance is measured (~ 50 Ω) while in the latter an open circuit is measured. For these reasons some attention was given to the possible reasons for the formation of this morphology and the potential to control the growth to achieve this mixed structure.

There appear to be three parameters of particular importance in the synthesis of the nanorod/nanowall mixed morphology. Au film thickness, growth duration and temperature all affect this morphology. At very small Au film thicknesses (5 Å) we see only well separated ZnO nanorods at growth temperatures of both 900 °C and 950 °C, whereas at larger Au film thicknesses of 20 Å & 50 Å a mixed nanorod/nanowall morphology is seen for growths at 900 °C. The nanowall structures become more apparent for longer growth durations at this temperature and these Au film thicknesses.

Because of the multiplicity of factors which influence the growth the identification of the key features associated with the nanorod/nanowall morphology are hard to identify. Various other groups have reported this morphology and associated it with (a) the presence of thicker Au catalytic films which have multiple "grain boundaries" along which VLS growth of nanowalls [16] or (b) the effects of Al contamination in the source powder [17]. It is also worth considering the possibility of VS deposition on growing nanorods as a source of nanowalls. This final explanation does not seem to be consistent with our data for the growth of the nanorod/nanowall morphology however since we observe this morphology even at low growth temperatures where the Zn vapour pressure is low and the growth rates are low. In addition the nanowall growth occurs only at the bases of the nanorods rather than randomly along their lengths as one would expect with VS deposition. In addition it is extremely hard to see how this explanation can account for the curved wall structures connecting nanorods as VS nanostructure growth would generally be expected to occur on specific crystal faces and produce a well-defined "habit". Explanation (b) is also not consistent with our data. Our source powders are 99.999% purity with negligible Al contamination and furthermore the same source material supply is used to grow samples where only well separated nanorods are observed.

The most likely explanation for the mixed nanorod/nanowall morphology is therefore the effect of thicker Au films. This is consistent with our data where the mixed morphology is only seen in samples with a high density of Au nanoclusters, as in Figures 4.11(c) and 4.11(d) above, where the Au nanoclusters are almost touching. The regions of contact between Au nanoclusters (effectively "grain boundaries", though the clusters will be molten)

will be preferential sites for precipitation and oxidation of Zn to form nanowalls during VLS growth as the grain boundary can allow both O_2 diffusion to the sapphire surface and preferential Zn precipitation, enabling the formation of a foam-like connection of nanowalls during the early stages of growth. The observation of this mixed morphology at the lower growth temperature of 900 °C is also consistent with this explanation as the formation of Au nanoclusters is temperature dependent and the density is reduced (and hence the separation increased) by higher growth temperatures. An example of the effects of annealing a 20 Å Au film at 800 °C and 900 °C is shown in Figure 4.20 below and the increase in separation of the Au nanoclusters at the higher temperature anneal is clearly seen. These data indicate that the average nanocluster diameter formed from Au film thicknesses ≤ 20 Å annealed at 800 °C and 900 °C are roughly constant at ~ 32.5 nm and 40 nm respectively, with the density ~ 722.5 per 1 μm^2 and ~ 260 per 1 μm^2.

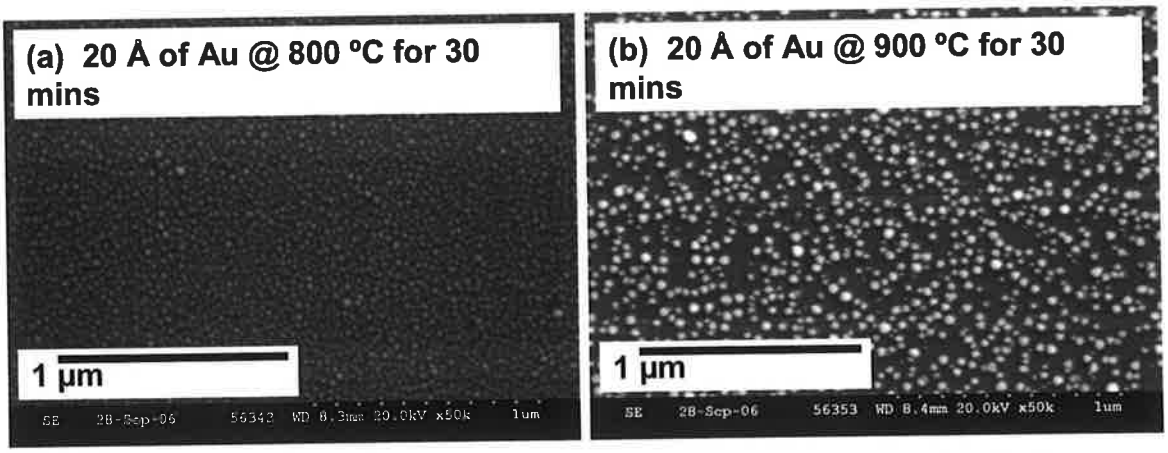

Figure 4.20 shows effects of annealing a 20 Å Au film at 800 °C (a) and 900 °C (b)

We summarise these conclusion in Figure 4.21 below.

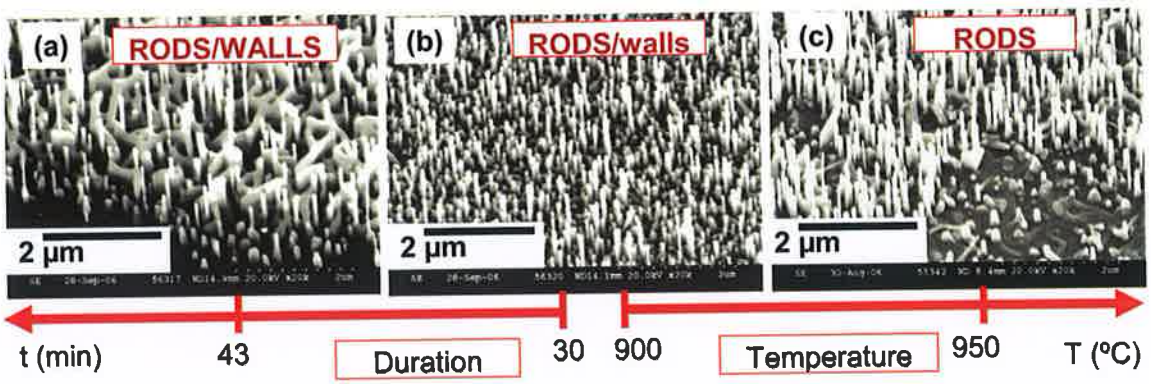

Figure 4.21 FESEM images of ZnO nanorods and nanorods/nanowalls grown on 20 Å of Au thin film. (a) ZnO nanorods/nanowalls grown at 900 °C for 43 minutes, (b) nanorods with very small nanowalls at the bottom grown at 900 °C for 30 minutes. (c) ZnO well separated nanorods grown at 950 °C for 30 minutes

4.3 Concluding Remarks

The results of the initial series of experiments using the growth apparatus described in chapter 3 have been presented. Various substrates were used in preliminary experiments to compare with published data in the literature as a method of commissioning the new VPT growth system. These experiments yielded data which was comparable to the literature results. The next series of experiments (and all other reported in this chapter) utilized *a*-sapphire substrates which enable high quality well aligned nanorods to be grown. Initial growth of such structures were studied using SEM, XRD and room temperature PL and showed excellent morphology, in terms of alignment perpendicular to the substrate, crystal quality and optical properties. A detailed series of experiments then studied the effects of variations in all the major parameters involved in the growth including Au catalyst film thickness and nanocluster formation, growth temperature and duration, enabling us to locate the optimum region of parameter space for growth of well aligned ZnO nanorods and to understand the effects of the various growth parameters on the morphologies of the ZnO structures.

The nanorod/nanowall mixed morphology structure was investigated and our experimental data was compared with existing hypotheses in the literature concerning the growth mechanisms for this morphology. Our data are in agreement with the hypothesis that the nanowall morphology is due to VLS growth at boundaries between Au nanoclusters, and seem to rule out the other explanations proposed in the literature.

The nanorod/nanowall morphology shows interesting optical properties in comparison with well separated nanorods which will form the main part of the next chapter of the thesis.

4.4 References

[1] J. Grabowska, K. K. Nanda, E. McGlynn, J.-P. Mosnier, M. O. Henry, *Surface & Coatings Technology* **200** (2005) 1093

[2] J. Grabowska, K. K. Nanda, E. McGlynn, J.-P. Mosnier, M. O. Henry, A. Beaucamp, A. Meaney, *Journal of Material Science: Materials in Electronics* **16** (2005) 397

[3] X. Y. Kong, Y. Ding, R. Yang, Z. L. Wang, *Science* **303** (2004) 1348

[4] C. Ronning, P. X. Gao, Y. Ding, Z. L. Wang, *Applied Physics Letters* **84** (2004) 783

[5] P. Fons, K. Iwata, A. Yamada, K. Matsubara, S. Niki, K. Nakahara, T. Tanabe, H. Takasu, *Applied Physics Letters* **77** (2000) 1801

[6] M. H. Huang, Y. Wu, H. Feick, N. Tran, E. Weber, P. Yang, *Advanced Materials* **13** (2001) 113

[7] Y. Li, M. Feneberg, A. Reiser, M. Schirra, R. Enchelmaier, A, Ladenburger, A. Langlois, R. Sauer, K. Thonke, J. Cai, H. Rauscher, *Journal of Applied Physics* **99** (2006) 054307

[8] Joint Committee on Powder Diffraction Standards (JCPDS) as follows: ZnO - JCPDS card no. 36-1451

[9] L. Wang, N. C. Giles *Journal of Applied Physics* **94** (2003) 973

[10] K. Vanheusden, W. L. Warren, C. H. Seager, D. R. Tallant, J. A. Voight, B. E. Gnade, *Journal Applied Physics* **79** (1996) 7983

[11] Ph. Buffat and J-P. Borel, *Physical Review A* 13 (1976) 2287

[12] M. Wautelet, *European Journal of Physics* **16** (1995) 283

[13] X. D. Bai, P. X. Gao, Z. L. Wang, *Applied Physics Letters* **82** (2003) 4806

[14] H. J. Fan, B. Fuhrmann, R. Scholz, C. Himcinschi, A. Berger, H. Leipner, A. Dadgar, A. Krost, S. Christiansen, U. Gosele, M. Zacharias, *Nanotechnology* **17** (2006) S231

[15] P. W. Atkins, book, *Physical Chemistry*, 5th edition, Oxford University Press (1994). Ellingham diagrams, Chapter 10, R. T. Dehoff, Thermodynamics in Material Science, McGraw-Hill, New York (1993)

[16] H. T. Ng, J. Li, M. K. Smith, P. Nguyen, A. Cassell, J. Han, M. Meyyappan, *Science* **300** (2003) 1249

[17] A. Rahm, G. W. Yang, M. Lorenz, T. Nobis, J. Lenzner, G. Wagner, M. Grundmann, *Thin Solid Films* **486** (2005) 191

5 PL Study of the Zinc Oxide Nanorods/Nanowall System

In this chapter an optical study of the ZnO nanorods/nanowall morphology is presented. The major initial result of this study is that this morphology shows extremely high optical emission intensity at low temperatures (~ 7 K) and poor optical emission intensity at room temperatures. The degree of quenching which occurs is quite unusual for ZnO nanostructures. X-ray diffraction and scanning electron microscopy show that the nanostructures are vertically well aligned with the c axis normal to the substrate and have a very low rocking curve width. Temperature dependent photoluminescence analysis indicates the ZnO nanorods/nanowall morphology nanostructures are of excellent optical quality at low temperatures, but their emission intensity is strongly quenched at higher temperatures in comparison to bulk ZnO crystals and nanorod samples with no nanowall interconnections. An excitonic emission around 3.366 eV is seen at low temperature and the intensity decays rapidly with increasing temperature. We propose that that our data on the nanorods/nanowall samples may be due either to (a) the intrinsically high surface to volume ratio associated with the nanorod/nanowall systems which leads to increased surface-related quenching or (b) the nature of the nanowall ZnO material compared to isolated nanorod structures, which may lead to quenching at e.g. grain boundary surfaces. The use of such nanostructures in room temperature optoelectronic devices appears to be dependent on the control or elimination of such deleterious surface effects.

In the previous chapter we discussed the formation of the mixed nanorods/nanowall morphology for ZnO nanostructures grown in certain conditions. As mentioned this may be potentially important for technological applications because the sapphire is an insulating substrate and the nanowall network may allow a convenient electrical back contact, which would be important in applications such as field emission where the well-aligned nanorod morphology would be quite promising in order to achieve high field enhancement factors. Basic electrical continuity checks as indicated in the previous chapter seem to support this belief.

We have discussed the control of the morphology in the previous chapter and the effects of different growth temperatures and times on the nanorod/nanowall mixed morphology. In particular the effects of the Au catalyst layer were concluded to play an important role in the formation of this morphology. For the PL study presented in this chapter we have grown samples on *a*-plane sapphire using both a single step and a two step growth process. The single step process, described in the previous chapter, involved a furnace temperature of 900 °C and a 90 sccm Ar carrier gas flow and an Au film thickness of 5 nm. The two step process utilized the same equipment and Au film thickness but the temperature profile is altered as shown in Figure 5.1 below. This growth procedure combined different steps during the growth period. By tuning temperature we can control shape of nanostructures. The lower initial furnace temperature of 760 °C appears to affect the Au nanocluster formation, possibly leading to nanowall formation as discussed in the previous chapter. We believe that ZnO nanowall growth is encouraged because the lower temperature step causes the Au film to evolve without beading up to form separate Au clusters. The higher temperature growth step on the annealed Au film then leads to the nanorod/nanowall morphology.

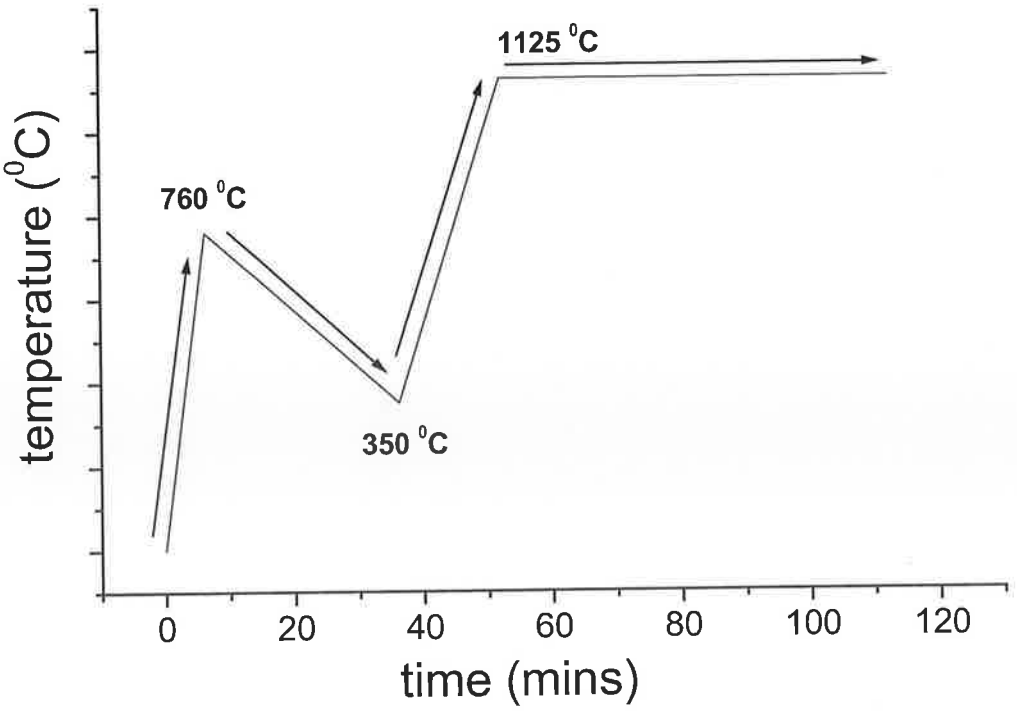

Figure 5.1 Two step growth of the nanorods/nanowalls sample

Figure 5.2 shows an FESEM image of a sample with a ~ 5 nm Au film deposited and ZnO nanostructures were grown using the two step process. In Figure 5.2(b) we clearly observe a system of vertically well aligned nanorods, with evidence of 'foam-like 'network of nanowalls below the nanorods. The structure observed is entirely consistent with the reports of Ng *et al.* and Lao *et al.*, [1, 2] who observe a similar nanowall network below a well aligned field of nanorods, as discussed below. The nanorod lengths are quite uniform with a value of ~ 1 μm, and diameters are slightly less then 100 nm. Nanowall thickness is also of the order of 100 nm and the wall heights ~ 500 nm. Vertical growth of the nanostructures is observed, and the absence of growth in the region with no Au coverage establishes the VLS growth mechanism.

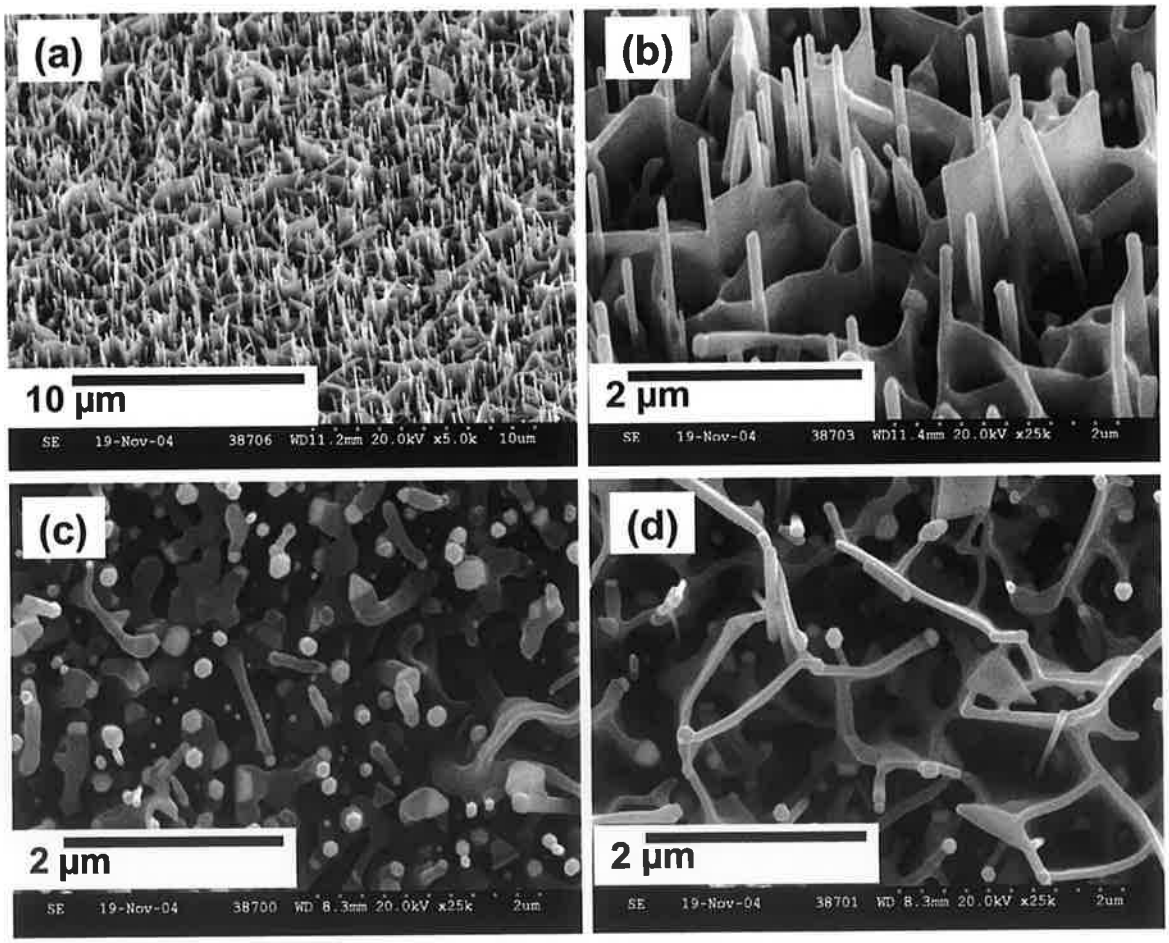

Figure 5.2 Four FESEM images of a ZnO nanowires/nanowalls sample grown on a-plane Al_2O_3; Side view with a low magnification (a), with a high magnification (b). Top view with different part of sample (c) & (d).

5.1 XRD Characterization

These samples have also been studied using XRD and this technique clearly shows that the nanorods/nanowalls grow in a textured manner on the substrate, as shown in Figure 5.3 below.

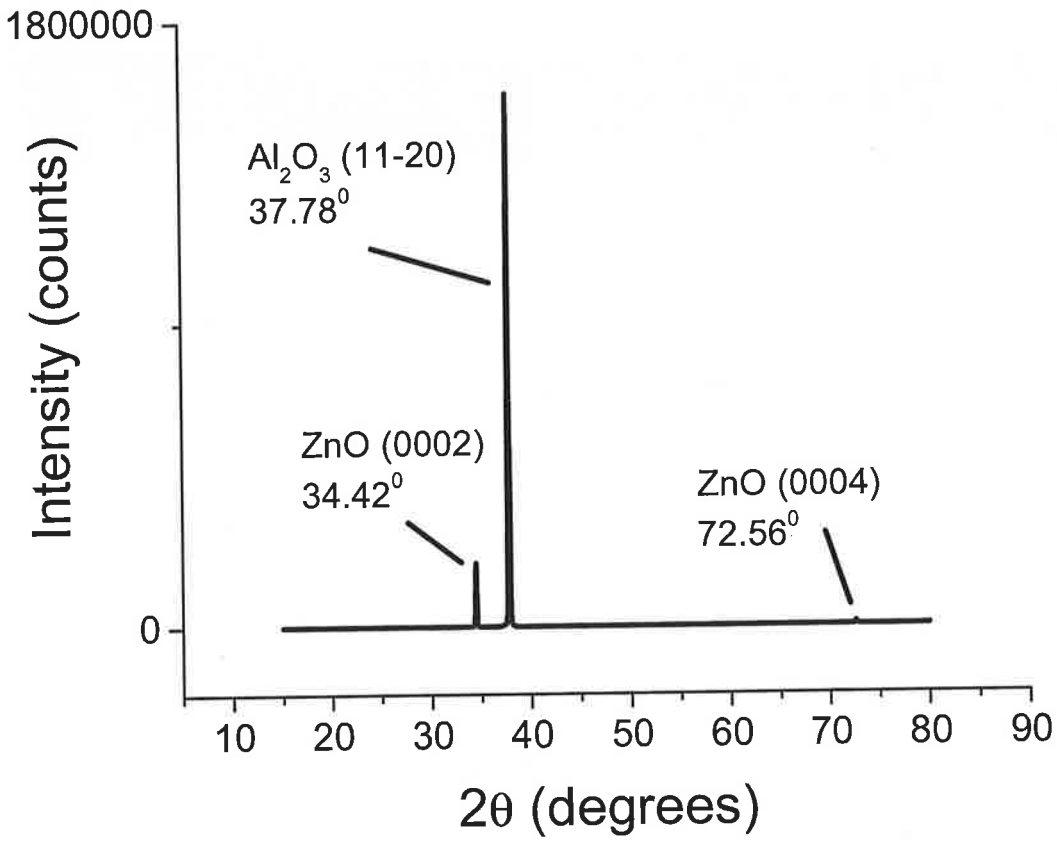

Figure 5.3 shows θ-2θ x-ray diffraction (XRD) data for ZnO nanowalls/nanorods grown on a-plane sapphire, with the ZnO (0002) and (0004) peaks clearly seen at 34.42 and 72.56 deg, respectively.

Figure 5.3 shows θ-2θ XRD data for ZnO nanowalls/nanorods grown on *a*-plane sapphire, with the ZnO (0002) and (0004) peaks clearly seen at 34.42 and 72.56 deg, respectively. The absence of any others peaks confirms the good aligment of these nanostructures with *c* axis along the nanorod axis and perpendicular to the substrate. We note that identical data are seen for a sample with well separated nanorods with no nanowall interconnections.

The rocking curve width of the (0002) peak for the nanorod/nanowall morphology (Figure 5.4(a)) sample is very low (~ 0.16 deg), one of the lowest values reported to date [3-5]. For comparison, the rocking curve width of the (0002) peak for well separated ZnO nanorods also grown on *a*-plane sapphire is ~ 0.23 deg. The very low FWHM value for both these samples indicates that the crystal quality is very good in both cases.

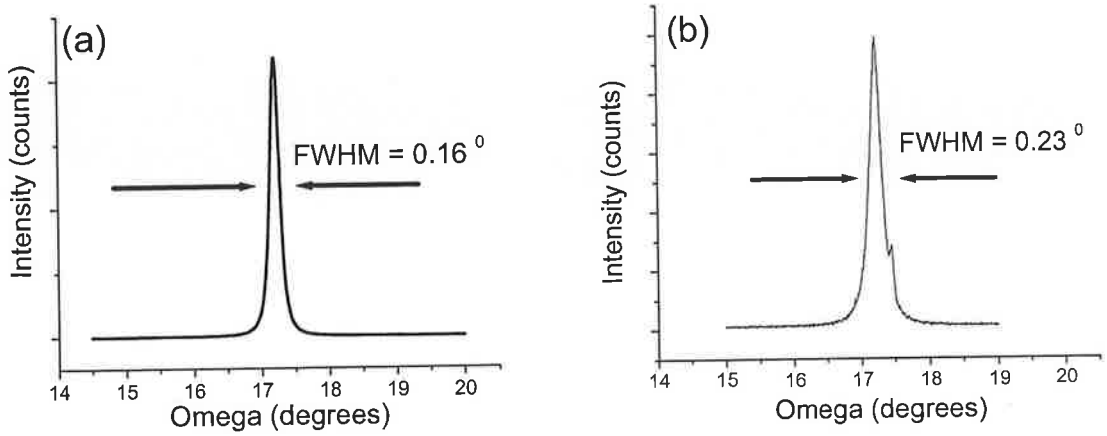

Figure 5.4 Rocking curve of nanorod/nanowall sample (a), and well separated ZnO nanorods sample.

The in-plane ordering of the ZnO nanorods was checked using x-ray phi scans. Figure 5.5 displays the corresponding phi scans for the sapphire (10-14) and ZnO (10-10) reflections, respectively for the sample with the nanorod/nanowall morphology. The sapphire reflections show two peaks separated by 180 degrees, consistent with the symmetry of the *a*-plane sapphire substrate. The ZnO reflection shows six peaks separated by 60 degrees and proves that the nanorods are grown epitaxially on the sapphire with 6 fold symmetry consistent with the (0001) texture seen in Figure 5.3 above. Once again identical data are seen for the well separated nanorod samples. The epitaxial relationship of the ZnO nanostructures on the sapphire substrate in both cases are $(0001)_{ZnO} \parallel (11\text{-}20)_{Sapphire}$ and $[11\text{-}20]_{ZnO} \parallel [0001]_{Sapphire}$, which is in agreement with other published data for growth on *a*-plane sapphire [3].

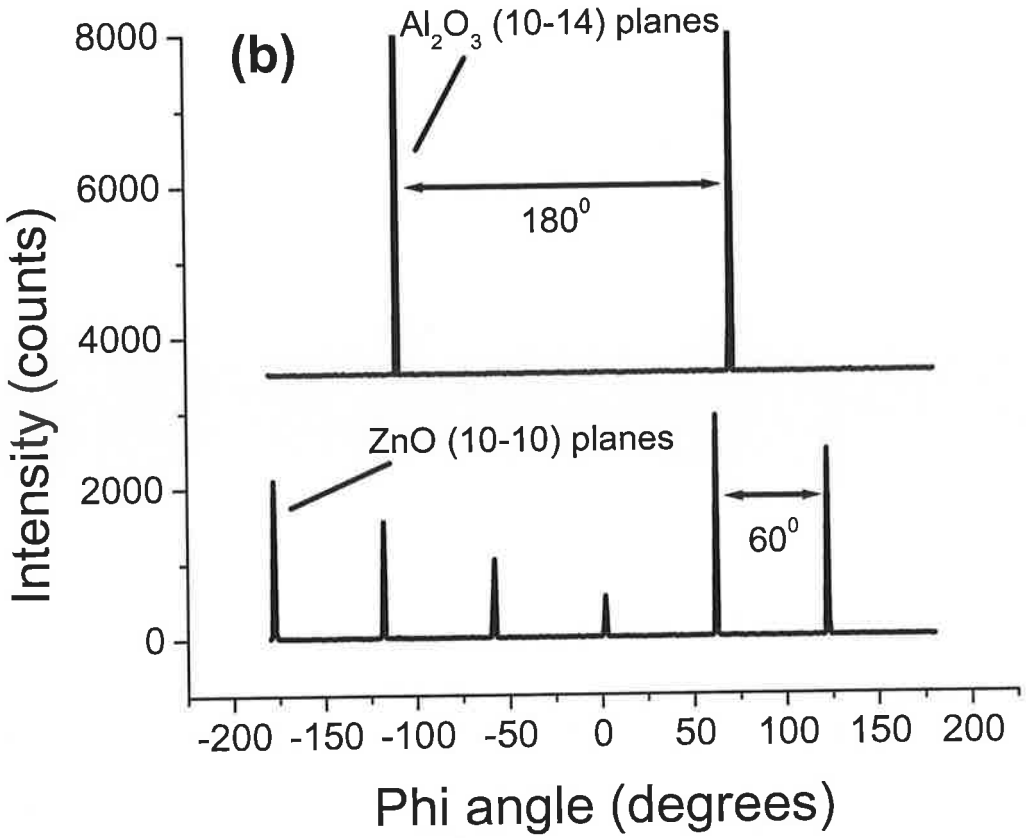

Figure 5.5 *Phi-scans of the sapphire (10-14)/ZnO (10-10) planes for nanorod/nanowall sample*

5.2 PL Characterization

As the luminescence of ZnO is very sensitive to its surface state, ZnO nanostructures with a high surface to bulk ratio are expected to make possible novel practical applications for electro-optical devices and chemical sensors. In our photoluminescence work we have studied the low temperature luminescence properties of ZnO nanorod/nanowall samples. We have compared these data with the optical properties of well separated ZnO nanorod samples and a range of bulk ZnO crystals at various temperatures. In our study, we have focused on excitonic emission and the influence of the large surface to volume ratio of these nanostructures on this emission. Others authors have commented on various aspects

of the impact of large surface to volume ratio on the optical properties of ZnO nanostructures [6, 7].

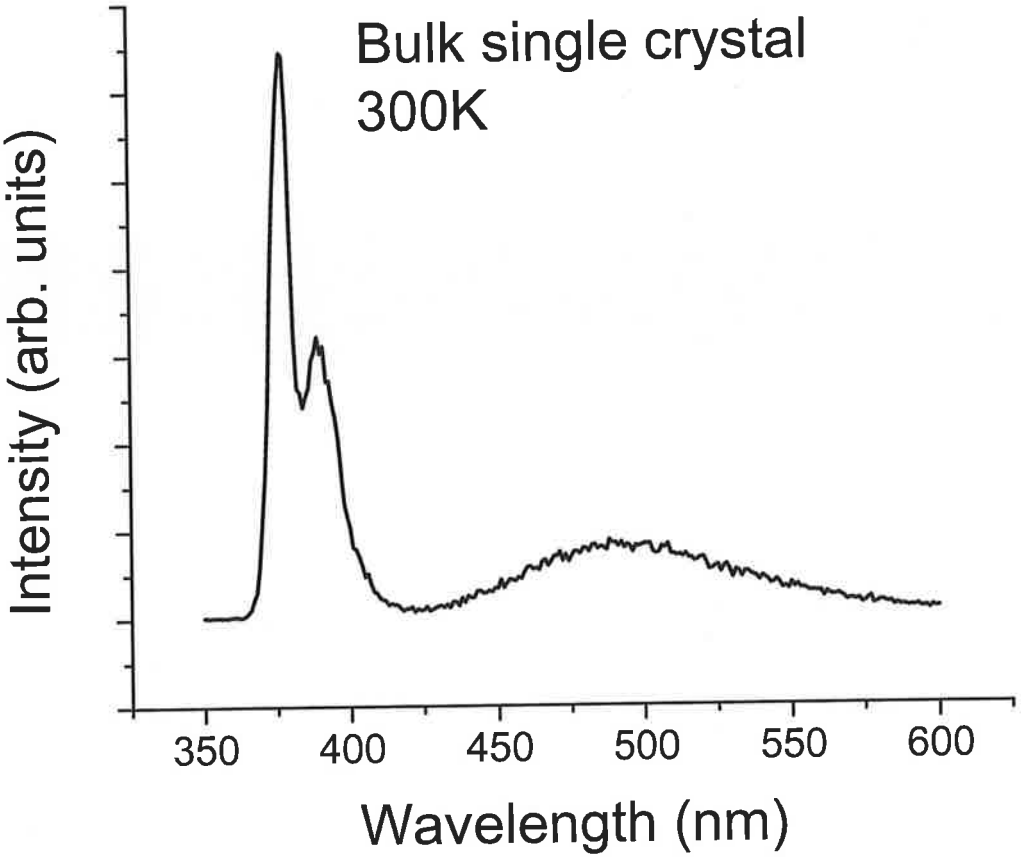

Figure 5.6 PL data at room temperature for the single crystal bulk ZnO (EP).

For comparison with the nanostructures we have grown in our lab, Figure 5.6 shows PL data of single crystal bulk ZnO at room temperature (300K). This sample was obtained from Eagle-Picher Corporation (EP, USA). For bulk ZnO we observe an extremely strong band edge luminescence and very weak green band emission, which is normal for single crystal materials.

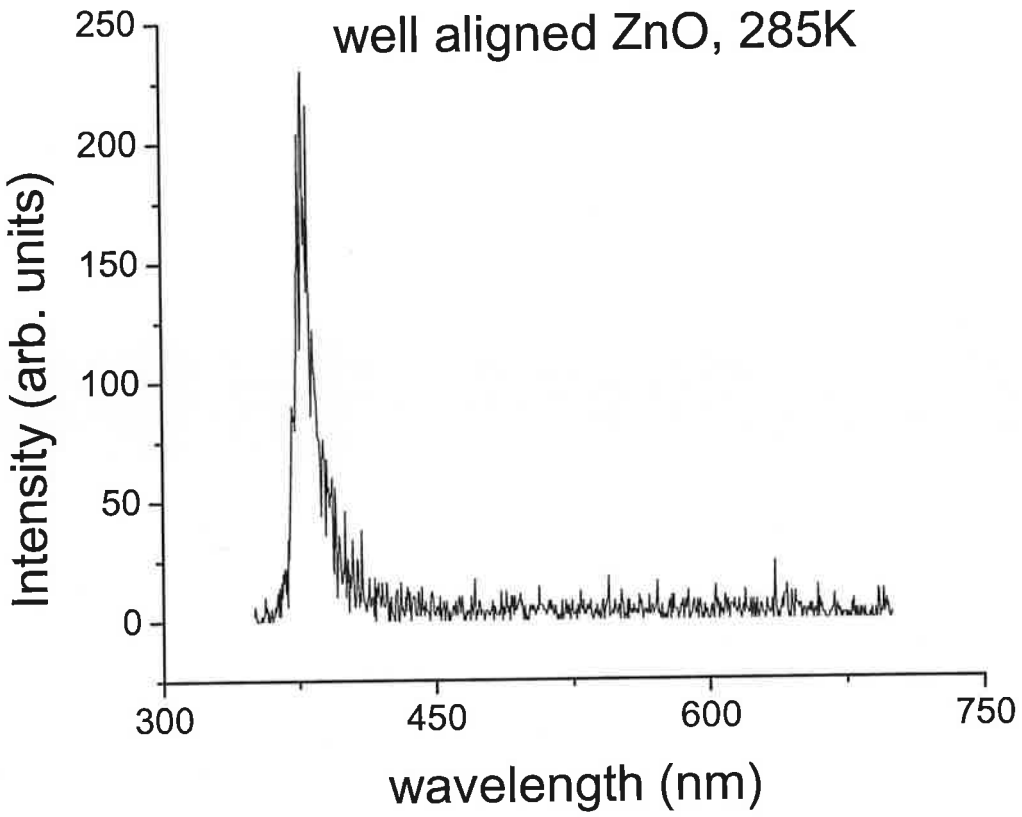

Figure 5.7 PL data at room temperature for well aligned ZnO nanostructures.

Figure 5.7 shows photoluminescence data at room temperature of well aligned ZnO nanorod sample grown in our lab. In comparison with the bulk ZnO (Figure 5.6), well aligned ZnO samples shows also strong band edge luminescence peak at 377 nm and no peak in green band emission region. These optical properties are often taken as a rough indication of high quality material.

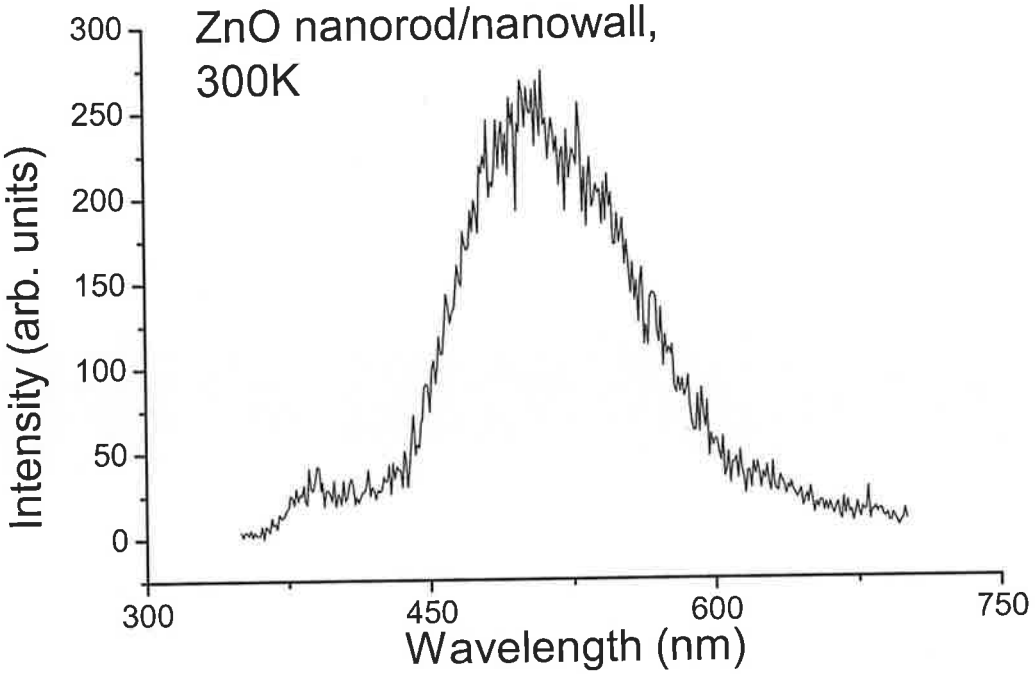

Figure 5.8 PL data at room temperature of nanorod/nanowall ZnO samples.

Figure 5.8 shows photoluminescence data for ZnO nanorod/nanowall sample taken at room temperature. For this sample, in comparison with bulk ZnO and well aligned ZnO nanorod sample, we observe rather poor band edge luminescence and a strong green band emission, which is often taken to indicate poor quality material. The series of sharp lines observed at room temperature towards shorter wavelengths are plasma lines from the HeCd laser which have not been completely removed by our filtering.

Photoluminescence data for the nanorod/nanowall sample at lower temperatures (measurement at 7 K) is shown in Figure 5.9. We observe dramatically different results for the emission from this sample at low temperature which shows a very strong and sharp band edge emission, with linewidths for individual bound exciton emissions of ~ 0.6 meV, comparable to good quality bulk material and among the smallest linewidths reported for ZnO nanostructures [3-5, 8]. We also observe the classic 'structured' green band, with distinct multi-phonon emission, which is attributed by various authors to various causes, most commonly native defects such as oxygen vacancies or Cu-related defects [9, 10]. Thus

the PL data at low temperatures indicate that these samples are of extremely good optical quality. We can compare this sample with photoluminescence data of well aligned ZnO nanorods sample taken at 7.5 K (Figure 5.10), which also show very strong band edge luminescence.

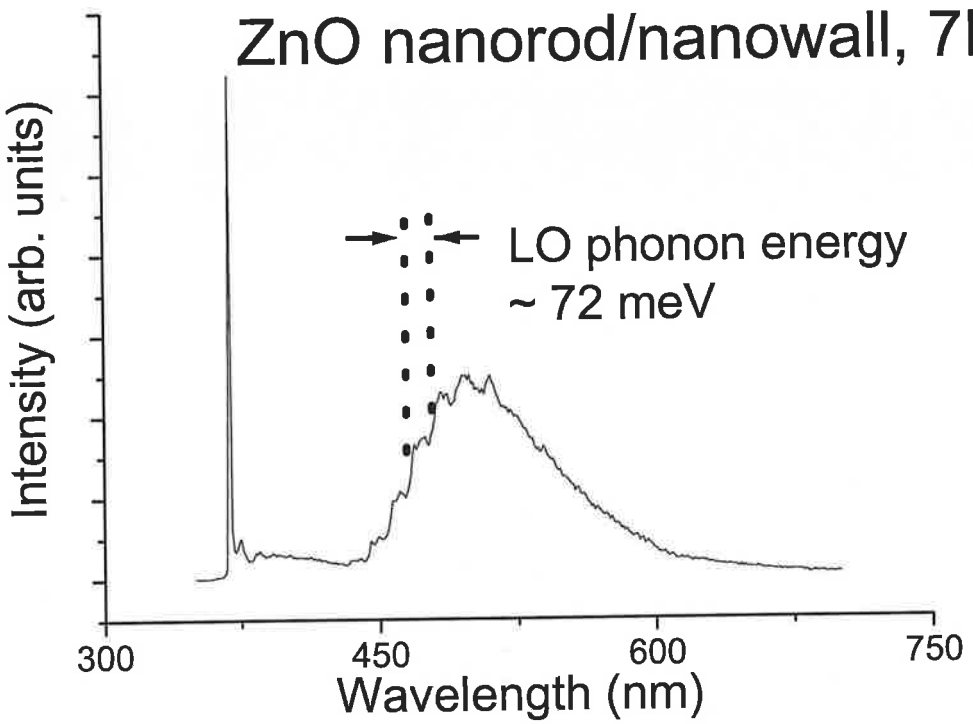

Figure 5.9 PL data at low temperature of nanorod/nanowall ZnO samples .

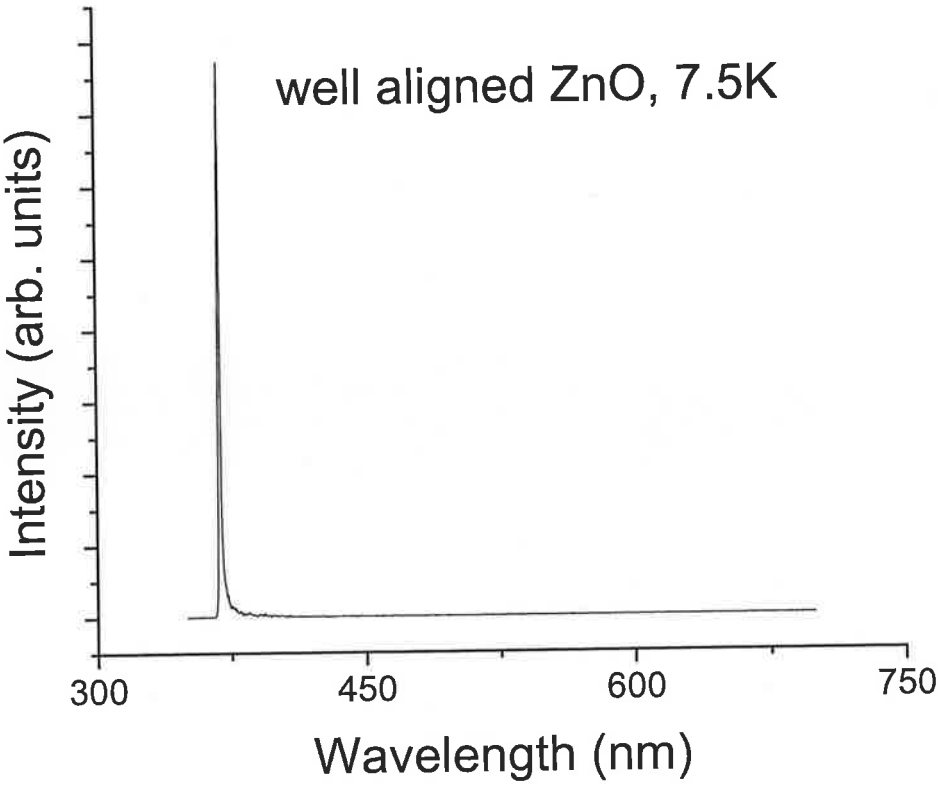

Figure 5.10 PL data at low temperature of well separated ZnO nanorod samples.

One of the most puzzling features of these PL data is the dramatic difference between the room and lower temperature PL spectra for samples which show very similar structural quality in terms of XRD measurements.

In Figure 5.11, we show the near bandedge PL signal of the nanorod/nanowall sample at 7.75 K as a function of photon energy in electron-volts (eV), and also the signal from an EP bulk signal crystal sample at 8 K. The PL spectra at low temperature for the nanorod/nanowall ZnO sample are compared to the bulk material, which has an extremely high optical quality and it may be seen that the individual bound exciton features are clearly resolved with narrow linewidths in both cases (< 1 meV, see Fig. 5.18 below). Thus the optical quality at low temperature of the ZnO nanorod/nanowall sample is clearly comparable to the bulk ZnO crystal in terms of PL linewidths.

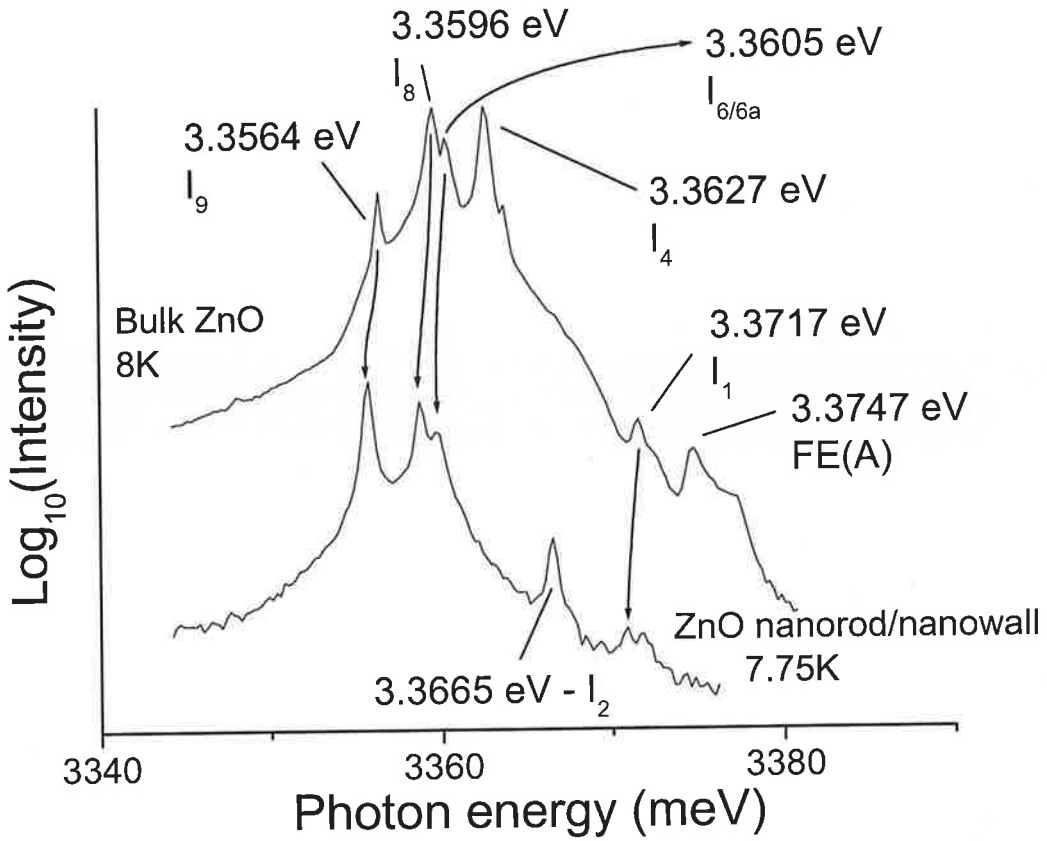

Figure 5.11 Pl data at low temperature of bulk ZnO material and ZnO nanorod/nanowall sample and line identification.

Our low temperature PL data for the nanorod/nanowall sample displays five clear peaks at energies of 3.3557 ± 0.0001 eV, 3.3588 ± 0.0001 eV, 3.3598 ± 0.0001 eV, 3.3665 ± 0.0001 eV and 3.3709 ± 0.0001 eV. A range of sharp peaks have previously been observed by a number of authors in studies on single crystal ZnO samples, and have been labelled I_0 to I_{11} [11], though the exact labeling is itself the subject of some controversy, and the microscopic chemical origins of the majority of the peaks is unknown. These peaks are associated with bound excitons at various defects in the ZnO crystal. The peaks in the nanorod/nanowall sample can be associated with peaks in bulk material, as indicated in Figure 5.11 and the fact that these lines all occur within one meV of the values measured for high quality bulk material (which are in agreement with literature values [11]) indicates that the nanostructures samples are not subject to a large strain. The three lower energy peaks at 3.3557 ± 0.0001 eV, 3.3588 ± 0.0001 eV and 3.3598 ± 0.0001 eV are most

probably the I_9, I_8 and $I_{6/6a}$ lines due to bound exciton recombination at neutral donor sites. The I_9 and I_8 lines have been attributed to In and Ga donors respectively by some authors [12, 13], while the origin of the $I_{6/6a}$ line remains unclear. The feature at 3.3709 ± 0.0001 eV is assigned to the I_1 feature based on its localization energy [11, 13]. We note that the lines in the nanorod/nanowall sample are shifted to lower photon energies by 0.8 meV in comparison with literature values for ZnO bulk material. We also note that there is no evidence of quantum confinement effects of the line energies for the nanorods of this diameter.

From our perspective, one of the most interesting features of the PL spectrum of the ZnO nanowalls/nanorods sample is the presence of the line at 3.3665 ± 0.0001 eV, substantially higher in energy than the main neutral donor bound exciton features. This feature is most likely the I_2 line. The chemical origin of this line is not clear, but the fact that it occurs at such high energy, indicates that it may not be due to a 'normal' donor bound exciton recombination. We note however that low temperature studies from the early 1990s [14, 15] have identified a high energy line at ~ 368.2 nm (3.3674 ± 0.0001 eV) as due to recombination of a 'surface' exciton in ZnO, which is observed in luminescence studies of a range of materials where ZnO crystallites with a high surface to volume ratio are formed. The surface to volume ratio of the nanorod/nanowall sample is much higher then the surface to volume ratio for bulk material. Our results favor this assignment, as the surface to volume ratio of the nanorod/nanowall sample is large.

We have also observed this feature in the well separated ZnO nanorod sample (Figure 5.12), and we can conclude that this feature is visible in both nanostructure materials where the surface to volume ratio is higher in comparison with the surface to volume ratio in bulk material where this feature is invisible (Figure 5.13).

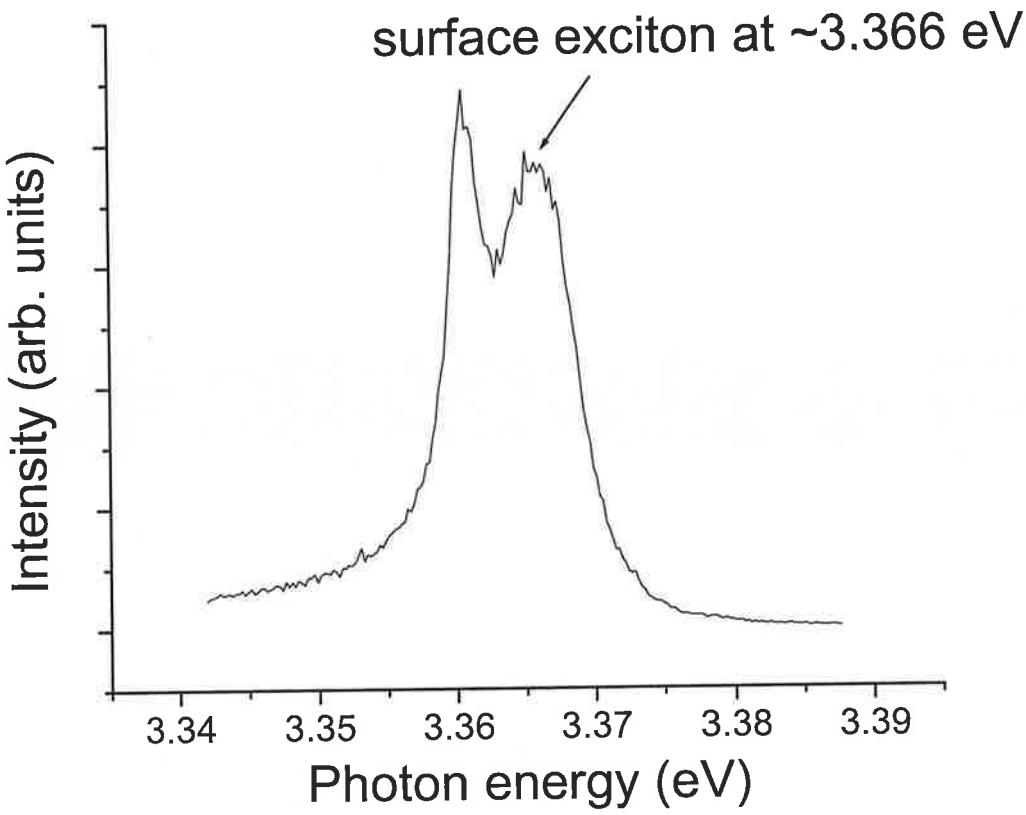

Figure 5.12 PL data at 7.5 K for well separated ZnO nanorod sample

We also note that the data in Figure 5.12 for the ZnO well separated nanorods show larger PL linewidths (~ 3.5 meV and 5.3 meV for the lower and higher photon energy features, respectively, based on fitting the spectrum with two Gaussian lineshapes) compared to the nanorods/nanowalls and bulk sample, which may be due to residual inhomogeneous strains, which are discussed below.

Figure 5.13 shows a comparison between low temperature PL spectra from bulk crystal material from two other suppliers (Cermet Inc. and Rubicon Technology) and Eagle-Picher bulk crystal material. We see no evidence for the surface exciton (SX) at 3.3665 ± 0.0001 eV in any of the bulk crystal samples.

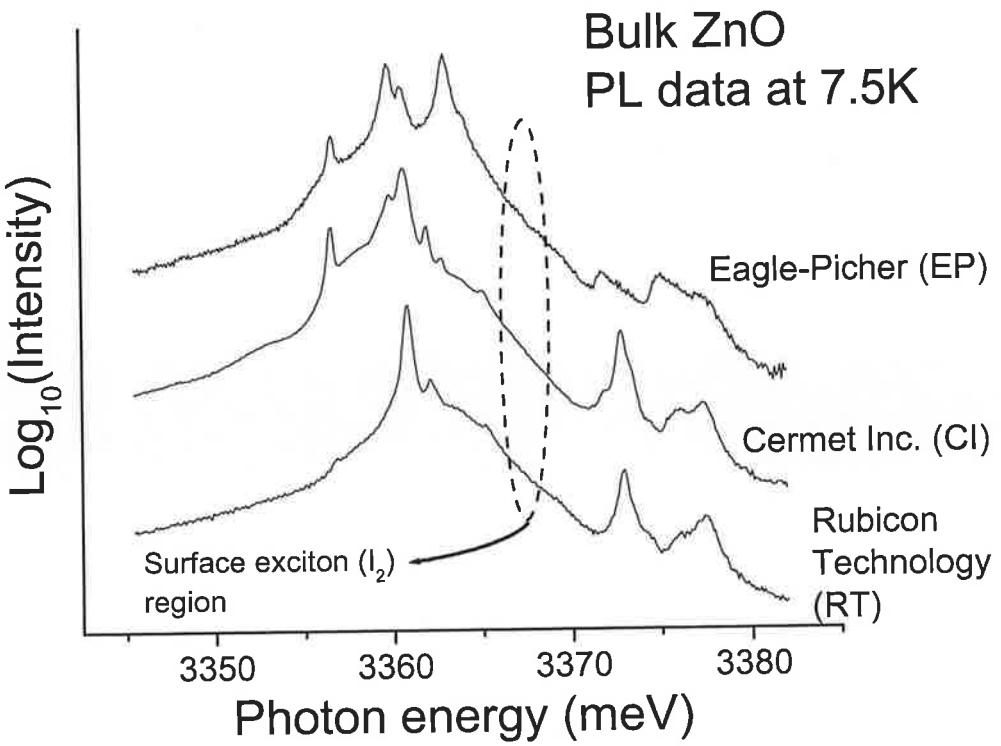

Figure 5.13 Comparison of low temperature PL (at 7.5 K) from two other sources of bulk single material ZnO; Rubicon Technologies (RT) and Cermet Inc. (CI), in addition to the EP sample.

Figure 5.14 shows the evolution of the PL spectra for the nanorod/nanowall sample as a function of temperature in the band edge region. We note that the surface exciton (SX) at ~ 3.366 ± 0.0001 eV disappears faster than the other lower energy bound exciton features and is gone at 20 K, while the luminescence from the other features survives to ~70 K and all these features appear to disappear at approximately the same rate. No other lines appear in a broader spectral range (3.300 - 3.440 eV) with increasing temperature, and specifically we do not see free exciton (FE) emission appearing.

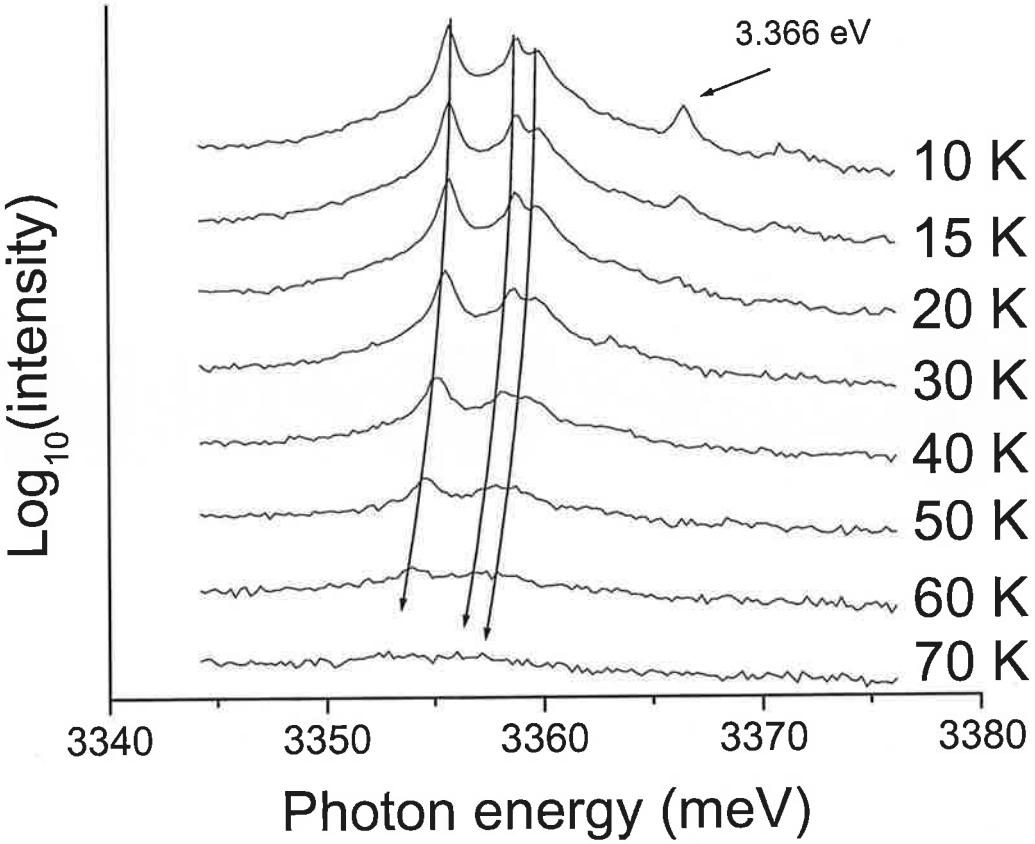

Figure 5.14 shows the evolution of the PL spectra for the nanorods/nanowall sample as a function of temperature in the band-edge region.

Figure 5.15 shows the evolution of the PL spectra for the well separated ZnO nanorod sample as a function of temperature in the band edge region. We note that the surface exciton at ~ 3.366 ± 0.0001 eV disappears relatively quickly (compared to the other I line emission at lower energy) with increasing temperature as was observed for the nanord/nanowall sample. Free exciton emission appears at higher temperatures, in contrast to the nanorod/nanowall sample, due to the thermally induced release of bound excitons from defects.

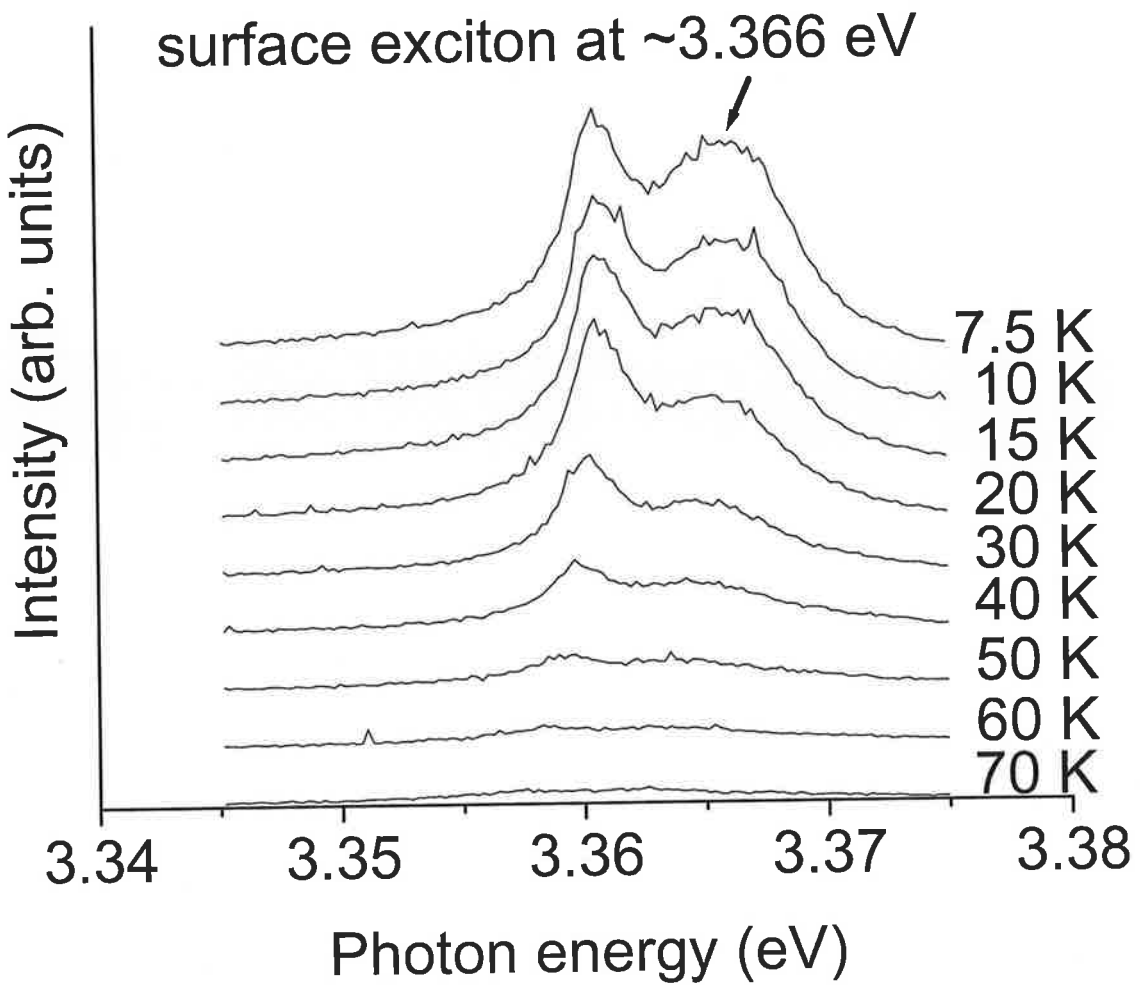

Figure 5.15 shows the evolution of the PL spectra for the well separated ZnO nanorod sample as a function of temperature in the band-edge region.

Figure 5.16 shows equivalent data for a commercial bulk single-crystal sample, where the bound exciton signals survive up to ~ 130 K and evidence is seen for the growth of the free exciton emission with increasing temperature as bound excitons are thermally released from defect centres.

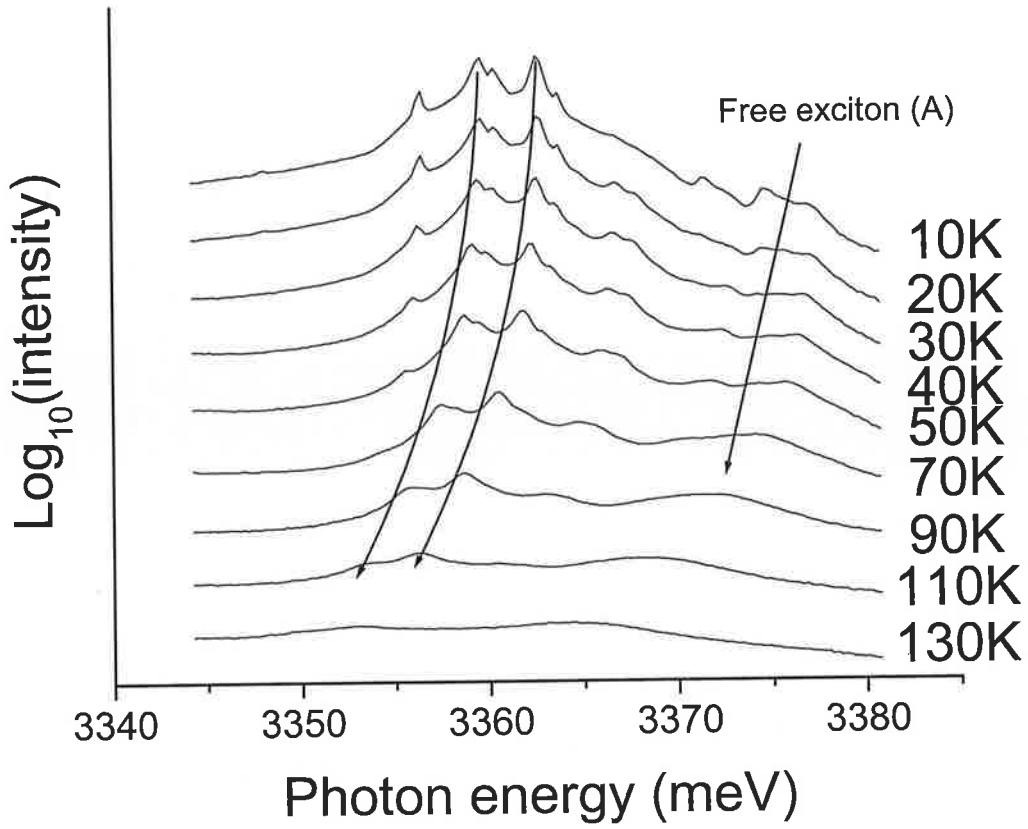

Figure 5.16 shows the evolution of the PL spectra for the EP bulk crystal as a function of temperature in the band-edge region.

While evidence for the surface exciton is seen in both the ZnO nanowall/nanorod sample and the well separated ZnO nanorod sample, consistent with the high surface to volume ratio in both compared to bulk material, the overall PL intensity in the nanowall/nanorod sample appears to quench far faster than in either the bulk material or the well-separated nanorod sample.

In Figure 5.17, we show the fits of the intensity versus temperature data to a temperature-activated exciton dissociation process (of the form in Equation 5.1 [16]) for (i) the integrated emission of the I_9, I_8 and $I_{6/6a}$ lines in the nanorod/nanowall sample, (ii) the surface exciton feature in the nanorod/nanowall sample, and (iii) the integrated intensity of the I_9, I_8 and $I_{6/6a}$, and I_4 lines in the bulk single-crystal sample.

$$I(T) = \frac{I(0)}{1 + GT^{\frac{3}{2}} \exp(-\frac{\Delta E}{kT})} \qquad (5.1)$$

I(T) describes the luminescence intensity as a function of temperature T, for a bound exciton, localised at a defect with localisation energy ΔE, being thermally delocalised into the band (with a band density of states $G.T^{3/2}$ [16]).

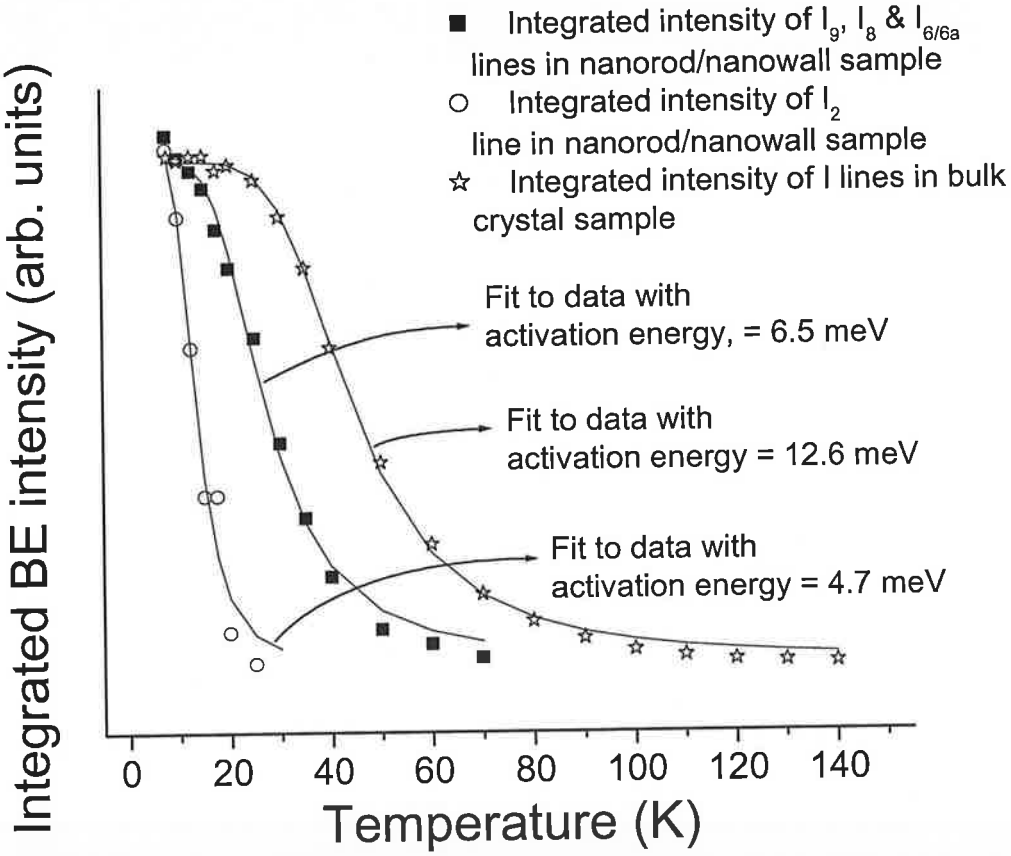

Figure 5.17 Evolution of PL spectra as a function of temperature for (a) the nanorod/nanowall sample and (b) the EP bulk crystal. (c) shows the fits (solid lines) to a temperature-activated process with activation energies displayed.

These fit well with activation energies ΔE of 6.5 ± 0.8 meV, 5 ± 1.5 meV, and 13 ± 0.6 meV, respectively. The value for the bulk sample is reasonably close to the average bound exciton localization energy for these features ~ 16 meV [11] and indicates a normal

thermally induced exciton dissociation. However, the activation energies for the nanorod/nanowall sample are significantly lower then any of the exciton localization energies, indicating a substantially different process is occurring. This is further evidenced by the growth for the bulk sample of free exciton (FX) emission which becomes prominent for temperatures above ~ 50 K (Figure 5.16) and the absence of any free exciton luminescence in the nanorod/nanowall sample with increasing temperature. We have not performed this analysis for the well separated nanorod sample as the larger linewidths commented upon above make accurate deconvolution of the contributions of the bound exciton (and free exciton at higher temperatures) and surface exciton features difficult.

Based on these data we propose that the nanowall interconnecting network in the nanowall/nanorod sample is of poorer crystal quality than the well separated ZnO nanorod sample. Because of larger footprint of the nanowall interconnections the strain energy in the ZnO will relax by creation of extended defects such as dislocations, as is customary in ZnO thin films on sapphire, but which is not seen in well separated nanorods whose footprint area is very low. This assignment is in agreement with our data, where we see broadened PL features in the well separated nanorod sample due to the incompletely relaxed residual strain in these samples (XRD data shown in chapter 4 confirms there is some residual strain in these samples which is not seen in the nanowall/nanorod sample). The poorer quality nanowall material may act as a source of non-radiative recombination for free excitons thermally released at higher temperatures and may also be responsible for the rapid decay of the luminescence with increasing temperature via a temperature-activated non-radiative recombination. Certainly these effects will limit the utilization of the excellent optical quality at low temperature in these systems for room temperature device structures.

One may further investigate the effect of this nonradiative recombination by studying the behavior of the full width at half maximum height (FWHM) of the I_9 peak (which can be observed in nanorod/nanowall sample and in bulk ZnO) as a function of temperature. This is shown in Figure 5.18. We observe that linear fits to these data give value of ~ 12 $\mu eV\ K^{-1}$ for the nanorod/nanowall sample and ~ 4 $\mu eV\ K^{-1}$ for the EP crystal. The FWHM in the nanorod/nanowall sample increases at a much higher rate then for bulk material which may

indicate presence of additional quenching mechanisms shortening the exciton lifetime, as proposed above.

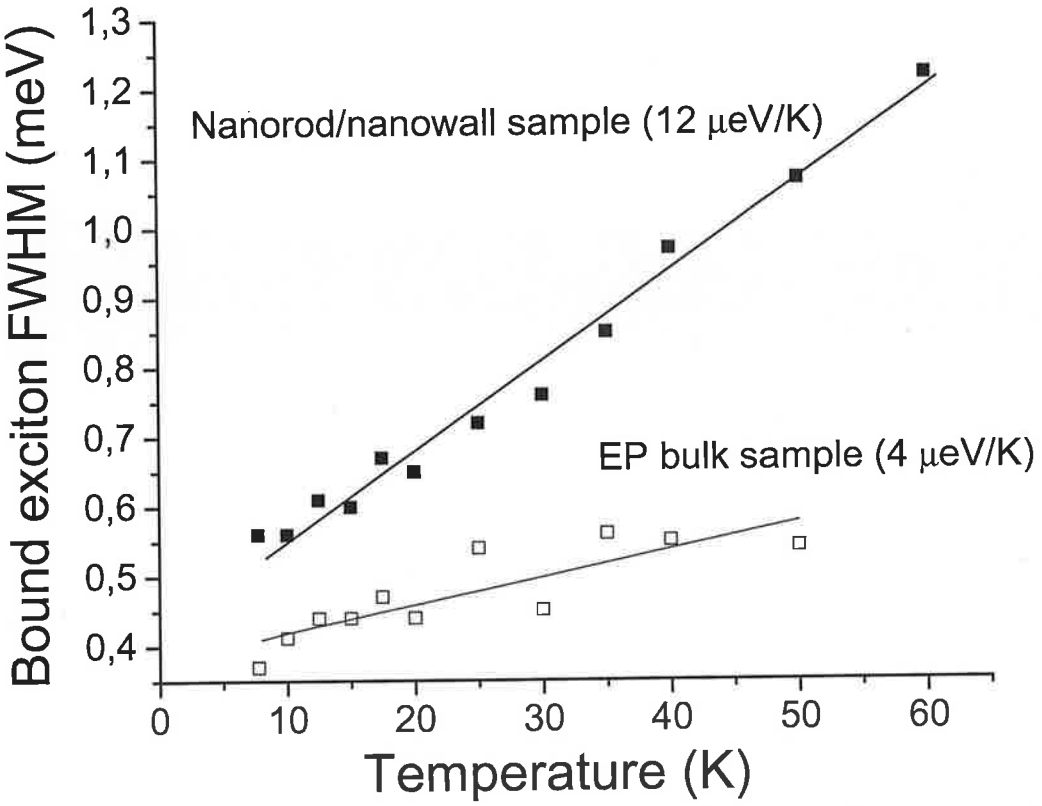

Figure 5.18 *The evolution of FWHM of the I_9 line in nanorod.nanowall sample and in the bulk material with temperature.*

5.3 Concluding Remarks

XRD and FESEM data on both well separated ZnO nanorod and nanowall/nanorod ZnO samples show well aligned nanostructures with the *c* axis normal to the substrate, with a very low rocking curve halfwidths. The well separated ZnO nanorods show some residual strain effects which are not seen in the nanowall/nanorod samples, which we attribute to strain relaxation in the nanowall interconnecting material by formation of extended crystal defects. PL data show that the optical quality of the nanorod/nanowall sample (where the surface to volume ratio is very high) is excellent at low temperatures in comparison with both well separated ZnO nanorod samples and bulk material. We observe a high energy

excitonic emission close to the band edge in the nanostructured ZnO samples which we assign to the surface exciton in ZnO at ~ 3.3665 ± 0.0001 eV, consistent with the large surface to volume ratio of the nanostructures. Temperature dependence measurement of the PL shows a temperature–activated nonradiative recombination in the nanorod/nanowall structures not seen in bulk material. Extended defects in the nanowall interconnecting network are proposed to be responsible for the rapid decay of the PL with increasing temperature in these samples, consistent with the XRD data referred to above. These observations lead us to conclude that in the systems we have grown, the large footprint of the nanorod/nanowall sample leads to strain relaxation and defect creation not seen for well-separated nanorods which then detrimentally affects the optical properties of the system, and the excellent low temperature optical emission from these samples are not apparent at room temperature. While the nanowall/nanorods nanostructures offer the prospect of technological applications whereby the nanowall network may allow a convenient electrical back contact on the insulating sapphire, which would be important in applications such as field emission where the well-aligned nanorod morphology would be quite promising, control of the non-radiative recombination effects due to the inferior material quality of the nanowalls via passivation or other means will be an important task in order to realize devices with optimum properties at room temperature.

5.4 References

[1] H. T. Ng, J. Li, M. K. Smith, P. Nguyen, A. Cassell, J. Han, and M. Meyyappan, *Science* **300** (2003) 1249

[2] J. Y. Lao, J. Y. Huang, D. Z. Wang, Z. F. Ren, D. Steeves, B. Kimball, and W. Porter, *Applied Physics A: Material Science Progress*. **78** (2004) 539

[3] B. P. Zhang, N. T. Binh, Y. Segawa, Y. Kashiwaba, and K. Haga, *Applied Physics Letters* **84** (2004) 586

[4] B. P. Zhang, N. T. Binh, Y. Segawa, K. Wakatsuki, and N. Usami, *Applied Physics Letters* **83** (2003) 1635

[5] W. I. Park, D. H. Kim, S.-W. Jung, and G. C. Yi, *Applied Physics Letters* **80** (2002) 4232

[6] I. Shalish, H. Temkin, and V. Narayanamurti, *Physical Review B* **69** (2004) 245401

[7] S. Hong, T. Joo, W. I. Park, Y. H. Jun, and G. C. Yi, *Applied Physics Letters* **83** (2003) 4157

[8] M. Lorenz, J. Lenzner, E. M. Kaidashev, H. Hochmuth, and M. Grundmann, *Annalen der Physik* **13** (2004) 39

[9] R. Dingle, *Physical Review Letters* **23** (1969) 579

[10] K. Vanheusden, W. L. Warren, C. H. Seager, D. R. Tallant, J. A. Voight, and B. E. Gnade, *Journal of Applied Physics* **79** (1996) 7983

[11] B. K. Meyer, H. Alves, D. M. Hofmann, W. Kriegseis, D. Forster, F. Bertram, J. Christen, A. Hoffmann, M. Strasburg, M. Dworzak, U. Haboeck, A. V. Rodina, *Phys. Status Soidi (B)* **241** (2004) 231

[12] S. Muller, D. Stichtenoth, M. Uhrmacher, H. Hofsass, C. Ronning, J. Roder, *Applied Physics Letters* **90** (2007) 012107

[13] K. Johnston, M. O. Henry, D. McCabe, E. McGlynn, M. Dietrich, E. Alves, M. Xia, *Physical Review B* **73** (2006) 165212

[14] V. V. Travnikov, A. Freiberg, and S. F. Savikhin, *Journal of Luminescence* **47** (1990) 107

[15] S. F. Savikhin and A. Freiberg, *Journal of Luminescence* **55** (1993) 1

[16] J. S. Blakemore, book *Semiconductor statistics* 1927-, Dover phoenix editions, Mineola, NY : Dover Publications, 1987

6 Self-Organized Zinc Aluminate ($ZnAl_2O_4$) on *c*-Sapphire

In this chapter our studies of the growth of epitaxially ordered zinc aluminate domains are presented. These domains, with sub-micron dimensions, are formed at atmospheric pressure on c-sapphire substrates without any catalyst, using a vapour phase transport method at various temperatures and growth durations. This observation initially came about as a by-product of the previously described studies on ZnO nanorod growth. The structures observed were quite unusual in appearance and the topic was pursued to identify the origin of the morphology in more detail.

The size of the grains can be controlled by varying process parameters such as growth temperature and deposition time, 950 °C – 1125 °C and 30 - 60 minutes respectively. A zinc aluminate ($ZnAl_2O_4$) layer is formed by reaction of the source materials (Zn and O) with the substrate. We observe crystallites or grains with a well-defined epitaxial relationship on the c-plane sapphire substrate. The epitaxially oriented deposit, displays the form of characteristically twinned grains with sub-micron dimensions with three variants, consistent with the c-sapphire substrate symmetry. FESEM and TEM studies show that the formation of these grains is associated with the presence of extended defects in the sapphire substrate. We have explored this link by a number of methods including stressing pre-annealed good quality c-sapphire substrates to their mechanical fracture point and also by various etching and laser ablation methods. These studies confirm that these structures can be grown only on c-sapphire substrates with high defect content. Epitaxially ordered grains formed at higher temperatures show a change in the nature of the twin boundaries and epitaxial relations as a function of growth time, attributed to the effects of annealing during growth. The aluminate microstructures formed also show a number of interesting features, including better diffusional transport along the lower density "open" twin boundary, a noticeably symmetrical appearance in FESEM images and a contrast mechanism in SEM images which is attributed to electron channelling along the twin boundaries in the grain. The change in the nature of the twin boundary with annealing, mentioned above, leads to the altered SEM images for annealed samples.

6.1 Experimental Procedure

Zinc aluminate was grown on *c*-sapphire substrates by VPT. Most of the substrates used were obtained from Testbourne [1], although substrates from other suppliers were also used. The substrates are ultrasonically cleaned before growth and are generally bare, though in some cases they have been patterned with gold to catalyse the formation of wurtzite phase ZnO nanorods by the VLS mechanism, (using otherwise similar growth conditions) for purposes of comparison [2]. The general growth conditions are as described in chapter 3. The nominal temperature of the furnace is set in the range 950 °C - 1125 °C and the set temperature is achieved in ~ 15 - 20 minutes. The actual substrate temperature is 35 °C lower than the nominal temperature for growth at 950 °C and 50 °C lower for growth at 1125 °C, due to the temperature gradient of the furnace. The absence of any Au catalyst particles on the substrate surface indicates that the VLS mechanism is not responsible for the growth products and we believe that ZnO is nucleated on the bare *c*-sapphire surface by VS deposition, and that this ZnO layer may react with the substrate to form a spinel zinc aluminate, according to the formula:

$$ZnO + Al_2O_3 \rightarrow ZnAl_2O_4$$

to form zinc aluminate.

6.2 $ZnAl_2O_4$ Characterisation

This section describes the characterisation of zinc aluminate microstructures and is divided into two sub-sections, based on the growth durations (6.2.1 describes growth for 30 minutes duration, 6.2.2 describes 60 minute duration growth).

6.2.1 -30 Minutes Growth Duration

The typical SEM/FESEM images of sample grown for 30 minutes at a furnace temperature of 950 °C and a substrate temperature of 915 °C and the sample grown for 30 minutes at a furnace temperature of 1125 °C and a substrate temperature of 1075 °C is shown in Figures 6.1(a), (b)) Figure 6.1(c), (d) respectively.

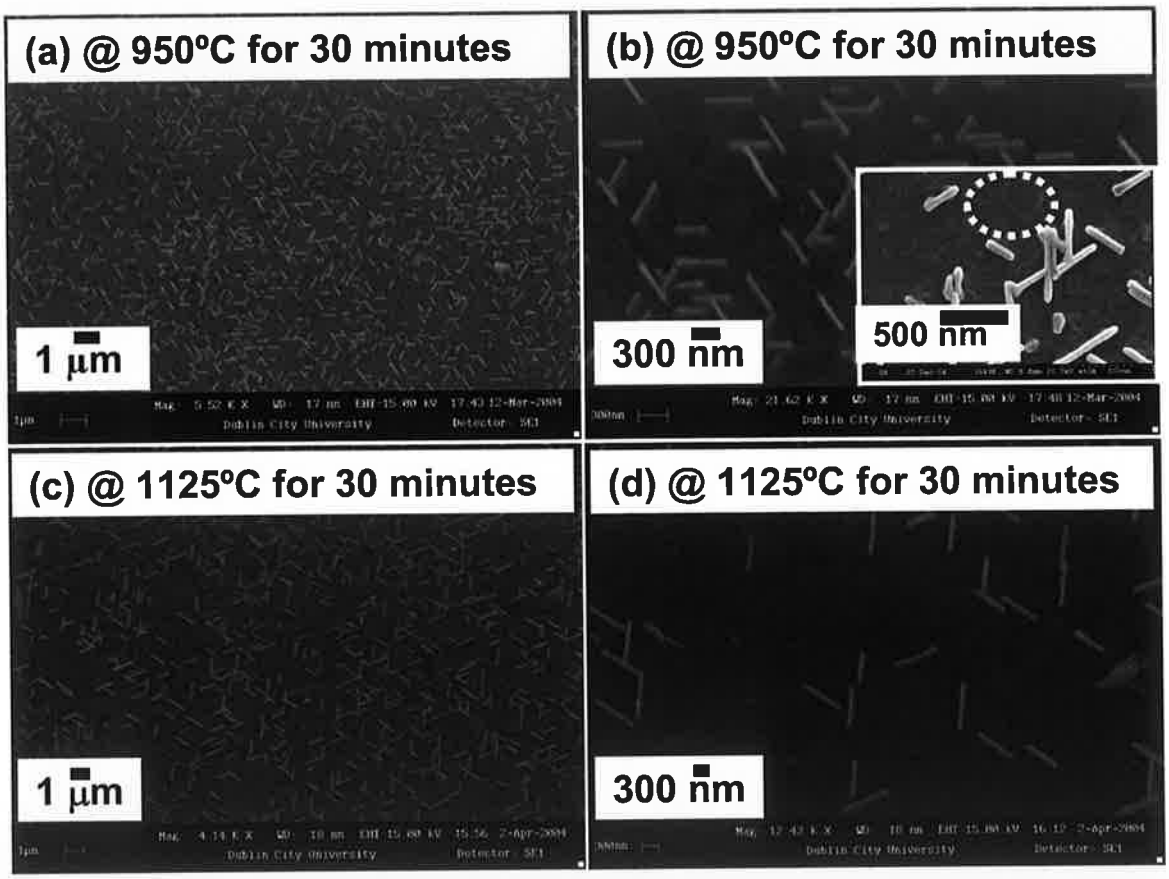

Figure 6.1 SEM / FESEM images of samples grown on c-sapphire; (a) growth temperature 950 °C (growth duration 30 minutes); (b) higher magnification of sample in (a), inset shows FESEM image at higher magnification; (c) growth temperature 1125 °C (growth duration 30 minutes).

Prominent structures with a linear appearance are seen with a high secondary electron contrast, aligned in three specific in-plane directions with an angle of 120 ° between them. These structures are uniformly distributed among these directions. The width of the linear

high intensity region in all cases is ~ 70 nm and the length of this region is distributed in the range 400 - 600 nm for samples grown at 950 °C, and in the range 700 - 800 nm for samples grown at 1125 °C, though shorter and longer examples are seen in both cases. We have performed AFM to study the surface topography, shown in Figure 6.2 for a sample grown at ~ 1125 °C for 30 minutes.

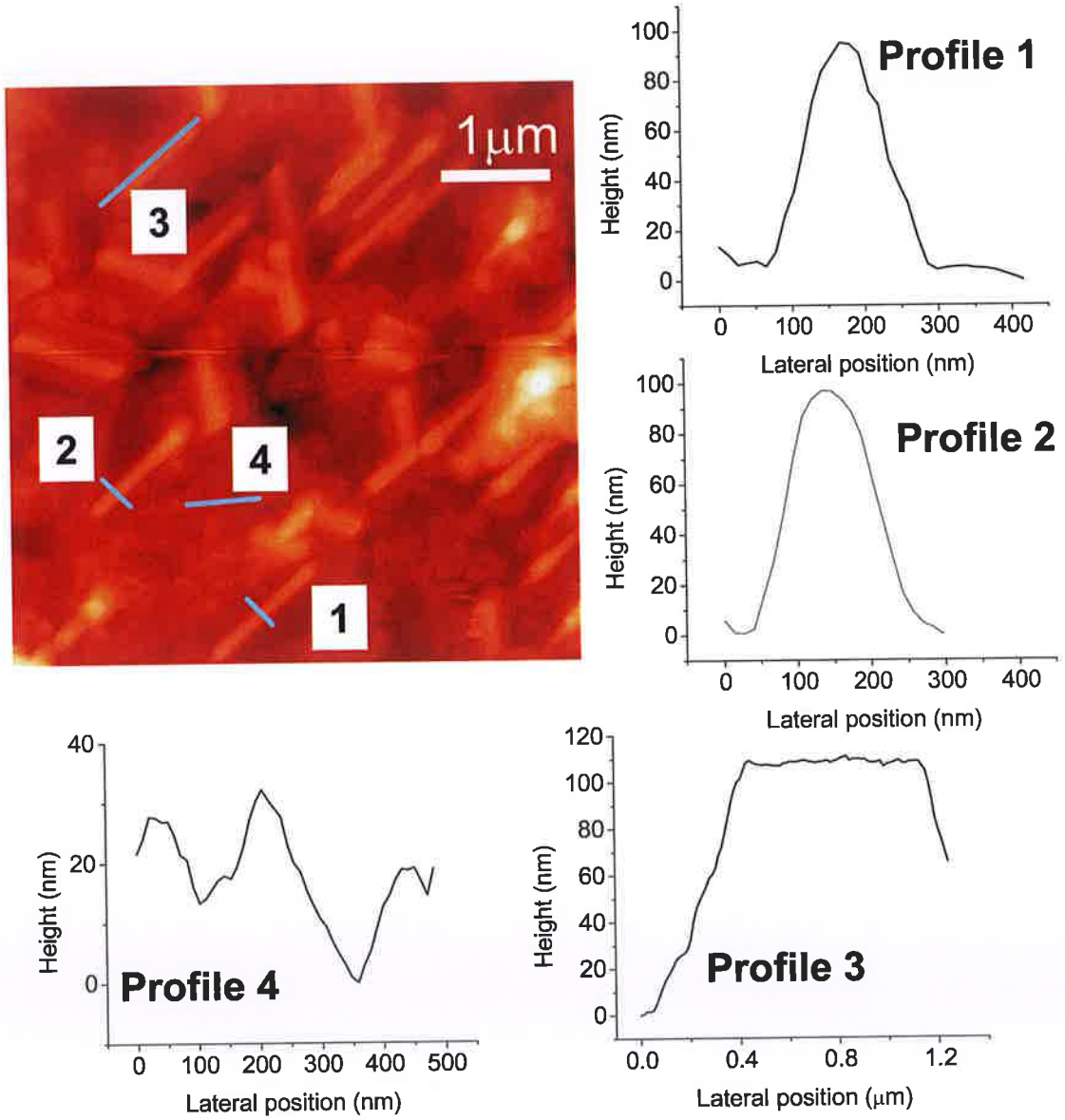

Figure 6.2 AFM data on sample grown at ~ 1125 °C shown in Figure 6.1(c) with height profiles at various positions on the surface, as discussed in the text.

Three-fold symmetric structures, similar to those observed in SEM/FESEM, are again clearly visible, although the contrast is reduced compared to the SEM/FESEM data and evidence of structure in the surrounding region is also visible. The longitudinal and crosswise height profiles are displayed from various regions of the AFM image. These show that the structures have the form of cylindrical bumps with an average height of ~ 90 -100 nm, and that the width of the structures (at their base) deduced from these profiles are quite broad ~ 200 nm. This is substantially greater than the width of the bright linear regions seen SEM/FESEM, and the difference is much greater than can be explained by tip broadening effects in the AFM. Thus the bright linear structures seen in the SEM/FESEM images are not only due to contrast effects due to surface topography. The physical structures responsible for the bright SEM features are quite a bit broader than the width of the bright lines seen in SEM images. Height profiles across regions of the sample where no symmetric structures are visible (profile 4 in Figure 6.2) show a substantial degree of roughness, indicating that layer deposition has taken place in this region also. Evidence of this deposition from SEM/FESEM data is also shown in the circled region in the inset of Figure 6.1(b) above.

The symmetric distribution of these microstructures with a three-fold symmetry suggests both the possibility of an epitaxial relationship to the hexagonal sapphire *c*-plane substrate (at least for the material close to these symmetric structures) and a possible alignment of the long axis of the structures seen in SEM along high symmetry in-plane sapphire directions. We have therefore studied Laue patterns of the *c*-plane sapphire substrate as shown in Figure 6.3(a) to study the crystallographic orientation of the zinc aluminate microstructures in relation to the *c*-plane sapphire surfaces (Laue pattern data supplied by Dr. Lisa O'Reilly & Prof. Pat McNally, RINCE, DCU). When the orientation of the sapphire substrate is known from Laue data then the orientation of these microstructures may be established from SEM/FESEM data at various magnifications by comparison with the physical edges of samples, as shown in Figure 6.3(b). The Laue measurements have been confirmed by subsequent x-ray phi scans of the sapphire substrates. We find that the long direction of the bright symmetric structures seen in SEM lie parallel to the <10-10> sapphire in-plane directions (Figure 6.3(c) in all cases studied, (for all growth temperatures

and durations). This alignment along a high symmetry in-plane sapphire direction further suggests that at least the portion of the deposit associated with these microstructures grows with an epitaxial relationship to the substrate.

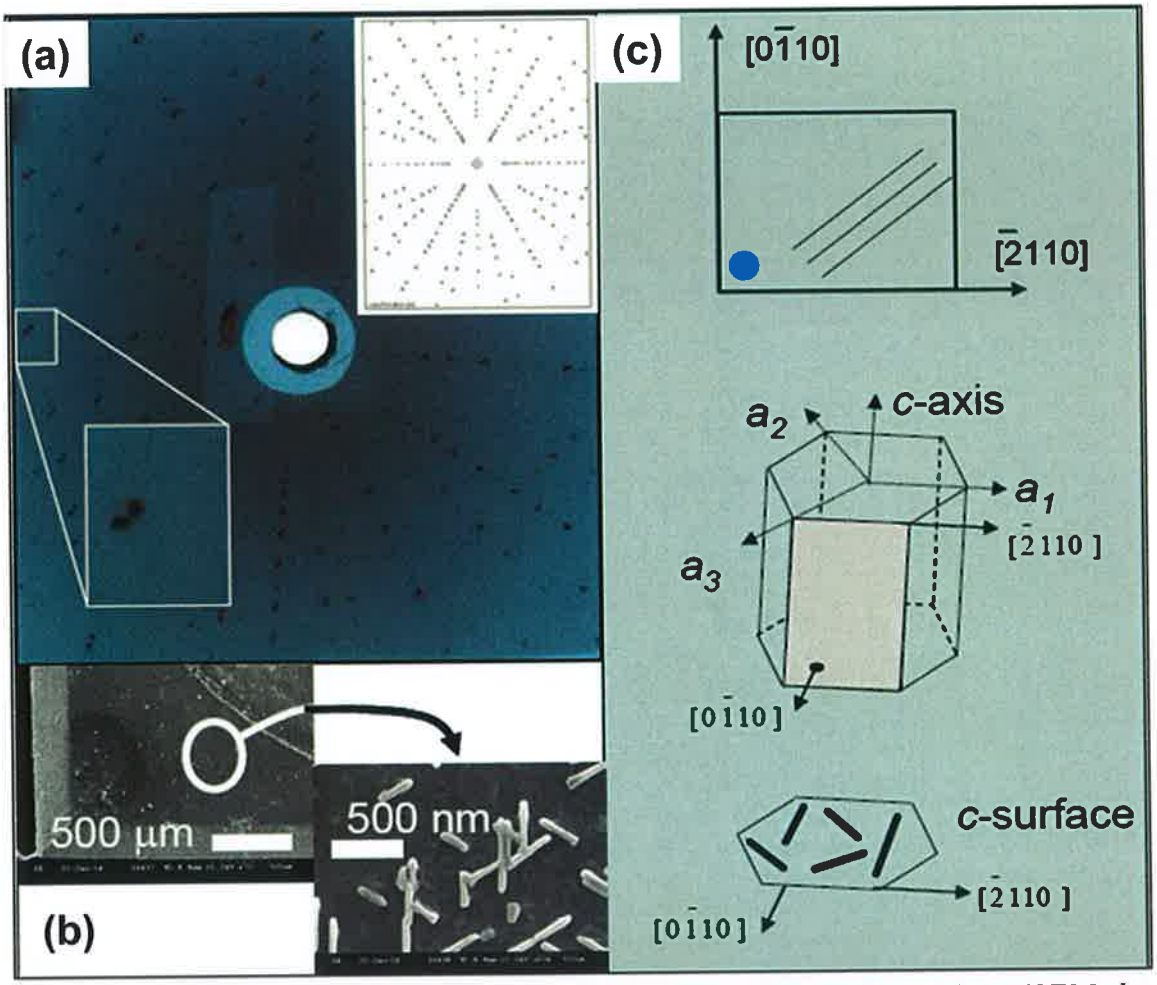

Figure 6.3 Experimental and simulated Laue pattern of c-sapphire (a); FESEM data showing orientation of zinc aluminate microstructures with respect to sample edges (b); Physical orientation of microstructures on substrates as determined from the Laue pattern.

TEM measurements have been performed in both cross-section and plan-view mode (in a collaboration with Dr. Simon Newcomb of Glebe Scientific Ltd., Ireland who actually prepared the samples and made the TEM measurements, see [3] for TEM sample preparation details). In addition, EDX, CL and Raman spectroscopy measurements have

been made in order to determine the material phase and chemical composition and to clarify the origin of the microstructures seen in SEM and AFM. Figure 6.4 shows cross-sectional TEM data for a sample grown at 950 °C for 30 minutes (the sample shown in Figure 6.1(a) above). Figure 6.4 shows a broad area at relatively low magnification which is a montage of two bright field micrographs.

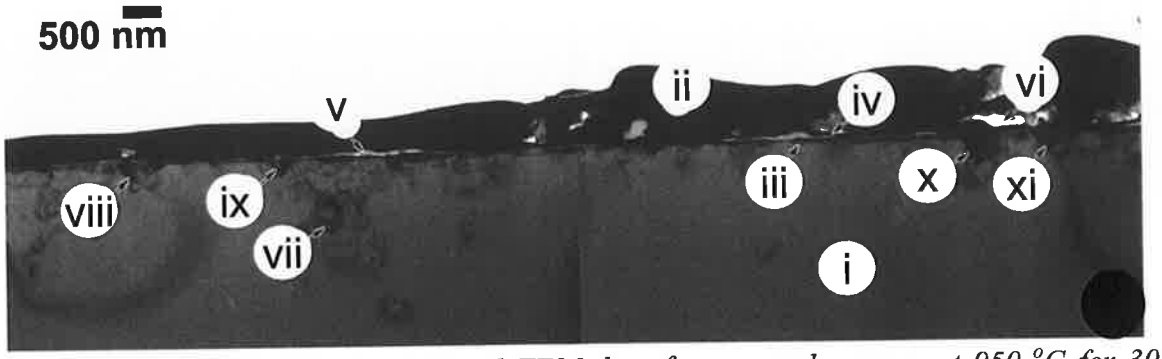

Figure 6.4 Bright field cross-sectional TEM data for a sample grown at 950 °C for 30 minutes, at low magnification.

A distinction can be made between the substrate material at (i) and the Pt-based coating at (ii), deposited onto the surface of the sample prior to ion beam thinning. One can also distinguish a thin surface layer marked at (iii) which was capped by a thick layer of Au (at (iv)) used to prevent any 'top down' ion damage of the sample before deposition of the Pt. There are a number of regions located at the base of the Au where 'pockets' of low atomic number debris from the TEM sample preparation are seen (as at (v)) and also some large holes of the type marked at (vi). The defect density of the near surface regions of the *c*-plane sapphire is characteristically high (as indicated at (vii)) and that the surface layer marked at (iii) exhibits significant variations in thickness. This aspect is shown by the presence of clearly observable features marked as (viii)-(xi) where the film thickness is much higher than elsewhere.

A cross sectional image at higher magnification on one of these high thickness deposition regions is shown in Figure 6.5 for a sample grown at 950 °C for 30 minutes. Figure 6.5 shows that the high thickness region consists of a grain surrounded by a thinner and randomly oriented regions, and the edges of the grain are indicated by the high angle grain

boundaries at (ii) and (iii) in Figure 6.5. The defect density of the material is significantly higher outside the course grain then within it. The grain shows a clear planar boundary at (iv).

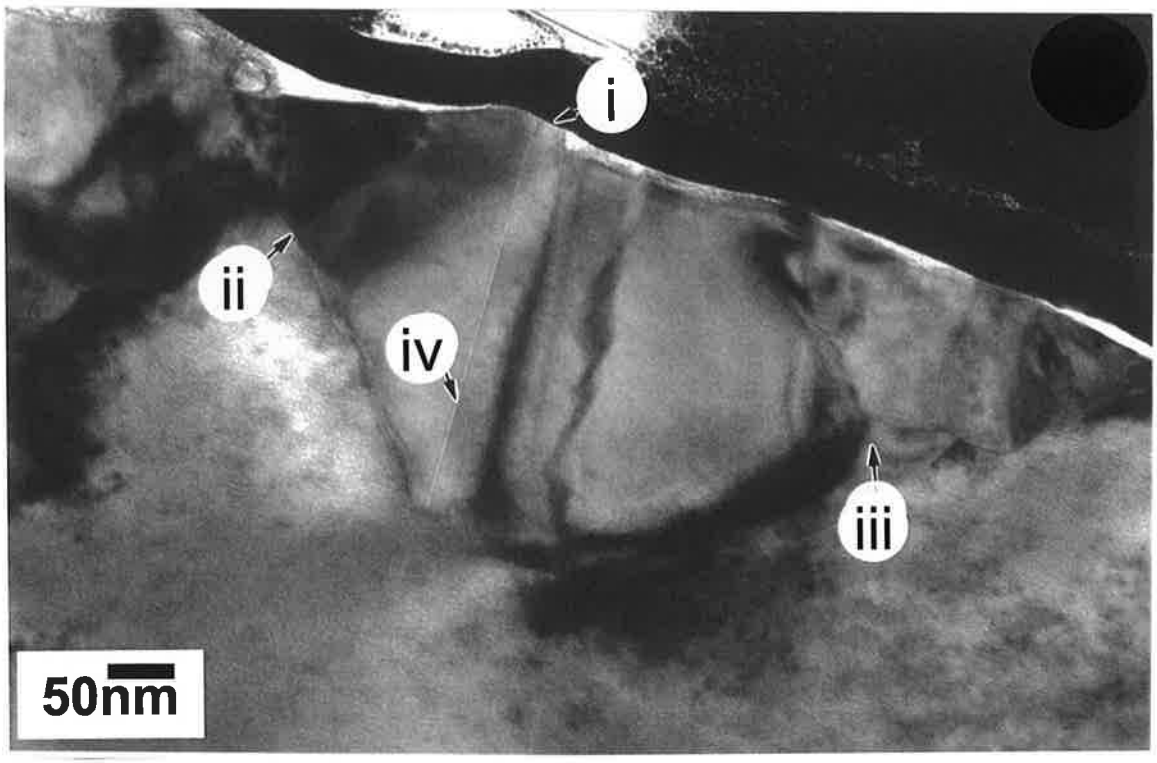

Figure 6.5 Cross sectional TEM image at high magnification on high thickness region.

The chemical composition of the deposit was studied by EDX, CL and Raman spectroscopy. EDX data is shown for a sample grown for 30 minutes at 950 °C (imaged in Figure 6.1(a)) in Figure 6.6. This indicates that the chemical composition of the deposit has contributions from Zn, Al, O and C as expected given the source and substrate material composition. Carbon (C) is detected because graphite and ZnO have been used as the source material. The strong Li peak is due to the detector used for EDX. However the EDX data are due to contributions from region many microns deep and the chemical phase of the growth layer cannot be accurately determined in this way. XRD data (Figure 6.7) display a number of peaks associated with the cubic spinel zinc aluminate phase, in addition to the

sapphire substrate, but no indication of ZnO or other Zn-Al-O phases, providing the first strong indications that the deposited layer is zinc aluminate.

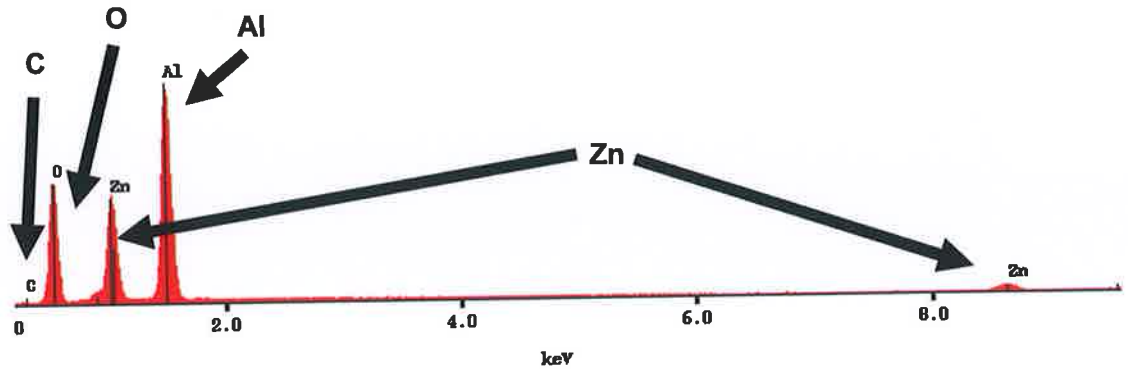

Figure 6.6 EDX spectrum of zinc aluminate layer.

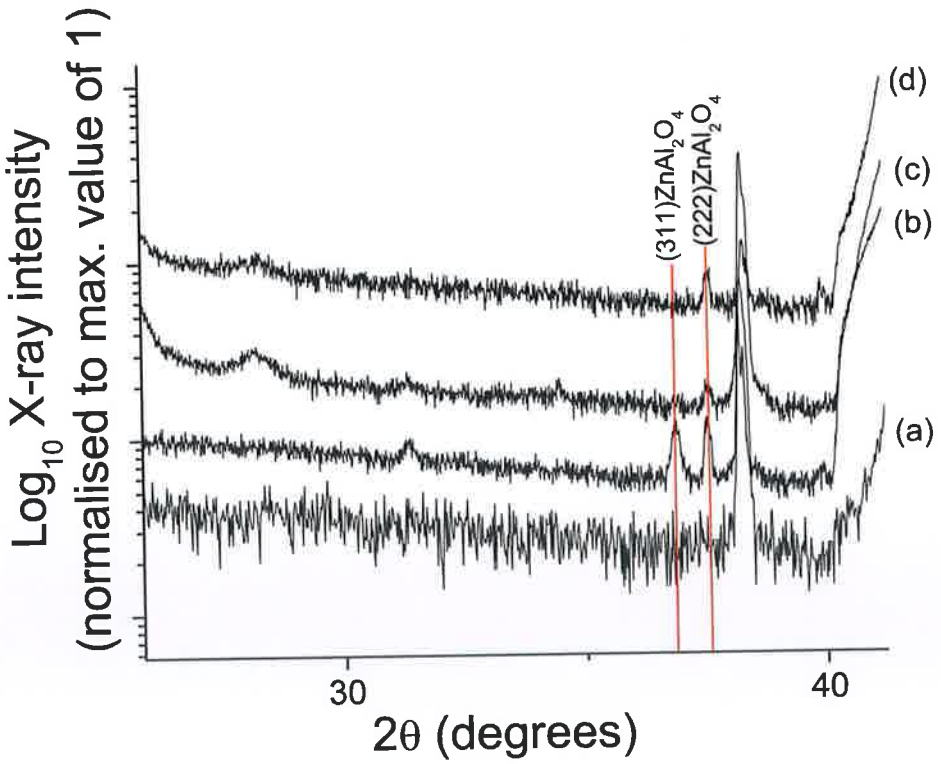

Figure 6.7 XRD data display a number of peaks associated with the cubic spinel zinc aluminate phase. We can see that the (111) ZnAl2O4 at 37.54 peak is presented in all samples ecept the bare c-sapphire; (a) bare c-sapphire, (b) sample grown at 1125°C for 30 mins, (c) sample grown at 1125°C for 60 mins, (d) sample grown at 1125°C for 30 mins on preannealed substrate.

CL and Raman data show no evidence of ZnO phase material, consistent with the indications above, though the deposited zinc aluminate layer is too thin for clear spectral signatures of this phase to be observed. These tentative assignments have been confirmed by selected area electron diffraction (SAED) measurements, as shown in Figure 6.8 below.

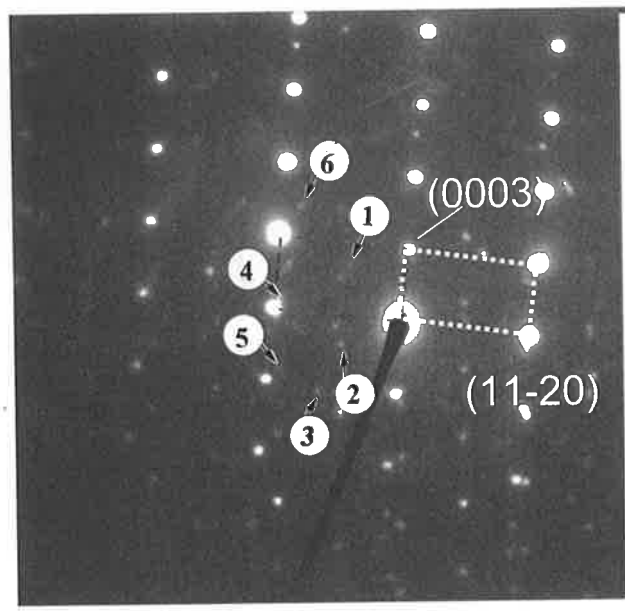

Ring No.	d-Spacing, nm	$ZnAl_2O_4$ d, nm	hkl
1	0.4688	0.4670	111
2	0.4061	0.4042	200
3	0.2872	0.2861	220
4	0.2455	0.2438	311
5	0.2348	0.2335	222
6	0.2040	0.2021	400

Figure 6.8 SAED pattern from lower thickness regions of the deposited layer ([10-10] sapphire zone normal, with sapphire reflections indexed, as indicated by dashed lines).

The SAED pattern shown above is from one of the lower thickness regions (e.g. between (viii) and (ix) in Figure 6.4) of the deposit where the sapphire substrate is at a [10-10] zone normal. The d-spacings for the diffraction rings marked at 1 - 6 are given in the table in the inset and a comparison can be made with the cubic $ZnAl_2O_4$ phase which has a lattice parameter of 0.80848 nm [4]. The diffraction pattern clearly demonstrates the formation of zinc aluminate, and we have carefully ruled out the possibility of the layer being associated with other zinc-related oxides, such as cubic and hexagonal ZnO phases as well as two cubic ZnO_2 phases. Thus the assignment to zinc aluminate is unambiguous. It is interesting to find such an angular spread in the diffraction spots. This pattern was taken from a reasonably small area of the aluminate but we are seeing polycrystalline growth with no epitaxial relationship to the substrate in this part of the deposit.

The coarse, or larger, grains are also zinc aluminate phase material. An SAED pattern of the region in Figure 6.5 above is shown in Figure 6.9. The spots in the SAED pattern in Figure 6.9 are all indexed either to zinc aluminate ((1-11, (200) & (11-1)) or sapphire ((-12-10) & (0003)) reflections. The SAED pattern also clearly shows twinning in this large grain, with the two twin components indicated by the dotted and dashed lines. The common twin plane is seen to be an aluminate (111) plane. We associate this twin boundary with the planar boundary referred to at position (iv) in Figure 6.5.

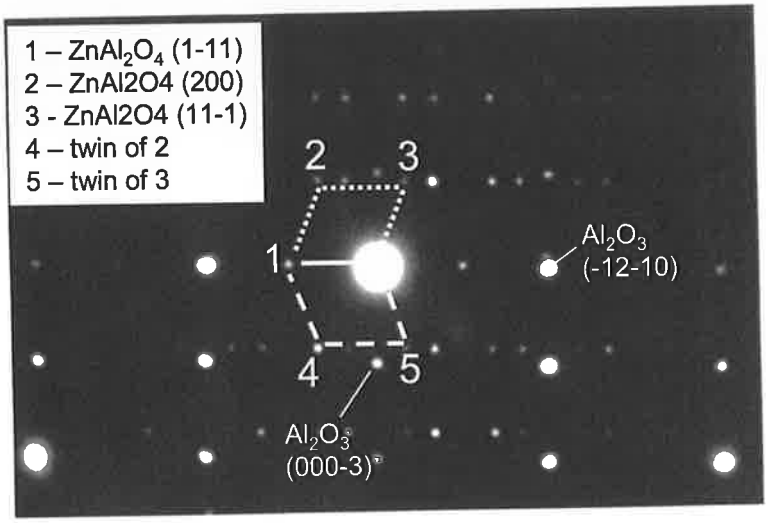

Figure 6.9 SAED pattern of region in Figure 6.5, with reflections of aluminate twins indexed at a sapphire [10-10] zone normal and an aluminate [011] zone normal.

The SAED data enable us to confirm that the coarse grains have a well-defined epitaxial relationship to substrate and to deduce that this relationship is:

$$[10\text{-}10]\ Al_2O_3\ //\ [011]\ ZnAl_2O_4 \text{ and } (0001)\ Al_2O_3\ //\ (\text{-}2\text{-}11)\ ZnAl_2O_4$$

This epitaxial and twinning relationship indicates that the intersection of the twin boundary of the aluminate grain with the surface is a line parallel to the sapphire [10-10] in-plane direction, i.e. exactly parallel to the long direction of the bright symmetric structures deduced from Laue and x-ray measurements. Thus we identify these large, twinned, zinc aluminate grains with the bright symmetric structures seen in SEM, and specifically we

identify the bright central line region seen in SEM with the twin boundary region seen in TEM. This identification is supported by the general topography of the grain structure. Much of the grain structure lies under the surface of the surface substrate and the surface topography of the grain shown in Figure 6.5 appears entirely consistent with AFM data presented earlier, in terms of height, width and the surface roughness of surrounding regions.

Multiple twinning in a single grain is also seen in a number of grains examined for a sample grown at 950 °C for 30 minutes, as shown in Figure 6.10, and is confirmed by the [011] $ZnAl_2O_4$ SAED pattern shown in Figure 6.10(b). The observation of multiply twinned grains with twin boundaries closely spaced parallel to each other is entirely consistent with SEM observations of side by side, parallel bright microstructures shown in the inset of Figure 6.1(b), and also shown in the inset of Figure 6.10(a) and specifically consistent with the identification of the bright central line region seen in SEM with the twin boundary region seen in TEM.

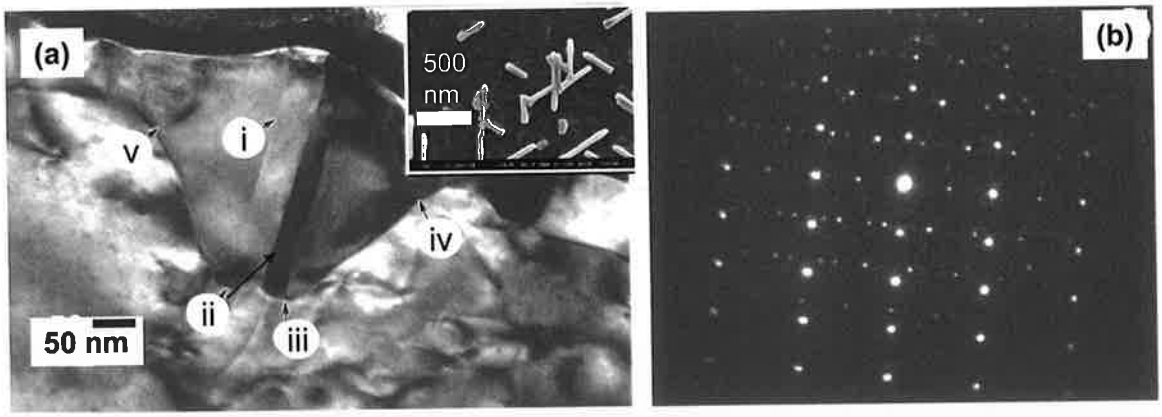

Figure 6.10 (a) Bright field cross-sectional TEM image on high thickness multiply twinned region (edges of region marked at (iv) & (v), twins at (i), (ii) & (iii)). Inset shows a FE-SEM image of the same sample; (b) SAED pattern of region in A at a sapphire [10-10] zone normal and an aluminate [011] zone normal showing twinned spots.

Plan view TEM data for a sample grown at 950 °C for 30 minutes are shown in Figure 6.11(a), where the plan view slice extends between positions at depths of ~ 140 and 250 nm below the surface, i.e. below the thin zinc aluminate layer depth, intercepting only the

thicker grains and sapphire substrate. Characteristically six sided zinc aluminate grains are seen in the sapphire matrix, each of which contains the type of twin boundary marked at (i), (ii) etc. Extended defects in the sapphire are also clearly visible around the grains. There are three grain variants for the aluminate, as typified by those marked at (ii), (iii) and (iv), making angles of 120 ° to each other. These data are interpreted as a top-view of the grains discussed above, and the twin boundaries are again seen in all cases, sometimes with multiply-twinned grains. SAED patterns are shown in Figure 6.11(b) one taken on each grain variant. These are taken at [-2-11] zone normals for the $ZnAl_2O_4$ phase, the interface marked at e.g. (i) in Figure 6.11(a) thus being a (111)-type boundary. Figure 6.11(c) was taken from a localised region of the sapphire that contained none of the aluminate grains and shows a [0001] Al_2O_3 zone normal. Figure 6.11(d) shows a combination of the substrate and the three grain variants of the oxide with a wide aperture, with the contribution of each variant indicated. These data are all consistent with the previously deduced epitaxial and twin relationships, and confirm our identification of the twin boundary as the origin of the bright central line region seen in SEM.

TEM measurements on samples grown at 1125 °C for 30 minutes show similar results to those on samples grown at 950 °C for 30 minutes, consistent with their similar appearances in SEM images.

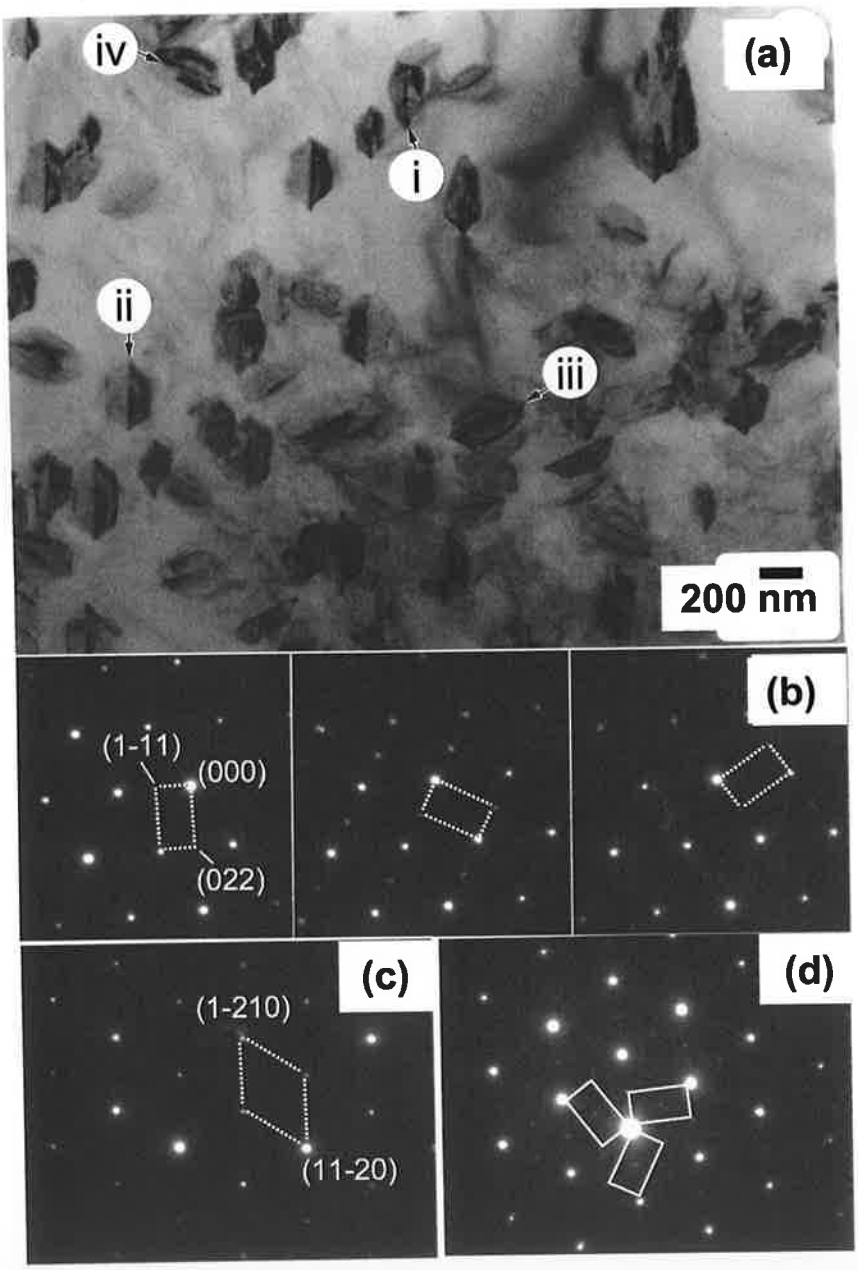

Figure 6.11 *(a) Bright field plan view TEM data for a sample grown at 950 °C for 30 minutes; (b) SAED patterns on each grain variant at an aluminate [-2-11] zone normal; (c) SAED patterns on sapphire at an [0001] Al_2O_3 zone normal; (d) wide aperture SAED pattern which is a combination of the substrate and the three grain variants of the oxide.*

6.2.2 -60 Minutes Growth Duration

The typical FESEM images of sample grown for 60 minutes at a furnace temperature of 1125 °C and a substrate temperature of 1075 °C is shown in Figures 6.12(a), and 6.12(b) at higher magnification.

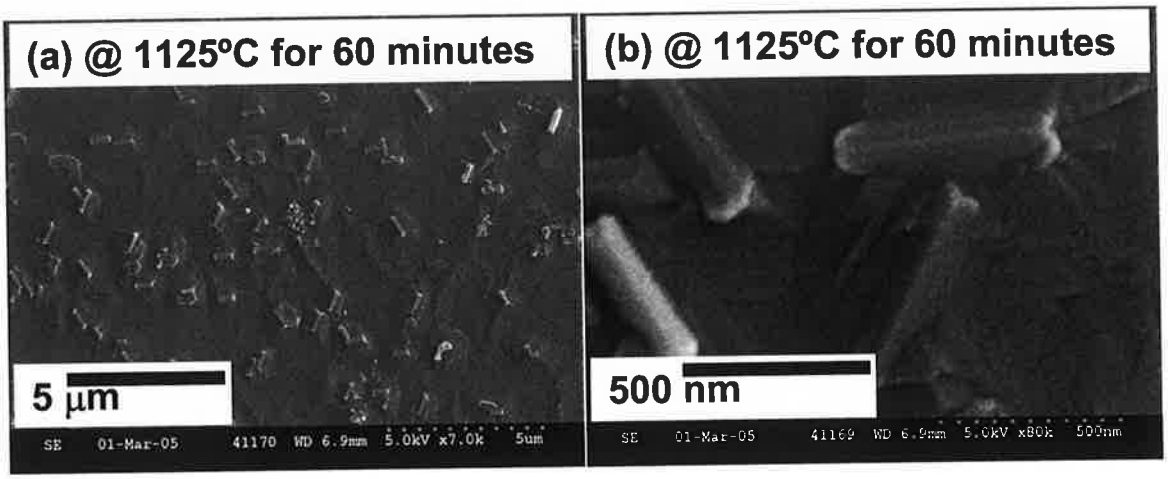

Figure 6.12 FE-SEM images of samples grown on c-sapphire; (a) growth temperature 1125 °C (growth duration 60 minutes); (b) higher magnification of sample in (a).

Figure 6.12 shows that zinc aluminate grains are again prominently visible, although the contrast and density are reduced compared to the samples grown at 950 °C for 30 minutes (Figure 6.1(a) - (d). The strong contrast of the central line portion of the microstructure is gone. These zinc aluminate grains are strongly affected by the growth duration, particularly at the higher growth temperature.

The long direction of the structures are again parallel to <10-10> -type sapphire in-plane directions, in all cases, as confirmed by x-ray phi scans. The width of the microstructures seen in Figure 6.12(b) is much closer to the width measured by AFM line profiles for samples grown for shorter durations shown in Figure 6.2, ~ 200 nm, indicating a change in the nature of the SEM contrast for samples grown at 1125 °C for 60 minutes, compared with samples grown at lower temperature or for shorter durations. Cross-sectional TEM

measurement on samples grown at 1125 °C for 60 minutes, with significantly different morphology in SEM/FESEM of samples grown for 30 minutes, are shown in Figure 6.13.

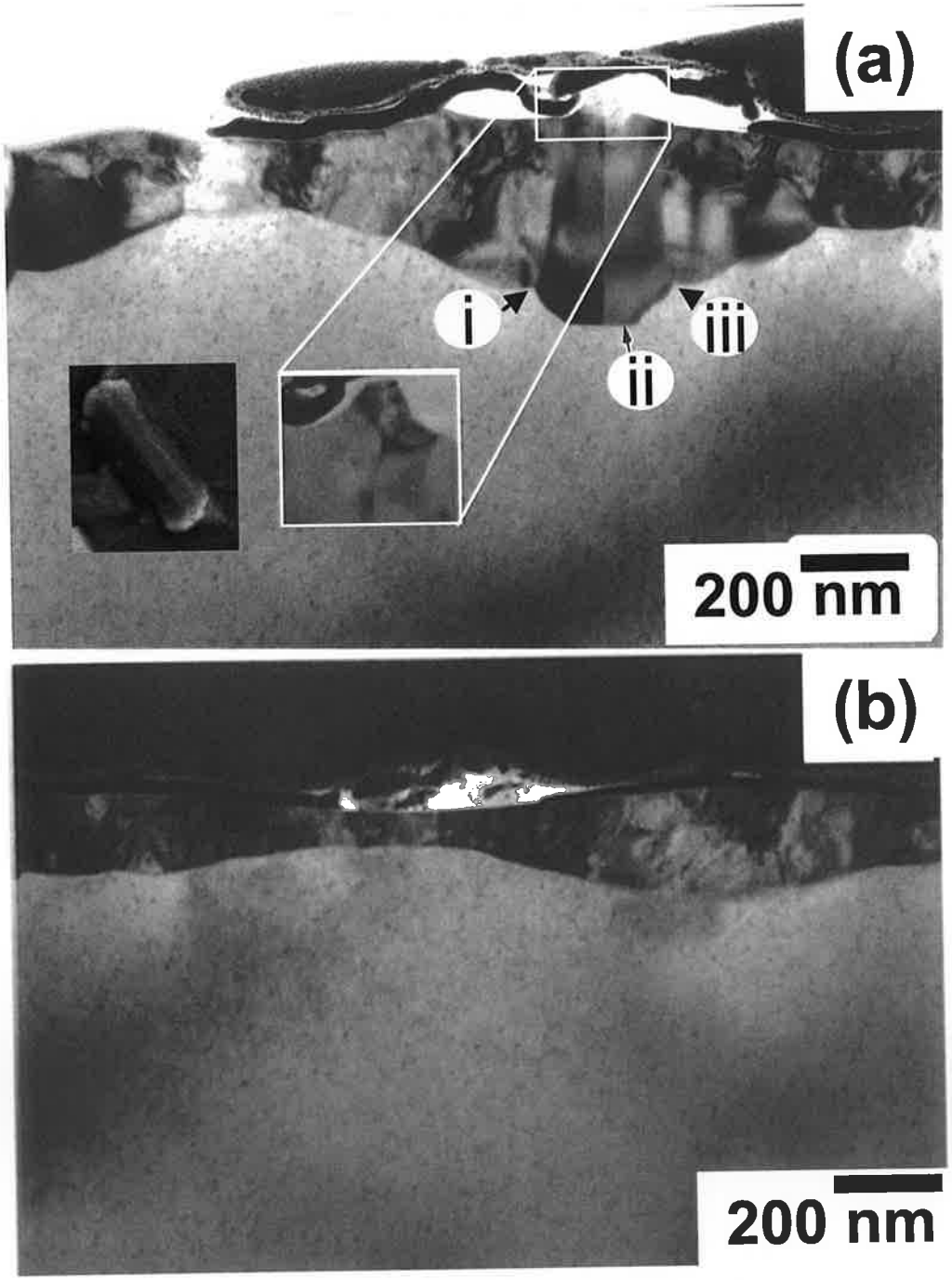

Figure 6.13 (a) Cross sectional TEM image at high magnification on sample grown at 1125 °C for 60 minutes (the inset shows a FESEM image of the zinc aluminate grains seen on this sample; (b) Other region of deposit with varying thickness and high defect content.

Figure 6.13(a) shows an area where a high thickness grain (marked at (ii)) has been formed. The sapphire substrate shows a low defect density due to annealing of extended defects during the longer growth period at higher temperatures. The grain itself is similar to the coarse aluminate grains formed in the previous samples with a twin boundary running through its centre and with high angle grain boundaries on both sides, marked at (i) and (iii), while the surrounding material is a thinner layer of high defect content. However, in this case the grain shows much clearer evidence of faceting at the sides and base, and also at the top portion, which is shown in the inset. We again identify these large, twinned, zinc aluminate grains with the symmetric structures seen in FESEM, and note that this identification is supported by the observation of the facetted nature of the grains seen both in TEM in Figure 6.13(a) and in FESEM (inset of Figure 6.13(a)). The absence of the bright central line seen in FESEM contrast in this sample may then be due to change in the nature of the twin boundary plane with a consequent effect of the contrast mechanism, discussed in section 6.4 below. Other regions of deposited layer of this sample have a morphology like that shown in Figure 6.13(b), a thinner layer with a thickness variation, and high defect content.

The SAED pattern in Figure 6.14 is recorded with a sapphire [10$\bar{1}$0] zone normal and aluminate [0-11] zone normal, with the aluminate reflections indexed accordingly. The deposit again is identified as zinc aluminate. The twin plane is an aluminate (-211) plane in this case (different to the situation for samples grown at 950 °C for 30 minutes), and the epitaxial relationship is:

$$[1\text{-}210]\ Al_2O_3\ //\ [\text{-}211]\ ZnAl_2O_4 \text{ and } (0001)\ Al_2O_3\ //\ (111)\ ZnAl_2O_4$$

These types of epitaxial and twinning relationships have been observed previously for the magnesium aluminate and other spinels, and the epitaxy of the (111) $ZnAl_2O_4$ plane on the (0001) Al_2O_3 plane is often seen in such systems due to the three-fold symmetry of both surfaces [5 - 8]. These epitaxial and twinning relationships indicate that the intersection of the twin boundary of the aluminate grain with the surface is again a line parallel to the

sapphire [10-10] in-plane direction, parallel to the long direction of the symmetric structures seen in Figure 6.12(b).

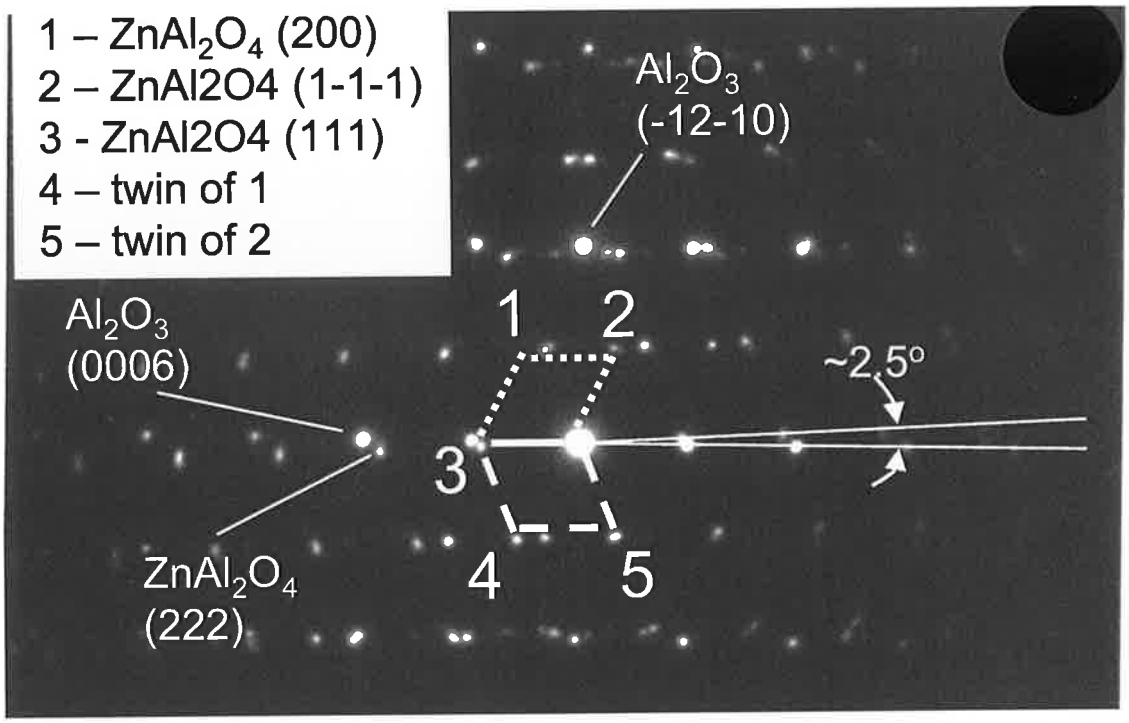

Figure 6.14 *SAED pattern of region in with reflections of aluminate twins indexed at a sapphire [10-10] zone normal and an aluminate [0-11] zone normal;*

A slight (~ 2.5 °) misalignment of the (111) zinc aluminate plane from the sapphire (0001) plane, is seen, indicated in Figure 6.14.

6.3 Effects of Substrate Preparation

The perfection of the substrate is an extremely important factor in the growth of the growth of the high SEM contrast symmetric structures as shown below (Figure 6.15(a)). This figure shows a FESEM image of a sample grown at 950 °C for 30 minutes, but on a substrate pre-annealed at 1000 °C for 30 minutes. Similar FESEM data are obtained on samples pre-annealed at 1000 °C for 17.5 hours and on samples grown on starting substrate

material of higher crystalline quality. These samples show a very different appearance in FESEM images, with very few instances of the high contrast three-fold symmetric structures. It appears that the presence of the symmetric microstructures is critically dependent on the initial crystalline quality of the substrate.

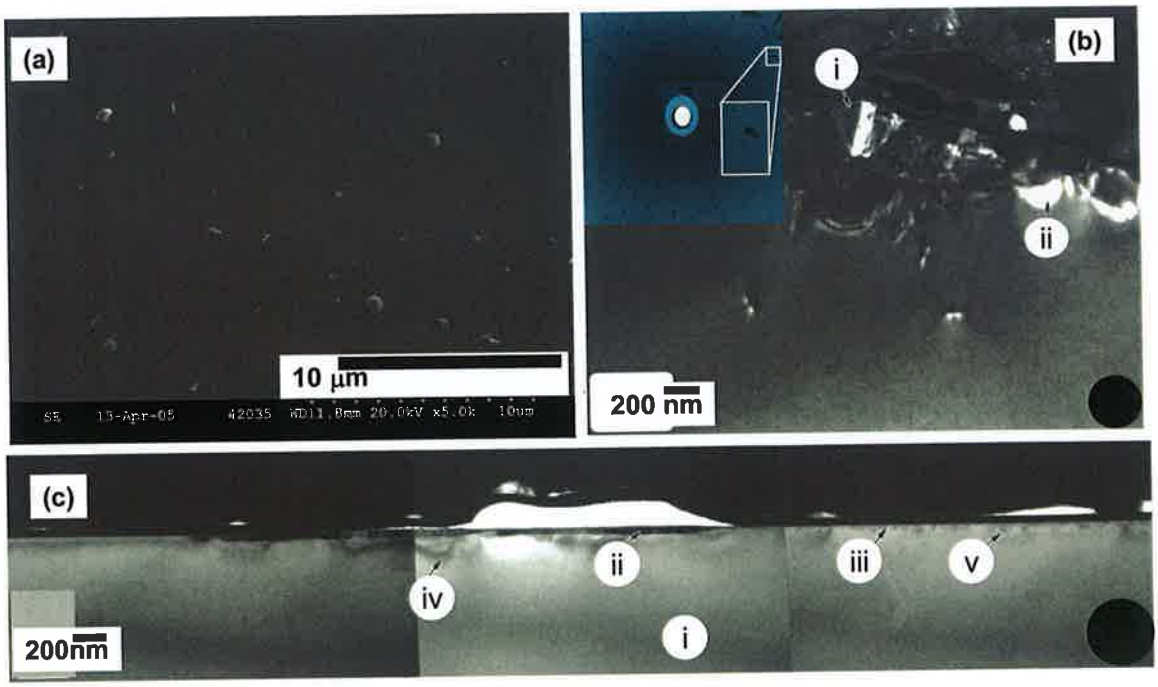

Figure 6.15 *(a) Sample grown at 950 °C for 30 minutes on pre-annealed substrate, with low symmetric microstructure coverage; (b) Dark field cross-sectional TEM data for a sample grown at 950 °C for 30 minutes on an unannealed substrate, showing a high thickness grain marked at (i), and the highly defective substrate below this (substrate is in lower half of image). The region marked (ii) is a type of large hole, similar to the feature marked (vi) in Figure 6.7(a). The inset shows a Laue pattern for the substrate with one spot magnified to illustrate broadening; (c) Bright field cross-sectional TEM data for sample shown in (a).*

The image in Figure 6.15(a) shows a low coverage of zinc aluminate grains. Figure 6.15(b) shows a dark field cross sectional TEM image, for sample grown at 950 °C for 30 minutes on an unannealed substrate (similar to that in Figure 6.1(a)), close to a high thickness grain, marked (i), and the high substrate defect density is easily seen around the grain. Laue pattern measurements of unannealed substrates show a significant splitting and distortion of

the reflection spots (inset of Figure 6.16(b)) which are associated with the poor crystal quality of the starting material and specifically the presence of slightly misoriented sub-crystals, grain boundaries and extended defects. Laue measurements on annealed substrates and other starting materials show much more sharply defined spots, indicating a reduction in the extended defect concentration of the material. TEM data shown above (Figure 6.15(b)) confirm this conclusion. The presence of the three-fold symmetric line structures is therefore apparently critically dependent on the presence of extended defects in the starting substrate material. It should also be noted that such high thickness grains do not appear at every region where the substrate defect density is high, and equally these large thickness grains are seen occasionally in regions where the substrate defect density is lower. Thus there is no one-to-one evidence of a connection between specific extended defects in the substrate and nucleation of specific high thickness grains. However, a comparison of Figure 6.15(b), with a cross-sectional TEM image of the sample shown in Figure 6.15(a) (deposited under the same conditions of time and temperature but on a substrate that had been given a pre-anneal treatment for 30 minutes at 1000 °C) is very informative. Part of the region that was thinned to electron transparency is shown at relatively low magnification in Figure 6.15(c) and one sees that the substrate marked at (i) has a significantly lower defect density than in Figure 6.15(b), as a consequence of the pre-anneal (the contrast marked at (iv) and (v) is strain related). The data in figure 6.15(a) shows that the coverage of the associated symmetrical structures is very low. This leads us to conclude that the presence of highly defective substrates (low crystal quality substrates) is necessary for the nucleation and growth of such twinned grains with three fold symmetry. Annealed sapphire or starting sapphire substrates of better quality do not show significant amounts of these microstructures after deposition.

We show further evidence in Figure 6.16 in support of the hypothesis of a relation between extended defects in the substrate and nucleation of symmetric structures. The FESEM images of a sample grown at 1125 °C for 30 minutes, show nucleation of the symmetric structures at various locations. While a significant fraction of the symmetric structures are randomly distributed, we also observe a clustering of the microstructures along straight line directions at some locations (Figure 6.16), which is suggestive of the phenomenon of

clustering of etch pits along the array of dislocations which intersect the surface of a crystal at low angle grain boundaries. Laue pattern data from Figure 6.3(a) show that the sapphire substrates used have slightly misoriented sub-crystals and associated grain boundaries and extended defects and this may explain the occasional nucleation of microstructures along straight line directions associated with such boundaries.

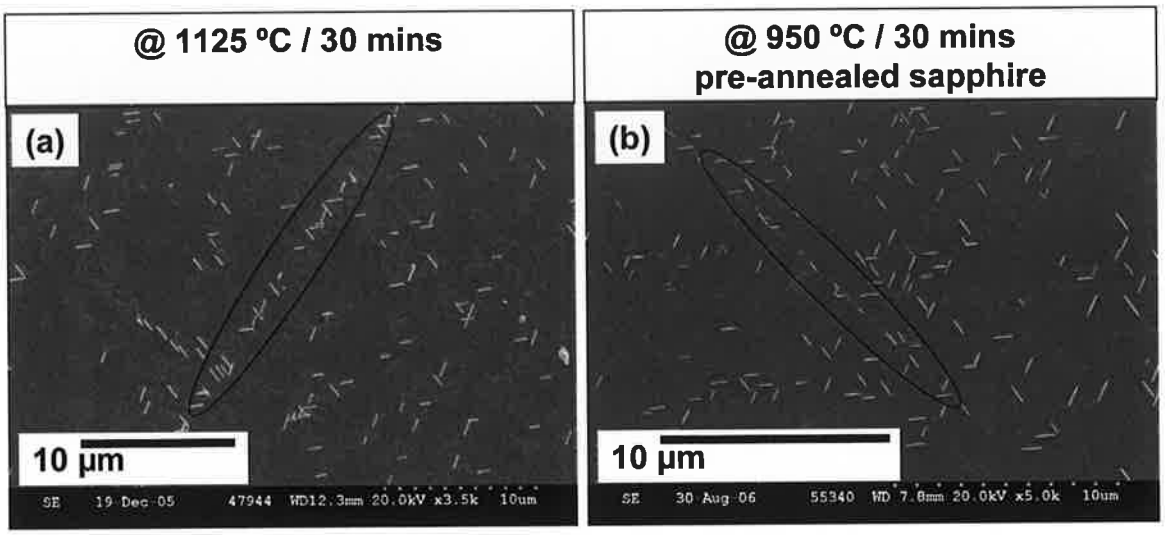

Figure 6.16 FESEM image of zinc aluminate grains on the c-sapphire, (a) grown at 1125 °C for 30 minute, (b) grown at 1100 °C for 30 minutes on the pre-annealed Fractured substrate (at 1000 °C for 120 minutes). Evidence is seen for structures clustering along straight lines in certain locations.

We have also pre-annealed (1000 °C for 2 hours) substrates (to ensure low extended defect concentrations) and subsequently introduced mechanical damage to the crystal in a number of ways and then deposited zinc aluminate. After deposition we looked for evidence of symmetric microstructure growth. The initial and rather crude method used was to mechanically stress a pre-annealed substrate to the point of fracture. Close to fracture locations (and also at samples edges where the substrate was cut with a saw) we see the characteristic high contrast symmetric structures (Figure 6.17), and in some cases these cluster along a crack location.

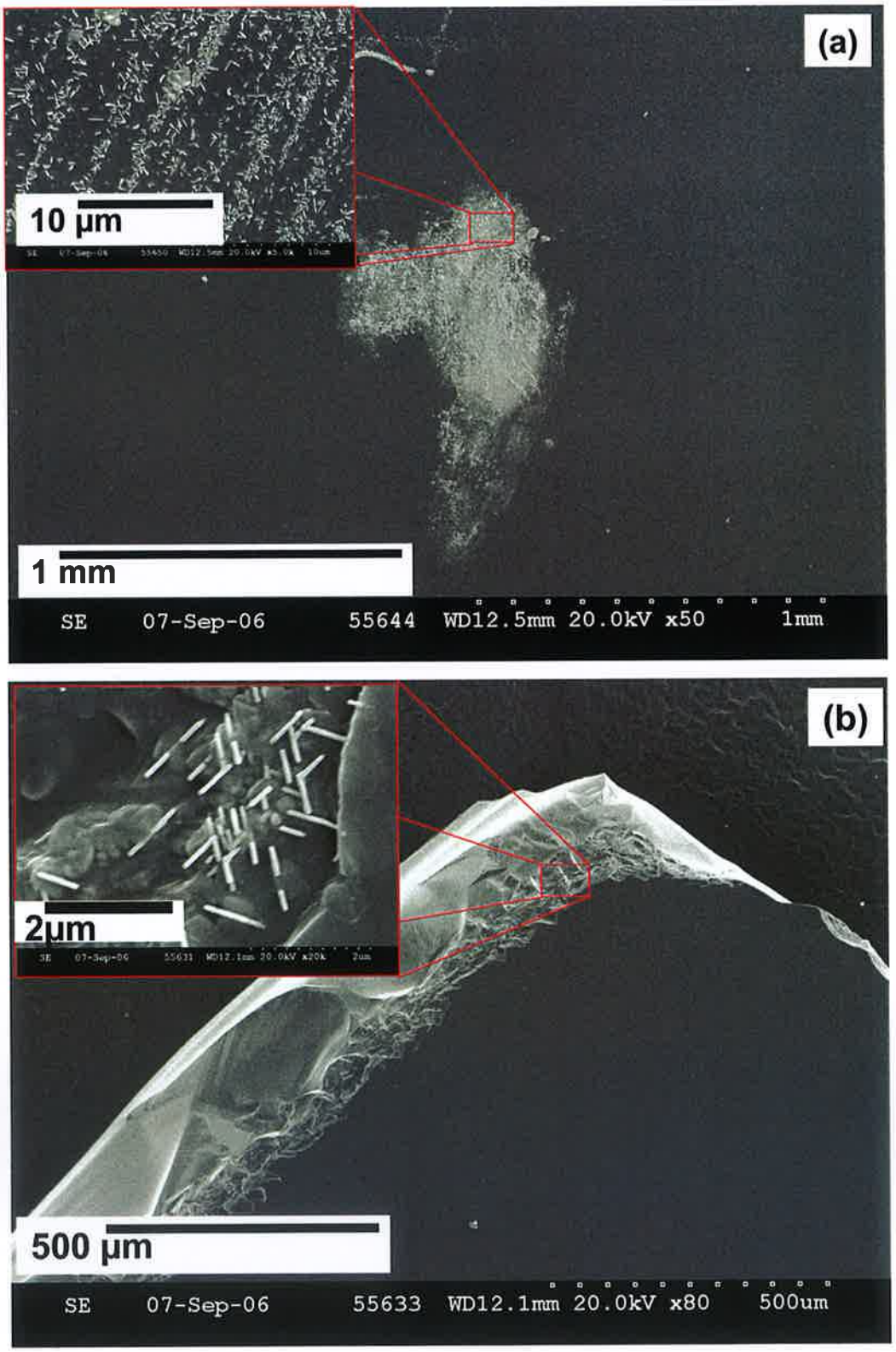

Figure 6.17 FESEM image of zinc aluminate grains grown on the fractured sapphire; (a) close to the fracture locations, (b) edges of fractured sapphire,

We believe that these nucleate due to the generation of extended defects in the sapphire at or close to the point of fracture. Reference pre-annealed samples not subjected to mechanical stress before growth show very little evidence of this microstructure after attempted aluminate growth.

More controllable, localised, attempts to introduce mechanical damage have included plasma etching and laser ablation (both surface and sub-surface) of the sapphire. We have also tried to 'damage' the *c*-sapphire surface by polishing it using aluminium oxide powders of dimensions 0.3 μm, 1 μm, and 3 μm. In these cases we have not yet observed growth of these microstructures after the substrate treatment. We have also tried to damage the *c*-sapphire substrate by wet chemical etching (in an etching solution: 20 ml H_2O_2 + 2 ml HF, 48 % in H_2O_2 + 20 ml HCl, 0.996 N), and grow zinc aluminate grains after that. We etched samples for 3 different periods: 15 minutes (Figure 6.18(a)), 30 minutes (Figure 6.18(b)), and 60 minutes (Figure 6.18(c)). Some evidence is seen for growth of zinc aluminate grains with characteristic 3-fold symmetric microstructures in this case, but further work is needed to confirm the reproducibility of these results.

These etching and other studies are at an early stage (see chapter 7 also) and there is not yet enough data to comment on the detailed nature of the extended defects which may be responsible for the nucleation and growth of the coarse zinc aluminate grains. However, based on the totality of the evidence presented here however, we believe that the intimate connection between the presence of extended defects in the sapphire and the nucleation of symmetric microstructures is quite convincing.

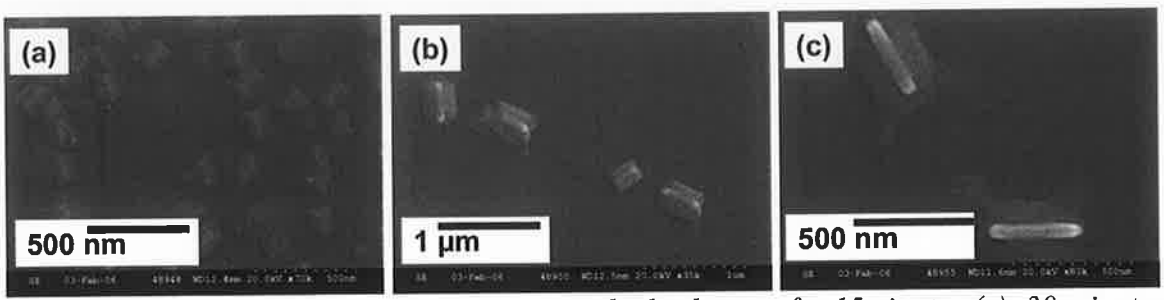

Figure 6.18 Grow zinc aluminate grains on etched substrate for 15minutes (a), 30 minutes (b), and 60 minutes (c).

6.4 Nature of Unusual SEM Contrast - Electron Channeling along Twin Boundaries

The zinc aluminate microstructures discussed above show a number of interesting features, including two well-defined twin relationships, depending on the growth duration, which in turn appear to have a very significant impact on SEM contrast mechanisms.

Large grains synthesized at shorter growth durations (950 °C for 30 minutes) show unusually bright, narrow, linear structures with sharp contrast in FESEM. These large grains in all cases show twin boundaries and a sharp contrast in FESEM. The twin boundaries are very visible in the grains. AFM data presented in this chapter (Figure 6.2) show a topography consistent with the rather broad (500 nm) grain size seen in TEM, and clearly the narrow linear features seen in FESEM are not associated with the broad aluminate grains, but rather with the twin boundaries. This identification is supported by the fact that the linear features and twin boundaries have the similar lengths of the twin boundaries and FESEM features (~ 500 nm) and also by the very narrow appearance of the linear features in FESEM, and the lateral dimension of these features (~ 70 nm), which is unchanged by the obvious variations in grain to grain width seen in TEM, indicating that the structures responsible for the FESEM contrast must be smaller then the actual grain size and be unchanged by the variations in grain width.

Epitaxially-grown grains synthesized at longer growth durations (1125 °C for 60 minutes) display a different twinning relationship, and the FESEM contrast is significantly reduced. It is clear that neither the topography nor material composition vary substantially between the two types of sample and thus cannot explain the large observed differences in SEM contrast. The main difference between the large grained and the surrounding region in both samples is the presence of twin boundaries in the large grains. The main difference between the grains in the two samples is the different twin plane. Thus the different nature of the twin plane in the samples grown at 1125 °C for 60 minutes must account for the change in the SEM contrast.

In FESEM by controlling the accelerating voltage, we can control the incident electron penetration depths, and these investigations can shed light on sub-surface processes in the sample. We have investigated the appearance of the zinc aluminate symmetric structures in samples grown at 950 °C for 30 minutes in an FESEM using both the secondary electron (SE) and backscattered electron (BE) imaging modes in an attempt to elucidate the origin of the sharply defined linear structures seen in SEM images of samples grown at 950 °C for 30 minutes. These samples have been sputter-coated with ~ 10 nm of Au prior to examination in the SEM to reduce charging effects. We have studied the contrast in both secondary electron (SE) and backscattered electron (BE) FESEM images for samples grown at 950 °C for 30 minutes, at accelerating voltages between 1 kV and 20 kV (Figure 6.19). The lower voltage is chosen so that the beam penetration depth is less than the 10 nm sputtered Au layer thickness [9]. It is clear that for 1 kV beam voltage (Figure 6.19(f), no clear image is seen in either SE or BE mode, while for 2 kV beam voltage (Figure 6.19(e), a clear image is seen in SE mode, but not for the BE imaging mode. For 1 kV, the incident electron beam cannot penetrate the 10 nm Au layer to interact with the aluminate and no image is seen in SE or BE, whereas a clear SE image is seen at 2 kV, where the incident beam can penetrate to the aluminate grains. At higher voltages both SE and BE images of the linear structures are seen. It is clear that the width of the bright linear structures in both modes is not strongly affected by change of one order of range in the incident beam energy. The width of the linear structures in SE between 20 and 5 kV varies from ~ 70 nm to ~ 85 nm, respectively. The linear features in the SE image at 2 kV (Figure 6.19(e)) have a width of ~ 120 nm.

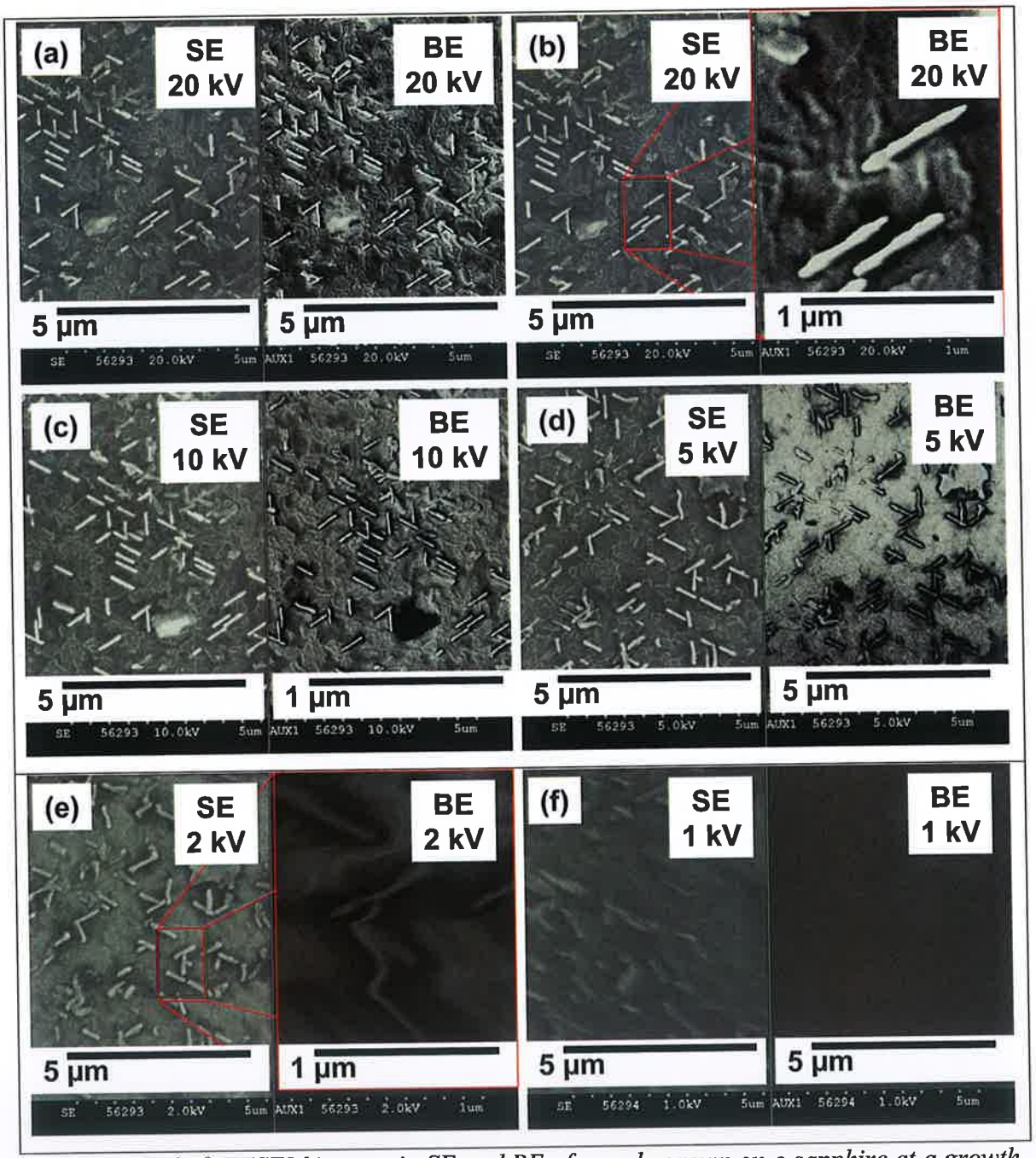

Figure 6.19 (a-f) FESEM images in SE and BE of sample grown on c-sapphire at a growth temperature 950 °C for 30 minutes, at accelerating voltages between 1 kV and 20 kV.

Such images taken at low voltage show that the strong contrast seen in the linear structures is associated with BE phenomena, either directly detected by the BE detector of the SEM or

detected by the SE detector due to SE emission by BE within the SE escape depth. Figure 6.20 shows proposed model to explain the SEM images.

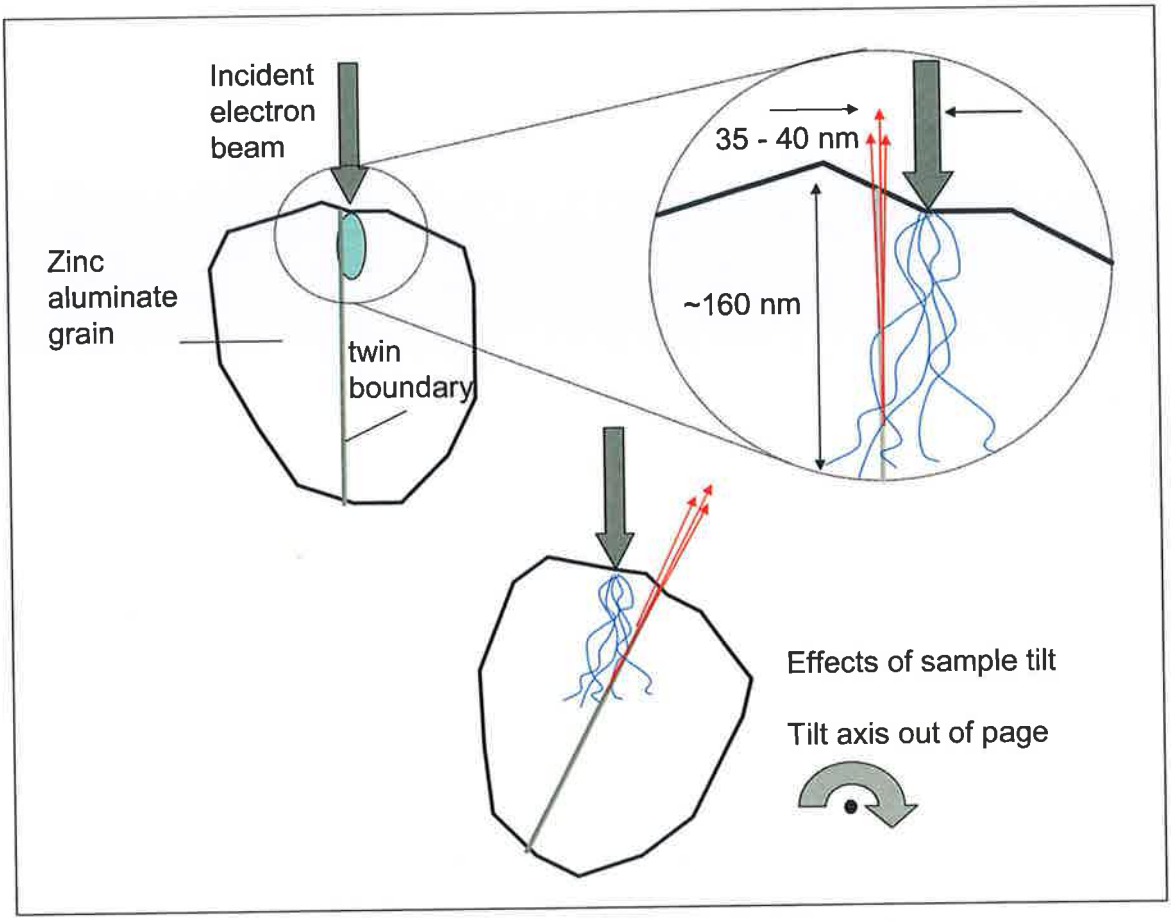

Figure 6.20 Schematic diagram of proposed model for enhanced backscatter along the twin boundary (channels) in sample grown at 950 °C.

We propose that the portion of the incident electron beam which is backscattered can channel (or waveguide) along the twin boundary (channeling effects in SEM typically refer to Bragg reflection phenomena, which is not what is proposed here [10]). These backscattered electrons can then generate secondary electrons when they impinge on the Au layer, which generate the narrow linear features either in SE or BE imaging modes. This proposal is supported by the observation in cross-sectional TEM that the twin boundaries in samples grown at 950 °C for 30 minutes show a low density, or "open" character. This is demonstrated in Figure 6.21 below where the twin boundary itself exhibits strong Fresnel

fringing effects as a function of the change in defocus conditions. The sense of the contrast changes is indicative of the fact that this part of the oxide is of lower scattering potential than the crystalline material lying to its sides [11]. Analysis of the Fresnel fringes as a function of focusing condition indicates that the thickness of this low density region is > 2 nm. These data and conclusions are based on discussions with Dr. Simon Newcomb of Glebe Scientific Ltd.

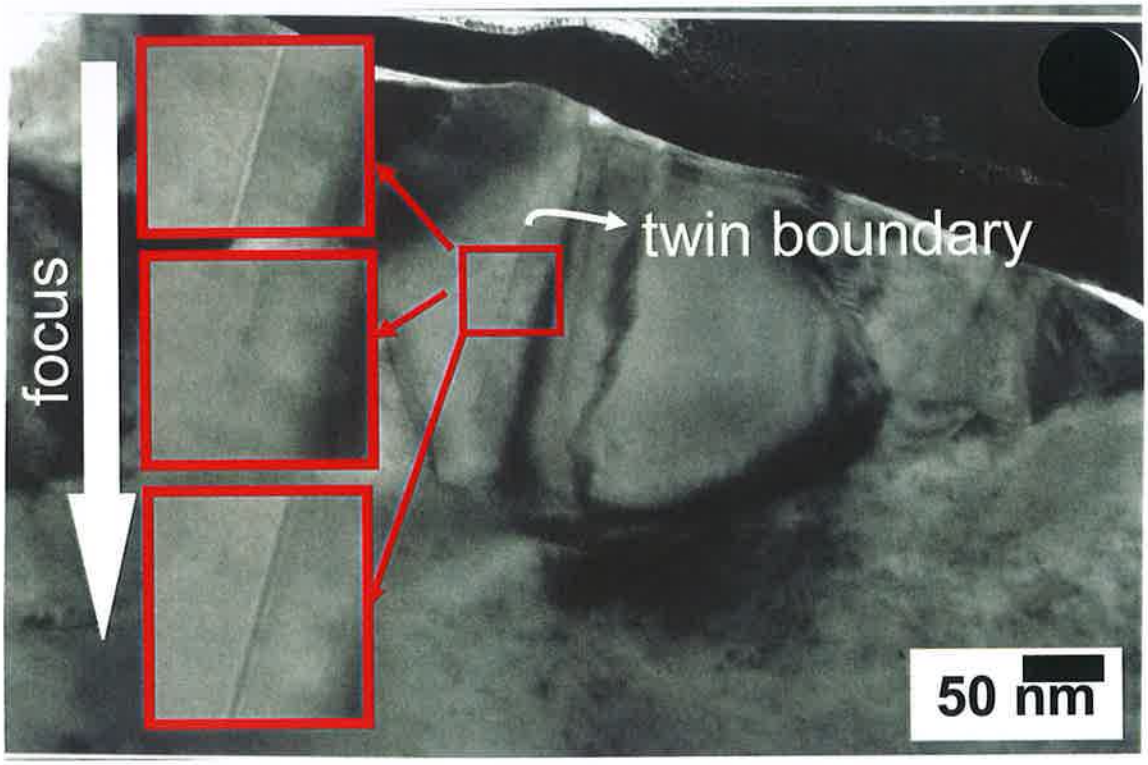

Figure 6.21 Cross-sectional TEM showing Fresnel effects as a function of defocus conditions for a sample grown at 950 °C for 30 minutes.

The presence of this lower density region provides an open channel along which electron backscattering may be particularly efficient. The proposed model may be further tested by looking at SE images of the structures under a large tilt angle (45 °) shown in Figure 6.22.

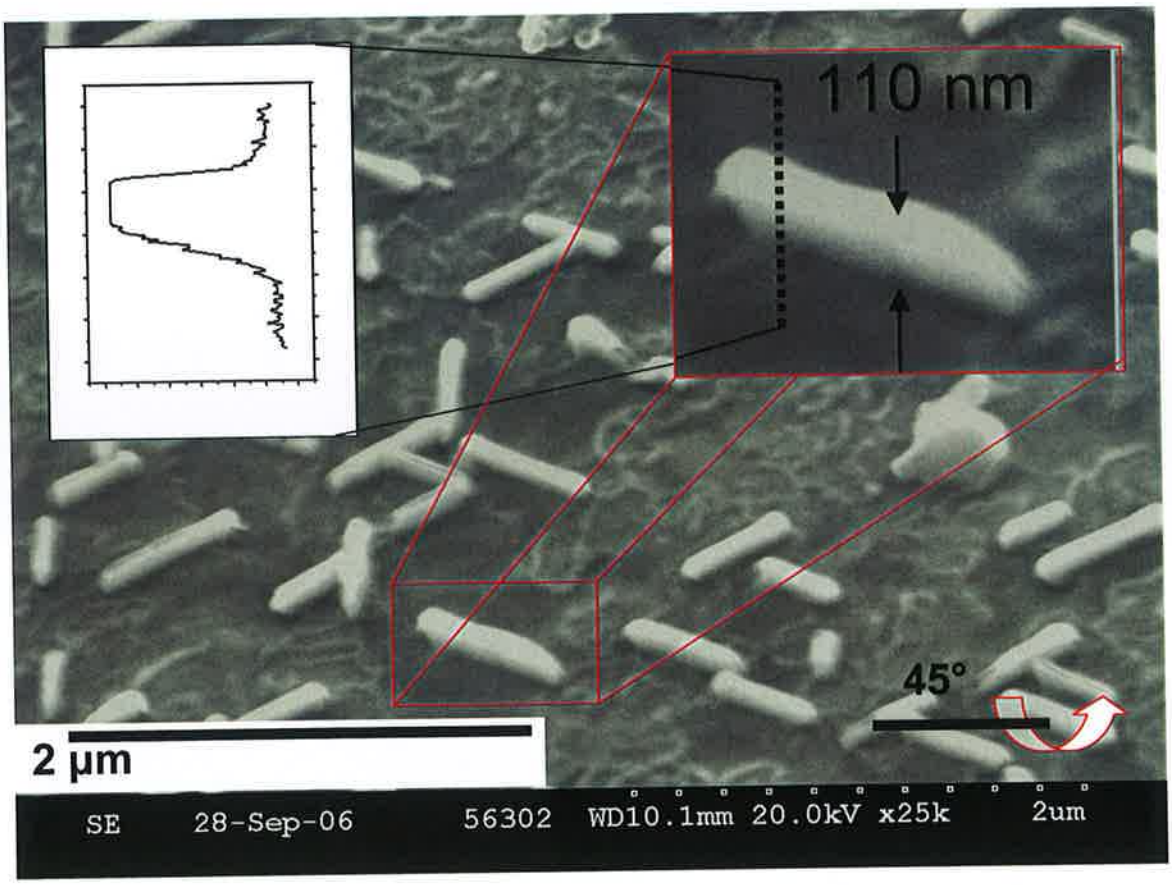

Figure 6.22 SEM image on sample tilted at 45 °, with line scan of grey scale intensity across single feature shown in inset

The tilt axis is a horizontal line in the plane of the page and the sample is tilted so that the upper portion of the sample is further from the incident beam, and the lower part is closer. When the sample is tilted such that the electron beam direction lies out of the twin boundary plane, noticeable elongation or smearing of many of the linear structures is seen (~ 110 nm), as demonstrated by the circled portion of Figure 6.22 and the inset line scan. This is shown schematically in the lower part of Figure 6.20. The elongation is not seen when the electron beam direction remains in the twin boundary plane (the vertically oriented linear structures). The elongation circled in Figure 6.22 is consistent with the proposed waveguiding mechanism because the sample tilt allows the incident beam to intersect the twin boundary over a larger region of the beam scan. The effect is not due to topography, as indicated by AFM data referred to earlier and also because the elongation is perpendicular to the tilt axis, although the linear structures in question are not. The incident

beam penetration depth at the accelerating voltage used for the data in Figure 6.22 is > 1 μm. Based on the degree of elongation observed, it appears that the region below the surface from which the waveguided BE escape to reach the surface and generate the BE, or SE, signals, is rather small, within ~ 160 nm of the surface. This shallow depth indicates that residual loss mechanisms during waveguiding may limit the region from which high energy BE can contribute to the contrast. We propose that the BE responsible for this local contrast are generated by large angle elastic collisions (> 90 °) of incident electrons directly interacting with the twin in this sub-surface volume which channel-out along the open twin boundary. The reason for the consistently narrow observed feature widths may be explained by noting that the beam width at depths ~ 160 nm below the surface is ~ 70 nm. BE generated by the incident beam outside the twin boundary region which reach twin boundaries have a large transverse momentum component (due to multiple smaller angle collisions) and are not effectively "captured" and waveguided along the open twin boundary. The combination of these two effects produces the rather narrow (~ 70 nm) feature widths seen in both SE and BE modes. At lower accelerating voltages the beam widths at depths of ~ 160 nm below the surface increase, leading to the increase in feature width commented on earlier. Further work using Monte-Carlo simulations of electron trajectory with the Casino programme will be used to explore this effect in the future [12].

The detailed nature of the twin boundary appears crucial to the observation of this waveguiding effect. It is quite clear from the data shown above in Figure 6.12 that the effects of electron waveguding in the twin boundary are reduced or even eliminated in samples grown at 1125 °C for 60 minutes type of boundary. The differences in the two twin boundaries appear crucial to the observation of the enhanced backscatter proposed above.

The twin boundary in samples grown at 1125 °C for 60 minutes also shows Fresnel effects with changes in defocus conditions (Figure 6.23), indicating an open nature to this boundary also.

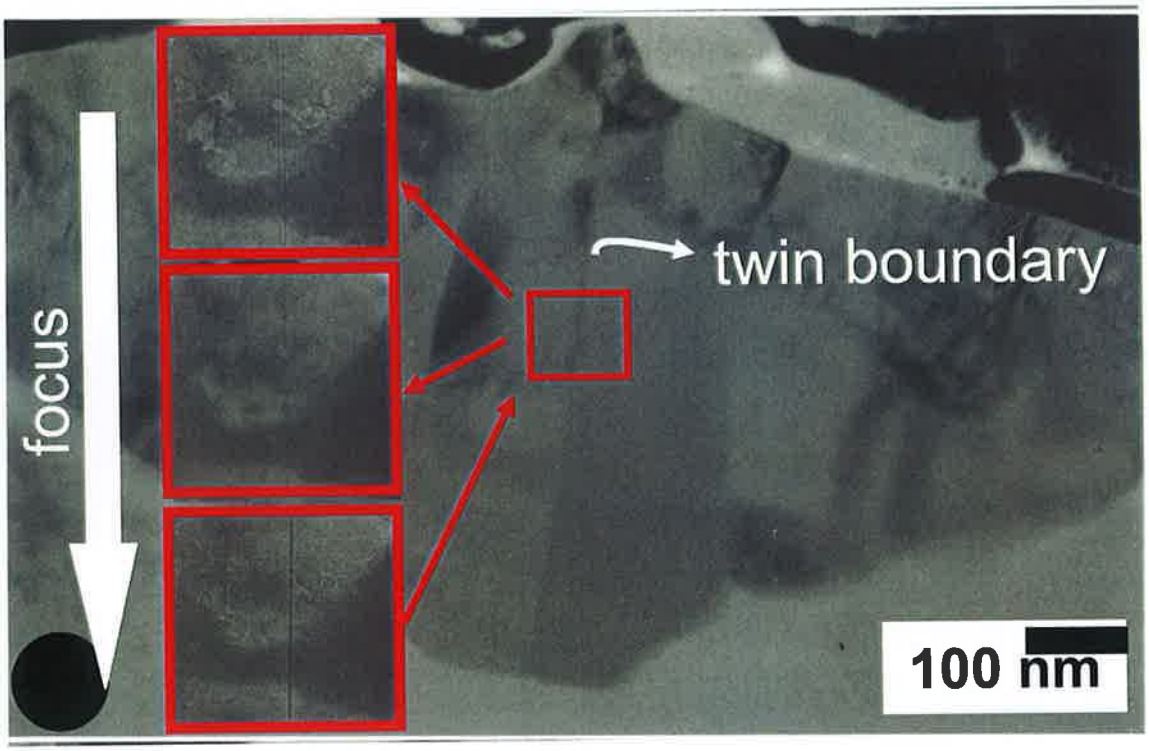

Figure 6.23 Fresnel effects as a function of defocus conditions for a sample grown at 1125 °C for 60 minutes.

Analysis of the Fresnel fringes as a function of focusing condition for this type of twin boundary indicates that the thickness of the low density region is ~ 1 nm. These data and conclusions are also based on discussions with Dr. Simon Newcomb of Glebe Scientific Ltd.

It is tempting to propose that the elimination of the waveguiding effects is due solely to a reduction in the thickness of the low density region, and certainly it is possible that a narrower boundary region would reduce such effects. Nevertheless the crystallography of the twin boundary may also play an important role. In the case of the magnesium spinel, when the twin boundary departs from a (111) plane, while still containing the [01-1] rotation axis, the twin boundary consists of an array of linear defects [6]. This geometric situation is exactly the case for the grain shown in Figure 6.23, and given the structural similarity of the magnesium and zinc spinels, it is likely that the (-211) twin boundary in zinc aluminate is a more defective interface compared to the (111) twin. The presence of

this defective interface may also play a role in reducing the efficiency of electron waveguiding along the twin boundary in the sample grown at 1125 °C for 60 minutes. Our data at present do not permit us to distinguish between these two effects.

6.5 Growth Mechanism

The growth mechanisms of aluminate spinels due to reaction between metal oxides and alumina is a topic which has been widely studied, both by observing the reaction between solid metal oxides and alumina and by observing spinel growth by vapour phase deposition of the metal oxide and subsequent reaction with the substrate [5, 13]. This latter mechanism appears to be the origin of the growth in our samples. Initially ZnO is deposited on the *c*-sapphire surface by VS deposition, and this ZnO layer reacts with the substrate to form zinc aluminate, according to the formula:

$$ZnO + Al_2O_3 \rightarrow ZnAl_2O_4$$

This growth mode has been observed previously for magnesium aluminate, cobalt aluminate and nickel aluminate and appears to be the most plausible growth mode in our case also [5, 7, 14]. We see growth of characteristically twinned, epitaxially oriented zinc aluminate grains only for furnace temperatures above 950 °C and see no growth of such grains at temperatures greater than 1125 °C.

We attribute the lower temperature limit to the low Zn pressures in the chamber as the carbothermal reduction of the source powder mixture does not proceed efficiently below this temperature, as discussed in chapter 2. The defects at which the twinned, epitaxially oriented grains nucleate will tend to anneal out before significant ZnO can deposit and no such microstructures will form. Similarly the higher temperature limit we believe is due to fast sample annealing which eliminates defects very quickly at such temperatures and hence the twinned, epitaxially oriented grains cannot effectively nucleate at high temperatures also. There appears to be a small temperature window in which the ZnO can deposit at a sufficient rate at defects in the sapphire and then react to form the twinned aluminate grains. It is likely that zinc aluminate layers continue to form below and above this

window, though we have not studied layers grown outside this temperature region. Growth of thin zinc aluminate layers on pre-annealed substrates (as in Figure 6.15(c)) supports this suggestion.

The nucleation and evolution mechanisms of the symmetric microstructures at extended defects in the substrate are both interesting questions. Previous studies on twinned nickel aluminate spinels grown by reaction of a vapour deposited layer of NiO on sapphire have attributed the origin of the twins in the aluminate to the presence of twins in the deposited NiO layer prior to reaction with the sapphire [15], and there was no evidence that substrate-dependent effects were seen. The twinning of the initially deposited NiO layer may have occurred to reduce stress in the film. We propose a similar mechanism for the nucleation of the symmetric microstructures we observe, but the mechanism must account for the relationship between extended defects in the sapphire and the nucleation of the symmetric microstructures in our case. ZnO grows epitaxially without twinning on single crystal *c*-sapphire [16], but it may be the case that the deposited ZnO layer will grow in a locally different fashion close to positions on the substrate where extended defects intersect the surface, due to local alterations in the surface structure. The initial ZnO layer may grow in a twinned fashion in such regions, leading to the characteristically twinned zinc aluminate grains after reaction with the sapphire. This would explain the presence of multiple twins in terms of regions where the local defect content and surface structure cause a multiple twinned ZnO layer to nucleate. The range of size of the twinned microstructures is most likely due to the range of sizes of the original nucleation sites. Our experimental data do not allow us to test this hypothesis any further at present, as the combined effects of the aluminate growth into the sapphire and annealing of sapphire during growth mean that the initial nucleating structures disappear during subsequent growth.

The growth rate of the aluminate deposit after nucleation is clearly quite different for the polycrystalline layer region (i.e. the low thickness (< 50 nm) region shown in Figure 6.4), compared to the larger, epitaxially oriented, aluminate grain structure shown in Figure 6.5. A number of previous studies of growth of zinc aluminate on sapphire are reported in the recent literature [17-19]. For growth at lower temperatures (680 °C) [18, 19] the growth is

reported to be diffusion-limited (following a parabolic thickness vs. time relation), with Zn as the diffusing species and an associated interfacial layer of different stoichoimetry (Zn deficient) is observed [19]. Growth at higher temperatures is reported to be interface-limited (following a linear thickness vs. time relation) and no Zn deficient interfacial layer is reported [17]. These reports are not contradictory since the diffusion constant of the reacting species, e.g. Zn, would be expected to increase at higher temperatures, changing the nature of the rate limiting step in the reaction. In addition the crystallographic nature of the reacting interfaces may also alter the rate limiting step in the reaction. In reference [17] the thickness of aluminate layers formed by the reaction of ZnO layers with sapphire at temperatures of ~ 1000 °C in 30 minutes is ~ 40 nm, which is quite consistent with our data for the thin polycrystalline layer seen in Figure 6.4 for a grown at 950 °C for 30 minutes. However, the much greater thickness of the larger grains (~ 400 nm) seen in these samples implies different growth kinetics for these microstructures. The cross-sectional TEM images shown in Figure 6.21 of the twin boundary in a sample grown at 950 °C for 30 minutes indicate that this region of the oxide is of lower density than the material lying to its sides [20]. The width of the boundary was acquired from a measurement of the fringe spacing in the in-focus image and is in the region of ~ 2 nm. The lower density "open" twin boundary region will enable enhanced diffusional transport for source material to the sapphire – aluminate interface, leading to much higher reaction and growth rates close to twin boundaries, as seen in our samples. Previous reports provide evidence for a similar effect close to zinc aluminate grain boundaries [17].

The evolution of the large, twinned grain structures as a function of growth time has been presented above in Figures 6.1, 6.12 and 6.13 These data show that the morphology of the large grains in samples grown at 1125 °C for 60 minutes differs markedly from that of grains in samples grown at 950 °C for 30 minutes, with a substantially more facetted appearance and exhibiting different twinning and epitaxial relationships to the substrate. The fact that the direction of the long axis of the symmetric structures seen in SEM is identical in both cases, and that the topography of the microstructures seen in samples grown at 1125 °C for 30 minutes are so similar to those seen in samples grown at 950 °C for 30 minutes leads us to conclude that the large, unfacetted, twinned grains seen in

growths at shorter durations evolve with increasing growth time to the facetted, twinned grains seen in samples grown at 1125 °C for 60 minutes, through a transformation due to annealing effects during growth. Experiments examining the effects of annealing on samples grown at 1125 °C for 30 minutes confirm this conclusion. Figure 6.24 shows SEM images of two samples prepared under identical conditions (1125 °C growth for 30 minutes), except that the image in Figure 6.24(b) is taken from a sample which had an additional annealing step in argon gas (no source material in tube) for 40 minutes. Figure 6.24(a) shows the presence of symmetric microstructures with high SEM contrast typical of growths for shorter duration shown in the main text, while Figure 6.24(b) shows a facetted microstructure consistent with the longer duration growths reported in the text. These data indicate that the evolution between the two microstructures is due to the annealing effects associated with longer growth durations.

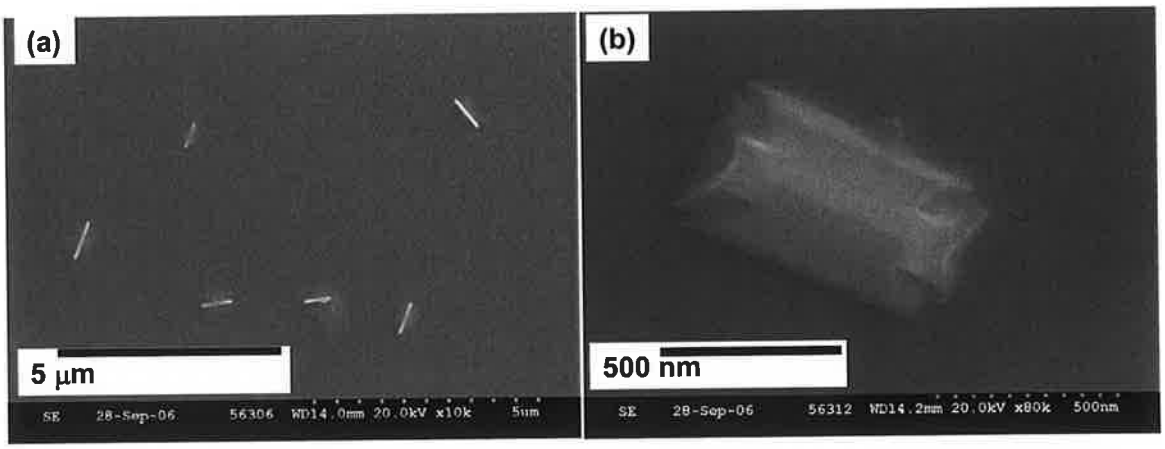

Figure 6.24 (a) Field emission SEM image of structures grown at 1125 °C for 30 minutes, showing three-fold symmetric microstructures with high SEM contrast; (b) Sample grown under identical conditions as (a) but with additional 40 minute anneal at 1125 °C.

The 2.5 ° misalignment commented on in relation to Figure 6.14 may be due in part to an effort accommodate misfit at the interface (as seen in cobalt spinels [7]), but may also be due, at least partially, to an incomplete transformation of this nature.

6.6 Concluding Remarks

The growth and structure of epitaxially ordered zinc aluminate grains and their epitaxial relation to the substrate was studied using FESEM, TEM in cross section and plan view, and other techniques. A zinc aluminate ($ZnAl_2O_4$) layer is formed by reaction of the source materials (Zn and O) with the substrate. While a significant part of the deposit is in the form of a polycrystalline thin film for lower temperature growths, a substantial amount grows with a well-defined epitaxial relationship on the sapphire. The epitaxially oriented deposit displays the form of large, characteristically twinned, grains with sub-micron dimensions. These grains display three variants, consistent with the *c*-sapphire substrate symmetry. The growth of these grains is strongly associated with the presence of extended defects in the sapphire substrate, and can be seeded by local mechanical damage to the substrate. We have also studied samples grown at higher temperatures (1125 °C) for longer times (60 minutes), and TEM data indicate that the twinned grains undergo a structural transformation, which changes the nature of the epitaxial relationship and the twin boundary crystallography in the grains, attributed to the effects of annealing during growth. In both cases the twin boundary is found to be "open", i.e. has a lower density than the surrounding material, of the order of 1 - 2 nm in width.

Samples grown at lower temperatures (950 °C) for shorter times (30 minutes) show an unusually sharp contrast in FESEM, compared to those grown at higher temperatures (1125 °C) for longer duration (60 minutes), which we uncertainly attribute to the effects of the different types of twin boundaries in the grain on electron backscattering. We have proposed a model to account for the data we observe.

Our data indicate that it is possible to grow epitaxially ordered zinc aluminate grains on sapphire and to control the morphology, epitaxial relationship and crystallographic nature of twin boundaries in the grains through control of the growth process parameters. This may enable the targeted use of this functional material system in e.g. catalytic and other applications. This level of control may be of use in new applications.

6.7 References

[1] (http://www.testbourne.com/)

[2] J. Grabowska, A. Meaney, K. K. Nanda, J.-P. Mosnier, M. O. Henry, J.-R. Duclère, E. McGlynn, *Physical Review B* **71** (2005) 115439

[3] S. B. Newcomb, in: S. McVitie, D. McComb (Eds.), Inst. Phys. Conf. Ser., No. 179, Inst. Phys., Bristol, UK, 2003, p.357.

[4] S. K. Sampath, D. G. Kanhere, R. Pandey, *Jurnal of Physics: Condensed Matter,* **11** (1999) 3635

[5] a) C. B. Carter, Y. K. Rasmussen, *Acta Metallurgica et Materialia* **42** (1994) 2729
b) C. B. Carter, Y. K. Rasmussen, *Acta Metallurgica et Materialia* **42** (1994) 2741

[6] T. M. Shaw, C. B. Carter, *Scripta Metallurgica* **16** (1982) 1431

[7] C. B. Carter, H. Schmalzried, *Philosophical Magazine A*, **52** (1985) 207

[8] D. X. Li, P. Pirouz, A. H. Heuer, S. Yadavalli, C. P. Flynn, *Philosophical Magazine A* **65** (1992) 403

[9] K. Kanaya, S. Okayama, *Journal of Physics D: Applied Physics* **5** (1972) 43

[10] G. Davies, *Physics Reports* ***176*** (1989) 83

[11] S. B. Newcomb, F. M. Ross, D. Ozkaya, W. M. Stobbs, in: M. J. Bennett, G. W. Lorimer (Eds.), The Uses of the Fresnel Method in the Study of Oxidation, Proceedings of Microscopy of Oxidation, London (UK), Institute of Metals, 1991, p.395

[12] CASINO: monte Carlo Simulation of electroN trajectory in sOlids, R. Gauvin, P. Hovongton, D. Drouin, P. Horny, H. Demers, A. R. Couture (http://www.gel.usherbrooke.ca/casino/What.html)

[13] Z. Bi, R. Zang, X. Wang, S. Gu, B. Shen, Y. Shi, Z. Liu, Y. Zheng, *Journal of the American Ceramic Society* **86** (2003) 2059

[14] L. Navias, *Journal of the American Ceramic Society* **44** (1961) 434

[15] P. G. Kotula, C. B. Carter, *Journal of the American Ceramic Society* **78** (1995) 248

[16] J. Narayan, B. C. Larsen, *Journal of Applied Physics* **93** (2003) 278

[17] C. R. Gorla, W. E. Mayo, S. Liang, Y. Lu, *Journal of Applied Physics* **87** (2000) 3736

[18] Y. Wang, K. Wu, *Journal of American Society* **127** (2005) 9686

[19] Y. Wang, Q. Liao, H. Lei, X. Zhang, X. Ai, J. Zhang, K. Wu, *Advanced Materials* **18** (2006) 943

[20] S. B. Newcomb, F. M. Ross, D. Ozkaya, W. M. Stobbs, in: M. J. Bennett, G. W. Lorimer (Eds.), The Uses of the Fresnel Method in the Study of Oxidation, Proceedings of Microscopy of Oxidation, London (UK), Institute of Metals, 1991, p.395

7 Conclusions and Future Work

In this thesis, I have given an overview of my work which is based on the growth of the zinc oxide and zinc aluminate materials via the VPT technique and the characterisation of the subsequent materials and nanostructures. My work began with the setting up of the VPT growth system and this took up approximately the first year of my Ph.D. work period. Using this apparatus in conjunction with the VLS method on Au coated sapphire substrates, single crystalline ZnO nanostructures have been prepared in a variety of morphologies and their morphology, structural and optical properties have been studied. Using the VPT growth system with uncatalysed sapphire substrates zinc aluminate domains with various epitaxial relationships to the substrate have been grown and their properties have been studied, including a proposed explanation of the unusual appearance of these structures in SEM.

7.1 Conclusions & Further Work

7.1.1 ZnO Growth on Sapphire

In relation to the growth of ZnO nanorods and related nanostructure morphologies on sapphire substrates, my work has shown the effects of changing various growth parameters, including the Au thin film thickness, growth temperature and duration.

The mechanisms by which a deposited Au thin film forms nanoclusters and the size and density of the nanoclusters was shown to be dependent on the initial Au thin film thickness, and I have proposed that at the annealing temperature used (900 °C), for Au thin film less than 50 Å the nanoclusters form by melting while cluster formation and coarsening appears to proceed by surface diffusion for thicker Au thin film. This in turn appears to affect the VLS growth mechanism, and VLS growth is not seen for Au thin film thickness > 50 Å, which suggests that the Au-Zn alloy may not form with solid Au nanoclusters.

For growth temperatures of 900 °C growth appears to be just starting, consistent with the low Zn vapour pressure expected in the chamber on the basis of the Ellingham diagram for the reaction, and optimum growth of aligned nanorods on *a*-plane sapphire appears to occur at a growth temperature of ~ 950 °C. Increasing growth durations lead to longer nanorods, as would be expected, bearing in mind the timescales over which residual oxygen is flushed from the chamber by the Ar flow.

From our study it seems that the temperature is a major key in controlling ZnO nanostructure morphology. We are able to conclude from our experimental work that at 950 °C and short duration (30 minutes) we can grow well aligned ZnO nanorods, where at lower temperature (900 °C) and longer duration (60 minutes) we can grow nanorods/nanowalls ZnO nanostructures. All the ZnO nanostructure samples were grown in a single zone furnace which is not the best equipment for the accurate study of ZnO nanostructure growth because the temperature in the furnace can vary strongly with position. Placing the substrate in slightly different positions can make a substantial difference for ZnO nanostructure growth.

The ability to control the morphology of the nanostructures grown between well separated nanorods and the nanorod/nanowall morphology seems to be determined to a large extent by the thickness and coarsening of the Au catalyst thin film and our data favour the previously proposed explanation in the literature of nanowall nucleation at "grain boundaries" in the Au thin film, i.e. at the locations where Au nanoclusters join.

We have also commented on the applicability of the conventional thermodynamic explanation of the VLS process as applied to ZnO growth on sapphire and the inadequacies we perceive therein. Specifically we have suggested that the effects of the oxygen in the chamber on the thermodynamic behaviour must play a role, and that this is consistent with previous data for VLS growth of III-V nanorod structures.

The optical properties of the ZnO nanorods grown by the VLS method on sapphire have been studied using PL. In the case of both well separated nanorods and nanorod/nanowall

morphologies the low temperature PL shows very good quality. In the case of the nanorod/nanowall morphology the quality is almost equal to that of bulk material, whereas a slightly larger bound exciton line broadening is seen for well separated nanorods, which may imply that the interconnecting nanowall structures enable strain relaxation in nanorod/nanowall samples. The ZnO nanostructures show a PL line at ~ 3.3665 eV which is not seen in any bulk crystal material studied. Based on these data and previous proposals in the literature we assign this PL feature to an exciton bound at a surface-related defect, possibly adsorbed oxygen. The bandedge free exciton PL emission from the nanorod/nanowall samples is quenched rapidly with increasing temperature compared to both bulk crystals and well separated ZnO nanorods which we interpret as evidence that the nanowall structures are of inferior crystal quality, possibly with a large dislocation content due to their large "footprint" compared to isolated nanorods, leading to strain relaxation and dislocation formation. This proposal is consistent with the narrow PL linewidths measured at low temperature for this sample and the increased quenching of free exciton emission at higher temperatures.

Based on the data presented in this thesis we feel that a reasonable degree of control has been achieved for growth of ZnO nanostructures on *a*-sapphire, whereby the morphology can be controlled and predicted by varying growth parameters. However the process remains fundamentally hard to control. Great care is needed in order to reproduce identical results in different growth runs. This has led to very many experiments and measurements in order to ensure reproducible results. The origins of these difficulties are not entirely clear, but it appears that VLS growth on Au coated substrates in the temperature region 900 – 950 °C using carbothermal reduction of ZnO powder involves rather low Zn vapour pressures, and that the melting behaviour of the Au particles also changes in this temperature interval. Both these facts very likely make the process very sensitive to small changes in process parameters. This in turn indicates that scaling the growth to substrate sizes of the order of inches will be difficult. Our experience is that homogeneous growth is generally only possible over smaller samples (of the order of 5 x 5 mm^2). Very tight control of furnace temperature profiles and Zn vapour pressure and supersaturation will be required to scale VPT growth to commercial levels.

Nevertheless, the current capability in terms of growth control represents a significant step toward realising the application of ZnO nanostructures as buildings blocks in nanoscale electronics and photonics, both in terms of identifying key growth parameters for morphology control and in terms of identifying challenges in terms of reproducibility and scaleability.

Further investigation of these ZnO nanostructures will be both exciting and highly worthwhile. The work presented above has raised as many new questions as it has answered. During the course of this thesis I have identified a number of scientific topics and potential application areas which would form suitable areas for fruitful further research as follows:

Scientific topics:

1 – Passivation of ZnO nanostructure surfaces: The work in chapter 5 of this thesis indicated that the large surface to volume ratio of ZnO nanostructures has an important effect on optical properties. A more detailed study of the nature of the surface processes which influence the optical emission and how these can be controlled, e.g. by passivation, would be a useful topic of research, particularly as the effects of the nanostructure surface will be key if ZnO nanostructures are to be used in sensors applications. This work is continuing in our group, with a Ph.D. student, Ms. Mahua Biswas, building on the work presented here.

Application areas:

1 – Chemical modification of ZnO nanowires: Zinc oxide and other metal oxides such as TiO_2 have been modified with e.g. ruthenium bipyridine complexes, for photochemical charge transfer applications such as Graetzel solar cells [1] and these structures have been reported in the literature. However there are few reports of zinc oxide nanorods chemically modified in this way. The ability to control the nanorod morphology and surface to volume ratio of ZnO nanostructures is an obvious advantage for such Graetzel cells. I have worked with a Ph.D. student in the School of Chemical Sciences at DCU, Mr. Robert Groarke, on preliminary investigations of the feasibility of modifying our ZnO nanostructures using

ruthenium complexes and the outcome of the these initial investigations was positive (see Figure 7.1) [2].

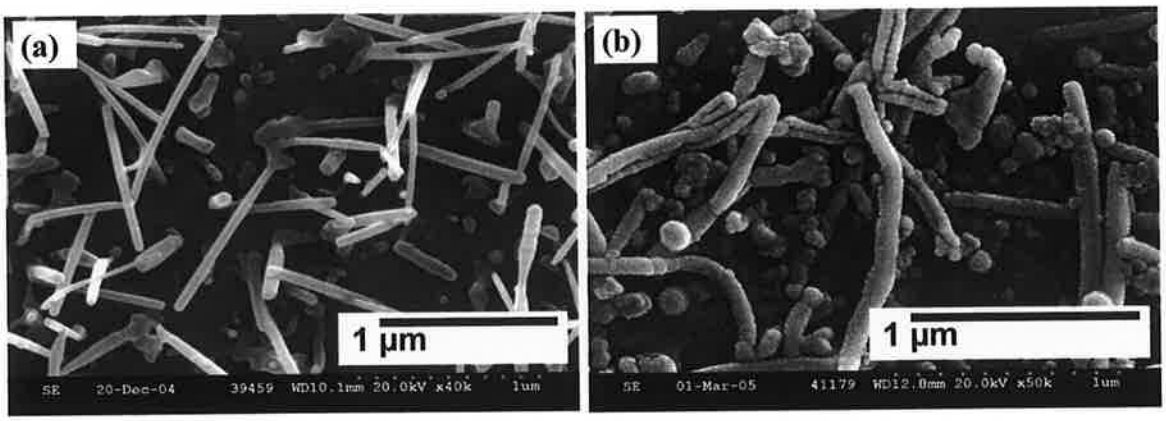

Figure 7.1 FESEM images of unmodified nanorods (a) and modified nanorods with ruthenium complex (b).

Looking at the images (Figure 7.1) of ZnO nanorods unmodified and modified with ruthenium complex we can see that the morphology of the modified rods is completely changed after modification and that the ruthenium complex appears to attach to the nanostructures.

2 – Superhydrophobicity of ZnO nanostructures / hydrophobic coatings: We have undertaken preliminary investigations with Dr. Alan Lyons of Lucent Technology in Ireland 'nanograss' structures. Nanograss surfaces (discovered by Bell Labs [3]) typically contain billions of tiny silicon rods, formed by top-down lithography. These are then coated with hydrophobic material. These surfaces are designed to reduce the contact area with liquids and thus to increase the contact angle and reduce wetting behaviour for applications in heat transfer involving liquid coolants. The results from these experiments could lead to important breakthroughs in cost effective communications devices and networks. Higher processing speeds from liquid cooled devices will support more compactly packed circuits in communications devices, which could allow communication service providers to operate lower broadband services.

The general idea of our investigations was to use our well aligned ZnO nanorods as an alternative 'nanograss'. ZnO is a naturally hydrophobic material so doesn't need extra coating and our growth is a self-organised bottom-up process. We have provided various substrates for Lucent to test, including nanorods and bulk ZnO crystals. The contact angle measurements have been done for our ZnO nanorods by Grace Jordan from Lucent Technology in Ireland (table 7.1). They show a number of interesting features:

1. The contact angle on the flat, bare ZnO bulk crystal surfaces (both Zn-terminated and O-terminated) are similar and much lower than would be necessary to achieve superhydrophobicity. Actually the value for these surfaces are just higher then the literature value for flat gold surfaces, 75.9 degrees [4].
2. The contact angles on the ZnO nanorod surfaces (both bare and Au coated) are significantly higher than for flat ZnO surfaces and gold films. The contact angles are as high or higher than for teflon surfaces in the case of the Au coated ZnO nanorod sample.

Sample	Mean (degrees)	No of measurements
Silicon nanograss	154.8	6
O-term ZnO	84.7	3
Zn-term ZnO	79.3	3
Gold sputtered ZnO nanorods	119.5	2
ZnO nanorods	106.0	1
Gold	75.9	Ref. [4]

Table 7.1 Contact angle measurements for various materials.

These data show an interesting effect. The nanorod morphology of the ZnO samples seems to increase the contact angle, in a manner similar to that seen for the Si nanograss. Other reports in the literature support our data and indicate that ZnO nanorod surfaces show much higher contact angles compared to flat ZnO surfaces [5 - 7].

However, these initial investigations have not continued any further as the angles are still much lower then for a Si nanograss surface. This largely to do with the lack of a uniform nanorod height and spacing compared to lithographically defined Si nanograss, and also due to the relatively small area of our ZnO nanorod samples.

3 – Living cell immobilization on ZnO nanostructures: The ZnO nanorod morphology may provide an interesting scaffold on which to try to grow and culture biological cells. The "bed of nails" approach for living cell immobilisation may offer advantages compared to conventional tissue culture plastic. Initial experiments are ongoing with Dr. Finbarr O'Sullivan and Prof. Martin Clynes of the National Institute for Cellular Biotechnology (NICB) at DCU who are using samples grown during this thesis work and studying various aspects of cell adherence and viability thereon. Initial outcomes from this study are positive and further assays are being undertaken. A couple of aspects have produced initial data:

- *Cell Adherence to Surface*

The lung cell line DLKP was selected as a test cell line. It is an adherent cell with growth and attachment qualities. Cells were suspended in culture media at high density and seeded on 2 ZnO nanorod samples and cultured for 24 hrs at 37 °C in 5 % CO_2. After 24 Hrs the media was replaced with fresh media and the cells cultured for a further 24 Hrs. For control purposes DLKP was cultured on standard tissue culture plastic under the same conditions.

DLKP adhered to both surfaces of ZnO nanorods samples, selectively and did not adhere at all to the plastic support material. The DLKP cells on 1 surface of the ZnO nanorods sample exhibited a round morphology and cells existed as single cells or as clumps of 2 or 3 cells, Figure 7.2. A similar morphology was observed for cells on the other surface of the ZnO nanorod sample, Figure 7.3. In contrast the DLKP cells on the control tissue plastic grew as colonies with a flattened cobble stone morphology, Figure 7.4.

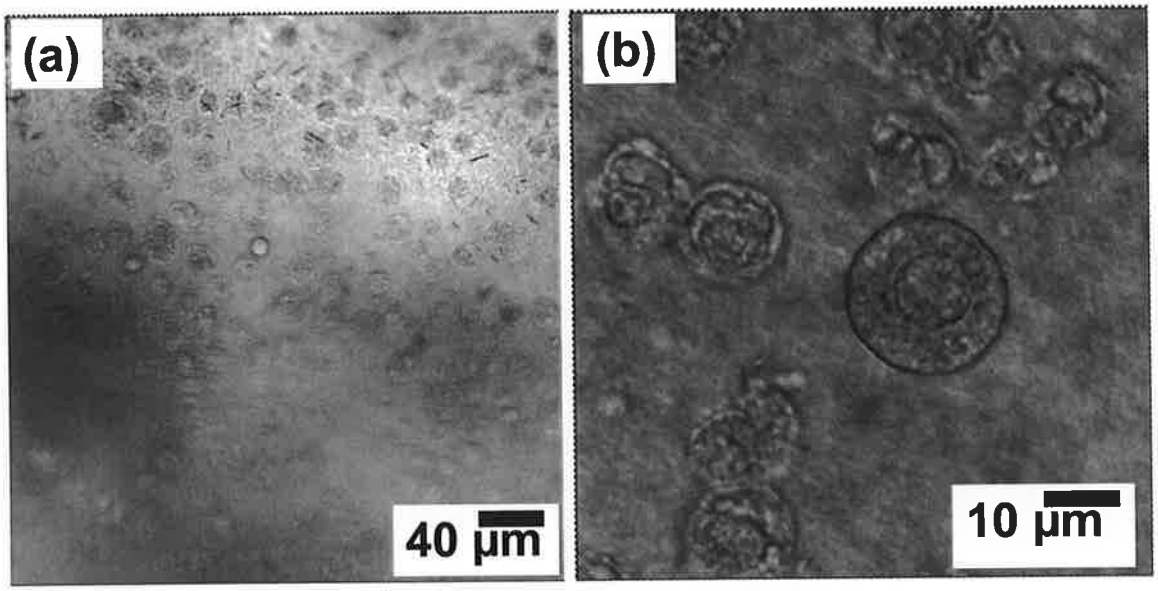

Figure 7.2 *Morphology of DLKP of the first ZnO nanorods sample. (a) view of cell field, (b) increased magnification of cells.*

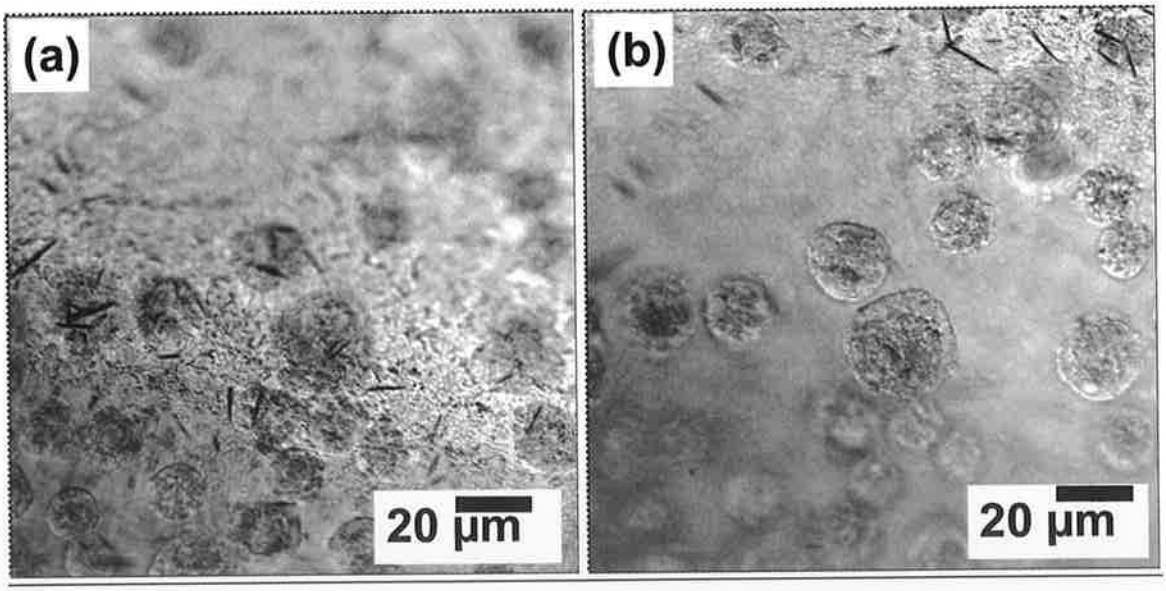

Figure 7.3 *Morphology of DLKP of the second ZnO nanorods sample, (a) and (b) are the same cell field at different focal depths.*

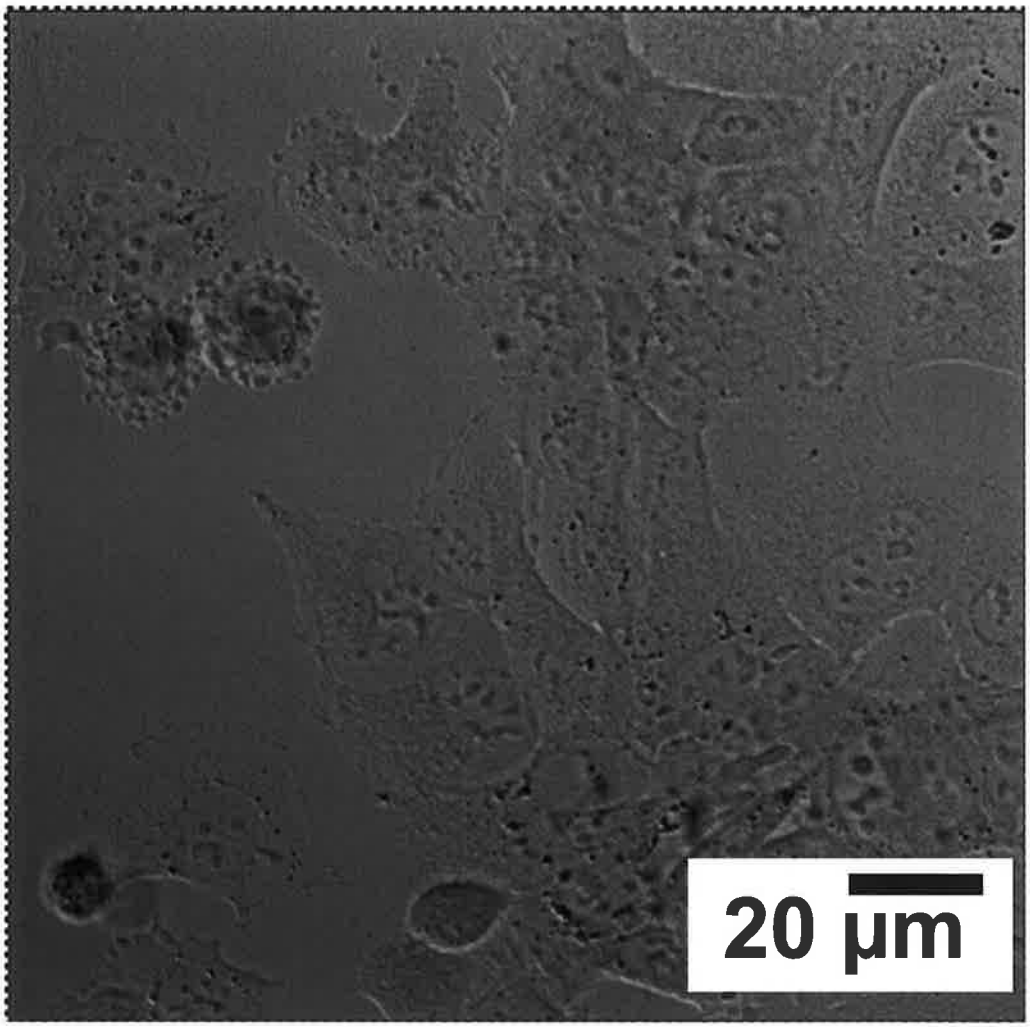

Figure 7.4 DLKP on standard tissue culture treated plastic.

-Investigation of Actin Cytoskeleton

An actin cytoskeleton was investigated to see if a change was induced by growth on the two ZnO nanorod test surfaces. The DLKP cells on the various surfaces were fixed and permabilised with ice-cold methanol. Filamentous actin was probed for with phallodin conjugated with Alexa 488, the nuclei were counterstained with DAPI. Unfortunately the actin staining was inconclusive and no sample existed to repeat, Figure 7.5, 7.6, and 7.7. In the case of the second surface ZnO nanorods sample, some DNA was observed to have leaked from the cells, indicating cell death, Figure 7.6. This maybe due to sample drying that occurred during earlier imaging earlier to fascination, rather then cell toxicity due to the surface.

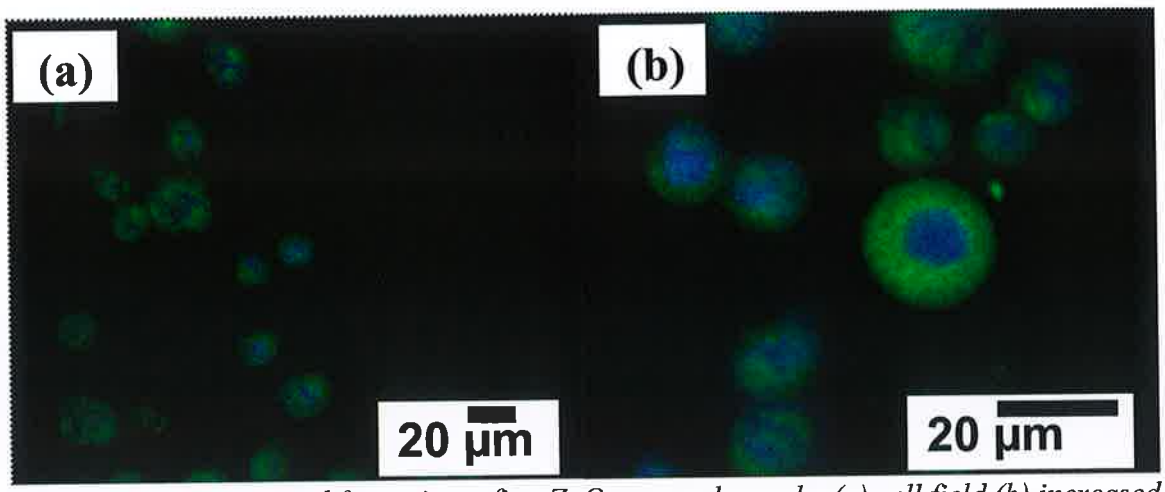

Figure 7.5 DLKP stained for actin on first ZnO nanorod sample. (a) cell field (b) increased magnification of cells. Actin green, Nuclei blue.

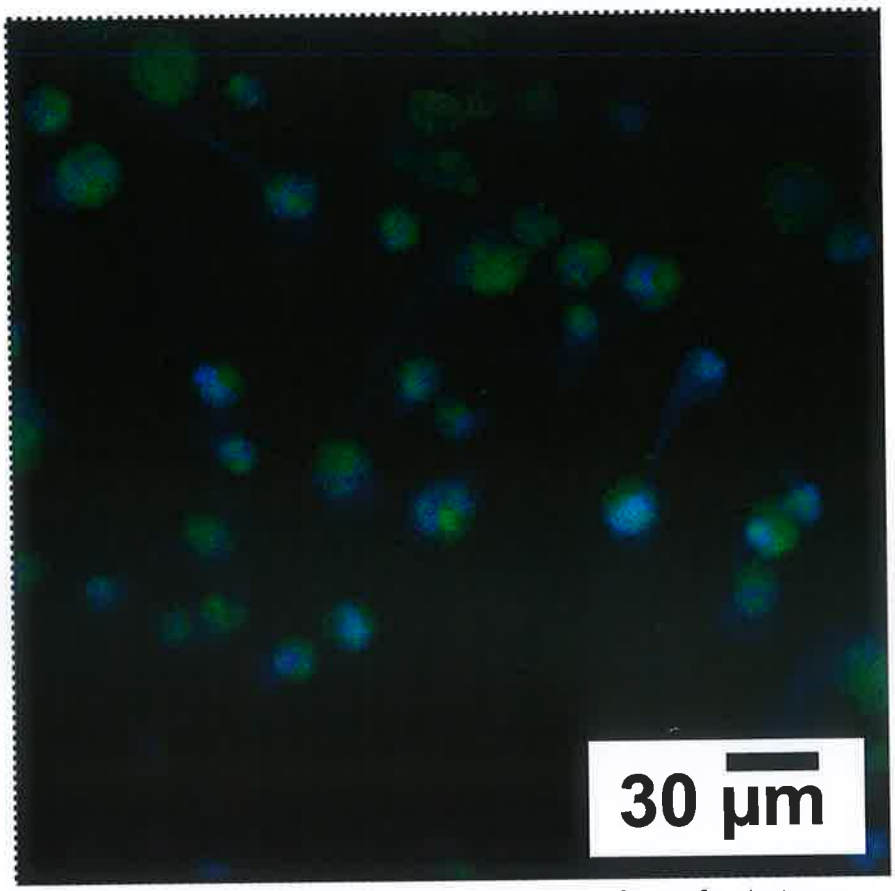

Figure 7.6 DLKP stained for actin on second ZnO nanorod sample. Actin green, Nuclei blue.

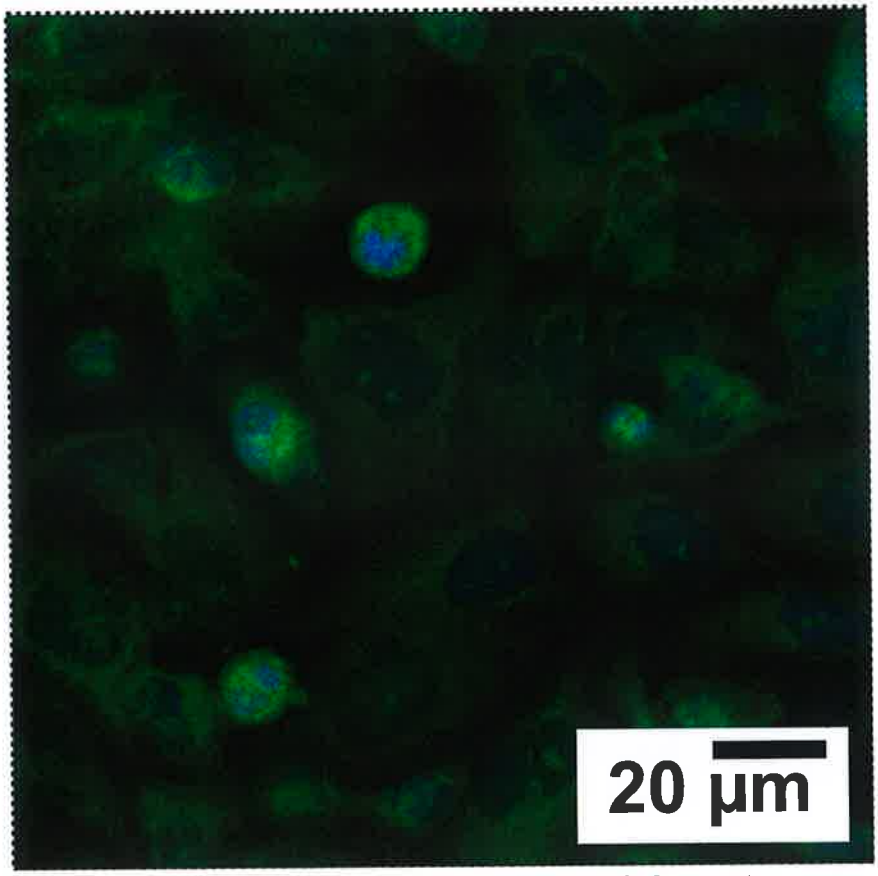

Figures 7.7 DLKP stained for actin on tissue culture treated plastic. Actin green, Nuclei blue

A number of further questions concerning long term cell viability and ability to reproduce are currently being studied with a new set of 5 ZnO nanorod samples.

4 – Free-Standing GaN Substrates: The general idea of this topic is that well aligned ZnO nanostructures could be used as an epilayer/buffer layer for growth of thick, good quality, GaN layers. This is based on two physical facts, firstly that ZnO and GaN have very similar lattice constants (ZnO, a = 3.249 Å, c = 5.207 Å; GaN, a = 3.189 Å, c = 5.185 Å) in the basal plane [8] and secondly that ZnO nanorods have such a small footprint that they are generally single crystalline with no dislocations. The combination of these facts means that a continuous GaN layer might be able to grow on the ZnO nanorod array with low dislocation density, with the GaN layer growing across the "gaps" in a manner similar to that seen in pendeo-epitaxy [9]. Following GaN film growth the ZnO could be removed by laser ablation or chemical etching to leave a strain free, thick, freestanding, GaN film. We

have supplied ZnO nanorod samples to the HVPE growth laboratory in Faculty of Microsystem Electronics and Photonics in Wroclaw University of Technology in Poland for initial investigations of GaN growth. No results are available as yet.

7.1.2 $ZnAl_2O_4$ Growth on Sapphire

In relation to zinc aluminate growth on uncatalysed *c*-sapphire substrates my work has characterised the characteristic epitaxially grown domains which are seen on substrates with poor crystal quality. This topic arose from attempts to grow ZnO on uncatalysed sapphire substrate. These aluminate domains show an unusual appearance in SEM, with a distinctive bright central line feature. These bright central lines are oriented at 120 degrees to each other, and the appearance prompted us to study the composition and origin of the structures. TEM studies in collaboration with Dr. Simon Newcomb of Glebe Laboratories established that the bright central line features are associated with twin boundaries in the aluminate domains. These bright line features come in three variants, consistent with the three fold symmetry of the *c*-sapphire substrate. Fresnel contrast experiments have established that the twin boundary regions are "open", i.e. of lower density that the surrounding aluminate material.

We have characterised the epitaxial relationship of the aluminate domains to the substrate at various growth temperatures and growth times and established that the relationship changes with annealing at higher temperatures for longer times. The change in epitaxial relationship alters the visibility of the twin boundaries in SEM images.

We have established that the appearance of these micron-sized grains is associated with poor quality substrates and possibly dislocations at the substrate surface interfere with the initial growth of the aluminate grains, generating the twin boundary structures.

Enhanced material transport through these open twin boundaries means that the aluminate growth at these locations is substantially thicker than at other locations on the substrate,

which is consistent with previous observations of thicker aluminate layer growth at grain boundaries [10].

Our data indicate that the bright contrast seen in SEM is due to backscattering/waveguiding effects along the open twin boundaries and the data are unusual as they imply that we are seeing direct images of twin boundaries in the SEM. Normally twin boundaries are seen in SEM only by virtue of channelling effects (i.e. diffraction-based effects) due to their different crystalline orientation which alter the Bragg conditions.

Further investigation of these aluminate domains could proceed along a couple of useful directions as follows:

Scientific topics:

1 – Mechanism of bright line SEM contrast: Our initial experiments on backscattering and secondary electron imaging of the aluminate grains strongly indicate that enhanced backscattering/waveguiding along the open twin boundaries is responsible for the SEM contrast. Further detailed investigation of this phenomenon is needed to firmly establish the mechanism, and computational modelling using Monte-Carlo techniques could provide quantitative confirmation of this effect.

2 – Mechanism by which the twinned aluminate grains nucleate and grow: Our data establish a connection between the presence of extended defects in the sapphire and the nucleation of twinned aluminate grains quite convincingly. However only very preliminary attempts to process the sapphire surface in a more localised and controlled way to generate equivalent surface disruption or "damage" by means of nano-indentation, plasma/chemical etching and laser ablation have been undertaken. It appears that the twinned aluminate grains can nucleate and grow on etched samples. However much further work needs to be undertaken to establish the nature of the surface disruption which is required to nucleate the grains, the nature of the grain growth, and the details of the temperature window in which the twinned grains form.

Application areas:

1 – Zinc aluminate can act as a catalyst for a variety of reactions, and the catalytic activity may be affected by the faceting of the aluminate grains. Further investigation of the catalytic activity of the different epitaxially oriented micron-sized twinned zinc aluminate grains presented in this thesis will be an interesting direction to study whether catalytic activity can be controlled by the growth parameters.

7.2 References

[1] M. Law, L. E. Greene, J. C. Johnson, R. Saykally, P. Yang, *Nature Materials* **4** (2005) 455

[2] R. Groarke, J. Grabowska, E. McGlynn, J. G. Vos, Spie 2004 in print

[3] http://www.reed-electronics.com/semiconductor/article/CA420726

[4] B. S. Sumerlin, A. B. Lowe, P. A. Stroud, P. Zhang, M. W. Urban, Ch. L. McCormick, *Langmuir* **19** (2003) 5559

[5] Y. H. Yang, Z. Y. Li, C. X. Wang, D. H. Chen, G. W. Yang, *Journal of Physics: Condensed Matter* **17** (2005) 5441

[6] S. Yin, T. Sato, *Journal of Materials Chemistry* **15** (2005) 4584

[7] H. Liu, L. Feng, J Zhai, L. Jiang, D. Zhu, *Langmuir* **20** (2004) 5659

[8] S. J. An, W.I. Park, G.-Ch. Yi, *Applied Physics Letters* **84** (2004) 3612

[9] K. Linthicum, T. Gehrke, D. Thomson, E. Carlson, P. Rajagopal, T. Smith, D. Batchelor, R. Davis, *Applied Physics Letters* **75** (1999) 196

[10] C. R. Gorla, W. E. Mayo, S. Liang, Y. Lu, *Journal of Applied Physics* **87** (2000) 3736